Analyses of Electron–Proton and Hadron–Hadron Collisions Using the Linked Dipole Chain Model

Gabriela Miu

Department of Theoretical Physics
Lund University, Sweden

Thesis for the degree of Doctor of Philosophy

Thesis Advisor: Gösta Gustafson

Faculty Opponent: Gavin Salam

To be presented, with the permission of the Faculty of Mathematics and Natural Sciences of Lund University, for public criticism in Lecture Hall F of the Department of Theoretical Physics on Friday, October 25th, 2002, at 10.30 a.m.

To the interested reader

This thesis is based on the following publications:

- I G. Gustafson and G. Miu,
  Minijets and Transverse Energy Flow in High Energy Collisions
  Physical Review **D63**, 034004 (2001).

- II G. Gustafson and G. Miu,
  A Simple Model for the BFKL–DGLAP Transition in DIS
  European Physical Journal **C23**, 267–274 (2002).

- III G. Gustafson, L. Lönnblad and G. Miu,
  Gluon Distribution Functions in the $k_\perp$–factorization Approach
  Journal of High Energy Physics **09**, 005 (2002).

- IV G. Gustafson, L. Lönnblad and G. Miu,
  Hadronic Collisions in the Linked Dipole Chain Model
  hep-ph/0209186.

In addition, during my years as a Ph.D. student I have contributed to the following publications:

1. G. Miu and T. Sjöstrand,
   W **Production in an Improved Parton Shower Approach**
   Phys. Lett. **B449**, 313–320 (1999).

2. T. Sjöstrand, P. Edén, C. Friberg, L. Lönnblad,
   G. Miu, S. Mrenna and E. Norrbin,
   High–Energy Physics Event generation with PYTHIA 6.1
   Computer Phys. Commun. **135**, 238–259 (2001).

3. Small x Collaboration (B.Andersson *et al.*),
   Small x Phenomenology: Summary and Status
   hep-ph/0204115.

Contents

Introduction

The pure and simple truth is
rarely pure and never simple.
Oscar Wilde

In this thesis we perform phenomenological studies of Quantum Chromodynamics in the context of deeply inelastic electron–proton and high–energy hadron–hadron collisions.

The thesis consists of this introduction and four articles.

The first two sections of the introduction are aimed at a general audience of physics students. We start with an historical overview of the field of particle physics up to the point where the composite nature of the proton was experimentally established. In the second section, the theory that constitutes the foundation of modern particle physics, namely the Standard Model, is briefly presented.

The subsequent two sections are of a more technical character and are intended for students with some knowledge of particle physics. Here we describe different techniques that particle physicists have at their disposal. Thus, in section three we focus on the theoretical tools, including both analytical and numerical ones. In the fourth section, the experimental techniques are presented, with emphasis on the description of two classes of experiments involving protons: electron–proton and proton–proton collisions.

The initiated researcher can go directly to the remaining two sections, or to the papers themselves. The fifth section contains a brief description of the Linked Dipole Chain model which is the phenomenological model used to produce the results of the thesis. The sixth and final section gives a short summary of the papers; these appear in their entirety in the subsequent chapters.

The Complex Nature of the Proton

The goal of elementary particle physics is to describe matter at its most fundamental level. Assuming that all matter is made of some tiny fundamental particles, the aim is to describe their properties and the ways in which they interact among each other. The term *fundamental* is used here to designate a point-like particle, i.e. one that lacks an internal structure.

The idea that all matter that we see around us consists of some smallest, indivisible units, called "atoms" (from the Greek "átomos", which means "not cuttable") was proposed already about 2500 years ago, by Leucippus, and was perpetuated by his pupil, Democritus. By that time, no confrontation with reality was possible – Leucippus himself postulated these atoms as being too small to be observed – leaving the questions on the nature of matter open to speculation and debate: they were philosophical, rather than scientific questions. Leucippus's atomic theory was just one of several different philosophical points of view regarding the structure of matter, alongside with, for instance, Empedocles's theory about matter being comprised of the four elements earth, air, fire and water.

Empedocles's theory, later adopted and extended by Plato and Aristotle, came to be generally accepted throughout the Middle Ages, but was proved inaccurate and abandoned during the Renaissance.

Around the year 1800, J. Dalton – an English professor of physical sciences – proposed a theory, derived from two centuries of chemical experiments, in which he asserted that the chemical elements are made of tiny indivisible particles. He called these particles atoms, as an homage to Leucippus.

The experiments that followed seemed to suggest that the atom might be composed of smaller objects. As we will see, our picture of the structure of matter is an ever-changing one, and it has often happened during the course of history that objects originally thought to be fundamental turn out to be composite.

Like any other branch of physics, particle physics relies greatly on experiments. The opportunity to perform experiments in this field did not arise until about a hundred years ago, and since then many ground-breaking discoveries have been made, leading to much progress in our understanding of nature at the microscopic level.

So why, then, was it so difficult to perform experiments aimed to study the structure of matter? The answer is of course that elementary particles are so small that they cannot be studied with the bare eye, and new experimental methods needed to be invented.

In everyday life we observe things by making use of visible light, i.e. electromagnetic waves of wavelength within the range: $10^{-7} - 10^{-6}$ m. The process of observing physically means that light is allowed to shine on the object of interest and this light, after being reflected by the object, is detected by our eyes directly, or through different optical microscopes. Since for an object to be resolved, its size must be at least that of the wavelength of light, this sets a natural limit to how small objects may be observed with light.

In order to study even smaller objects, radiation of smaller wavelengths is necessary and detectors of different kinds are needed to "observe" it. To this end, so-called scattering experiments are employed, in which a probe is sent towards the object (target) of interest, and studies of the outcome of such processes are used to obtain information about the structure of the target. Because of the quantum mechanical nature of the tiny particles involved, these can be thought of as waves, whose wavelengths λ are related to their momenta p according to $\lambda = h/p$ (h is known as Planck's constant[1]). Thus, the faster the particles are, the smaller the sizes that can be resolved.

Scattering experiments have proven very fruitful in exploring the structure of matter.

As a first example, we may take the experiment performed by Rutherford in 1911, that consisted of bombarding a thin gold foil with α-particles (helium nuclei). In those days, the atom was thought of as a sphere with its charges (both positive and negative) evenly distributed throughout, so as to give an electrically neutral atom. According to such a model, the majority of the α-particles would have just passed through the atoms of the golden foil. Instead Rutherford observed that an unexpectedly large number of α-particles actually rebounded after slamming into the foil. He concluded that this can only be the case if most of the atom is concentrated within a tiny electrically charged core at its center (the nucleus), with a uniform spherical distribution of opposite electric charge surrounding it (the electrons).

Later scattering experiments made use of electrons as probes in order to study the structure of the atoms. At first electrons of moderate energies were used (<100 eV) and the experiments proved fruitful in mapping the electron shells of the atoms. The development of particle accelerators made it possible to achieve much higher energies, thus accelerating electrons up to some hundreds of MeV (1 MeV = 10^6 eV); these corresponded to a resolution that was high enough to permit studies of the nuclear structure. In this way the existence of the constituents of the nucleus – the protons and the neutrons – could be established.

For a long time it was believed that electrons, protons and neutrons were elementary, i.e. they were thought to lack an internal structure, and the term *elementary particles* was coined, as a common name for these particle. However, it turned out that the protons and neutrons are not fundamental.

As a consequence of the many particle collisions that were studied during the 1940's and 1950's, a large number of particles were detected, all of which

[1] In particle physics, natural units are employed, meaning that the constants $h/2\pi$ and c are set $h/2\pi = c = 1$. In these units, Einstein's famous relation between the rest mass of a particle and its energy becomes $E = m$, i.e. the concepts of mass and energy can be used interchangeably.

were similar to the protons and the neutrons. These discoveries cried out for a systematization of all particles, the multitude and regularities of which seemed to suggest that they could not be the ultimate building blocks of matter. In 1961, by making use of the mathematical concept of group theory, the theoretical physicists M. Gell-Mann and Y. Nèeman proposed a scheme in which all the discovered particles fitted very well. In the version of the theory presented by M. Gell-Mann and G. Zweig a few years later, all the discovered particles were assumed to be composed of three building blocks; these were collectively called "quarks", and they were named u (up), d (down) and s (strange). Furthermore, the theory predicted the electrical charge of u, d and s to be $(2/3)e$, $-(1/3)e$ and $-(1/3)e$, respectively, i.e. fractions of the electron's charge.

In spite of the intense search for quarks that took place in the years that followed, no direct experimental evidence for their existence was found. This led people to believe that perhaps the quarks were just mathematical objects, without any correspondence in reality.

The proof of the existence of quarks came with yet another scattering experiment, known as the SLAC-MIT [1] experiment, that was performed during the second half of the 1960's. As we shall see, at the time the results were presented, the appropriate interpretation was not at all obvious; the theoretical physicists J.D. Bjorken and R.P. Feynman were the key persons contributing to a correct interpretation.

In the SLAC-MIT experiment energetic electrons were allowed to strike the protons and neutrons of a target consisting of liquid hydrogen. The experiment was run on two different occasions, with the energy much increased the second time.

When an electron of energy E is allowed to hit a proton (or neutron) which is at rest, there can be different outcomes.

If the scattering leaves the proton unexcited, then it is called *elastic*. There is only one free variable and the collision can be fully described in terms of e.g. the electron's scattering angle θ. Alternatively, the free variable can be chosen to be Q^2, which is a measure of the momentum transfered from the electron to the proton in the collision. This process is illustrated in Fig. 1a.

If instead the scattering is such that it results in the excitation of the proton, the collision is called *inelastic*. Such collisions typically have large Q^2 values. As opposed to elastic collisions, there are now two independent variables. Besides Q^2, also the invariant mass of the excited proton, W^2, represents a degree of freedom. (In the case of elastic collisions, W is simply the proton's mass m_p, which is of course constant.)

In a scattering experiment, such as the SLAC-MIT, in which electrons of energy E are allowed to collide with protons, the measured quantities are the scattering angle θ and the energy of the deflected electrons, E'. In this way the reaction *cross section* σ, giving the probability for scattering to take place between the particles involved in the collision, can be obtained.

One possible way to analyze the structure of the proton is to compare the observed scattering probability with the one expected if the proton were point-like. We can then write (schematically) the reaction cross section as:

$$\sigma = \sigma_{point} \cdot F^2,$$

where σ_{point} represents the (known) relativistically correct expression for the probability of an electron scattering against a point-like proton. The quantity F parameterizes the detailed structure of the proton. In the case of elastic electron-proton collisions, F is expressed in terms of "form factors" that depend on Q^2 only; the relevant scale for this Q^2-dependence is given by the proton's mass m_p. These form factors account for the distribution of electric charge and magnetic moment inside the proton. When inelastic electron-proton scattering takes place, the corresponding F is written in terms of "structure functions" that now depend on the two variables Q^2 and W^2.

When the SLAC-MIT experiment was run the second time, at higher energies (and higher Q^2) as compared to the first run, an increased number of inelastic scatterings could be studied. An unexpectedly large number of so-called *deeply inelastic scattering*, i.e. scattering characterized by very large values of Q^2 and W^2, was noted. The surprising result was that the measured inelastic structure functions for these collisions were no longer functions of Q^2 *and* W^2 independently, but rather seemed to depend only on the *ratio* between

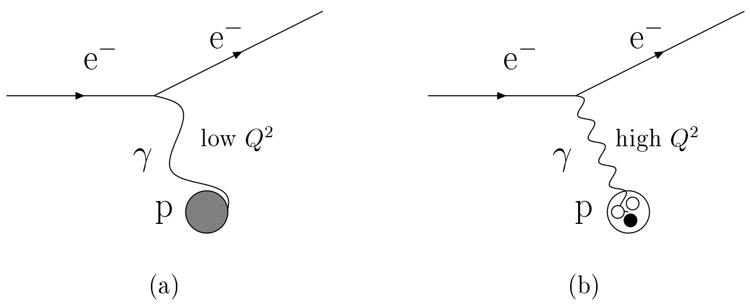

Figure 1: (a) Elastic electron–proton scattering, characterized by moderate values of Q^2. The corresponding resolving power, $\lambda = 1/\sqrt{Q^2}$, is comparable to the size of the proton. (b) Deeply inelastic electron–proton scattering, usually of very large values of Q^2, which are able to probe the quark content of the proton.

them. Actually Bjorken had predicted that this phenomenon, known as scale invariance, would set in at very large values of Q^2 and W^2 ($\gg m_p^2$). Feynman showed that these results could be interpreted in terms of *elastic* scattering of the electron against *point-like* "partons" within the proton (the name parton indicates that it refers to an object that is a part of the proton), with scaling as a natural consequence. This process is illustrated in Fig. 1b.

The task of proving that the observed point-like partons were indeed the earlier introduced (hypothetical) quarks was not a trivial one. In the quark–parton model, one starts by postulating that these two concepts (the parton and the quark) are indeed identical.

The scattering process may be analyzed in a frame given e.g. by the electron's and proton's center of mass system, with the proton having a considerable momentum. In the quark–parton model, the quantity F depends on two structure functions F_1 and F_2, that are both scaling. Actually, these are not independent, and it suffices to specify one, e.g. F_2. This receives contributions from the different quarks within the proton and can be written as a sum:

$$F_2(x) = \sum_i e_i^2 x f_i(x),$$

where $x = 1/(1+(W^2/Q^2))$ and e_i is the electric charge of quark i; the functions f_i, called parton distributions, represent the probability of finding a quark of flavor i inside the proton, carrying a fraction x of the proton's momentum.

Careful measurements of the proton structure function have confirmed the assumption that the observed partons really were the hypothetical quarks. In particular it has been possible to deduce that the quarks have indeed the fractional electric charges predicted theoretically; it was further inferred that the proton is made of three "valence" quarks (two u quarks, and one d quark) and additional "sea" quarks that arise as quark-antiquark pairs, as a result of quantum fluctuations.

However, an intriguing thing was found: when the momentum fractions of the quarks inside the proton were summed over, it was observed that together they only accounted for half of the proton's total momentum!

This apparent contradiction is solved by quantum chromodynamics, QCD (see next section), which is the theory that is now known to correctly describe the strong interaction between the quarks. According to this theory some additional electrically neutral partons, called "gluons", exist inside the proton. Studies of the proton's structure functions have led to a picture of the gluons that is consistent with QCD and indicate that the gluons carry the missing half of the proton's momentum.

The quark–parton model completely ignores the existence of gluons and assumes Bjorken scaling to be perfect. In QCD, at high Q^2 the elastic electron–quark scattering is altered by the possibility of the quark's first emitting a gluon, before reacting. Because of this, scaling is no longer perfect, and F_2 becomes a function of Q^2 as well as of x. Scaling violation has indeed been observed experimentally and constitutes yet another proof that QCD is self–consistent.

To summarize, we have seen how scattering experiments have played an essential role in revealing the different layers of matter. By allowing electrons of increasingly high energies to scatter against matter, the excited states of the atoms, the nuclei and the protons and neutrons were observed. In particular, deeply inelastic electron-proton scattering experiments have led to a picture of the proton as being composed of quarks, antiquarks and gluons (see next section), whose properties inside the proton are described in terms of parton distributions.

In a scattering experiment of the kind we have described, one might expect the quark that was “kicked out” of the proton and the remains of the proton to come out of the collision. In fact, free quarks have never been observed, but instead what does come out are lots of particles composed of quarks and gluons, collectively referred to as hadrons (see next section). These hadrons tend to move in the same directions as the original quark or proton remnant. The more energetic e.g. the quark is, the more concentrated the hadrons are about its direction; these concentrated beams of particles are referred to as particle jets.

In this thesis we study the proton's structure and the distributions of particle jets that result from energetic electron–proton and proton–proton collisions.

Fundamentals of Particle Physics

The modern theory of the fundamental particles and their interactions is called the Standard Model. This is based on the assumption that quantum mechanics governs the behavior of the microscopic world, and it assumes the validity of Einstein's special theory of relativity.

There are four (known) fundamental forces in nature, namely the electromagnetic, the strong, the weak and the gravitational force; even though the latter is important in everyday life, it can essentially be neglected in the context of the microscopic world and shall not be treated in the rest of this section. With the exception of gravity, all of these fundamental forces have been successfully formulated in terms of quantum field theories. Here, the forces are assumed to arise through local processes (as opposed to arising by means of action at a distance), that involve the absorption and emission of particles. To each force there is an associated charge, and when particles possessing that particular charge interact, they do so by exchanging a quantum (or gauge boson) specific to the force in question. Thus, the list of the fundamental particles of the Standard Model includes not only the particles that constitute matter, but also the quanta associated with the forces.

As mentioned in the previous section, the fundamental particles are assumed to be simple objects that lack internal structure. They can be described in terms of a few characterizing properties. Besides having a mass, they may also possess several kinds of charges. Furthermore, they can possess "spin", which is a quantity related to their magnetic properties. Quantum mechanics supplies a natural unit for spin, and in terms of that unit a "boson" is defined as a particle with integer spin (0,1,2, and so on), while a "fermion" refers to a particle of half-integer spin (1/2, 3/2, 5/2, and so on). All the matter particles of the standard model are fermions of spin 1/2 and all the force quanta corresponding to the different interactions are bosons of spin 1. (The only exception is the graviton, which is the quantum of the gravitational force, that has spin 2.)

It turns out that quantum field theory implies a fundamental symmetry of the elementary particle system between particles and their "antiparticles": for every particle there is a corresponding antiparticle, of identical mass, but having all other charges reversed. Thus, the particle spectrum is augmented by these antiparticles.

Quantum electrodynamics (QED), the theory that describes interactions between electrically charged particles, represents the first successful example of a quantum field theory; at macroscopic level it reproduces the well-known classical electrodynamics. In QED, the interaction between two electrically charged particles is viewed as mediated by the exchange of photons, which are the quanta of the electromagnetic force. This is most easily understood in terms of so-called Feynman diagrams, which give a pictorial description of the interaction (see also next section).

As an example, Fig. 2 illustrates the interaction between two electrons. One of the electrons emits a photon and recoils; this photon is then absorbed by the other electron, which consequently changes its motion. We note that the described process violates the law of conservation of energy. Due to quantum mechanics, this law need not hold for finite time intervals, a consequence of Heisenberg's uncertainty principle, applied here to energy and time: for a short while the system can borrow enough energy in order for the first electron to emit a photon, and this energy is returned when the second electron absorbs the photon. Such a process is referred to as the exchange of a "virtual" photon.

The electron–proton interaction of the previous section is also of electromagnetic nature, and involves the exchange of a virtual photon (cf. Fig. 1). Q^2 is called the photon *virtuality*, and measures the amount by which its mass deviates from that of a real photon i.e. from 0 (cf. Table 2).

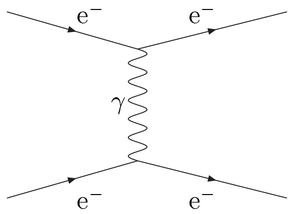

Figure 2: The electromagnetic interaction between two electrons (e^-) via the exchange of a virtual photon (γ) represented by the wavy line.

The quantum theory describing the strong (or color) interaction is called quantum chromodynamics (QCD). This interaction is responsible for keeping the quarks together inside the protons, neutrons and generally inside all hadrons, as well as for binding the protons and neutrons together inside a nucleus.

There are six (known) kinds or "flavors" of quarks, as shown in the upper part of Table 1.

Thus, besides the u, d and s quarks mentioned earlier, there exist in addition c, b and t quarks, with the latter discovered only recently, in 1995. The quarks are sensitive to the color force, and consequently possess "color" charge. The three possible color charges are labelled red, green and blue, for reasons that will become clear in a short while. Besides having color charge, the quarks are also electrically charged. In the units in which the electron has the electric

	First Family	Second Family	Third Family	Electric Charge
Quarks	$\begin{pmatrix} u \\ d \end{pmatrix}$	$\begin{pmatrix} c \\ s \end{pmatrix}$	$\begin{pmatrix} t \\ b \end{pmatrix}$	$\frac{2}{3}e$ $-\frac{1}{3}e$
Leptons	$\begin{pmatrix} \nu_e \\ e \end{pmatrix}$	$\begin{pmatrix} \nu_\mu \\ \mu \end{pmatrix}$	$\begin{pmatrix} \nu_\tau \\ \tau \end{pmatrix}$	0 $-e$

Table 1: The matter particles of the Standard Model.

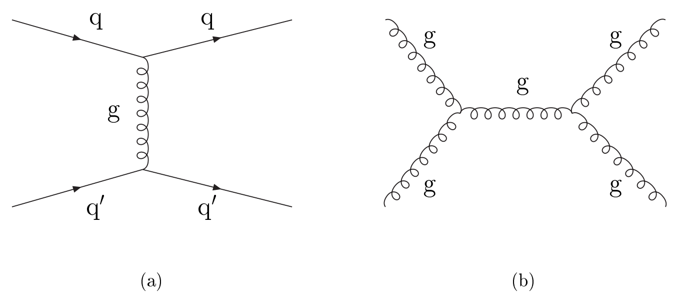

Figure 3: (a) The strong interaction between two quarks (q and q') via the exchange of a gluon (g). (b) Gluon–gluon interaction.

charge -1, all quarks have fractional electric charges. The neutron consists of one u quark and two d quarks (which together add up to give it 0 charge), and the proton is made of two u quarks and one d quark (which together add up to give it +1 charge).

It is an experimental fact that no free quarks have been observed. Instead, what are directly observable in the laboratory are the hadrons, which have no net color charge; the colored objects can only exist inside these particles. Hadrons may consist either of three quarks (baryons) or of a quark-antiquark pair (mesons). The recipe for a baryon is to take one quark of each color, in such a way that the color cancels out. For a meson the quark-antiquark pair corresponds to a system of color-anticolor (e.g. red-antired), which also results in a color neutral object.

The nature of the color force can most easily be understood by comparing it to the electromagnetic force and pointing out similarities and differences.

Just as the electromagnetic force between the electrons is generated by the virtual exchange of photons, so the strong force that binds together the quarks comes from the exchange of other force quanta: the "gluons" (the name hints on their property of glueing the quarks together to make observable white objects). The QCD analog of Fig. 2 is shown in Fig. 3a, in which two quarks interact strongly via the exchange of one gluon. A crucial difference between the two interactions arises from the different natures of the corresponding gauge bosons: while the photon of QED is electrically neutral, the eight gluons of QCD each carry a particular color-anticolor charge combination (e.g. red-antigreen), that results in a net color charge. This means that the gluons can also interact amongst each other (see e.g. Fig. 3b), in a way that the photons can not. As a result the color force behaves in a very different way from electromagnetism: at large distances it does not vanish. This property of QCD explains why colored objects such as quarks, antiquarks and gluons are permanently confined inside hadrons: the color force acts similarly to a spring that holds them together.

The process through which the quarks transform into the observed white hadrons – known as hadronization – is extremely difficult to describe using the Standard Model and is not fully understood theoretically. There exist a few phenomenological models for hadronization. The most successful example is the so-called Lund model [2], based on the idea that when we try to pull apart the quarks, the energy of the strong field that is stretched between them increases up to a point when new quark-antiquark pairs can form; these then re-group themselves in order to give rise to the observed hadrons.

The third kind of interaction, the weak interaction, is probably the least familiar one. The particles sensitive to this interaction include the quarks, as well as the electron and its "weak" partner, called the electron neutrino. Actually, there exist two more electron-like particles, the muon μ and the tau lepton τ, each one accompanied by its own neutrino. The neutrinos lack both color and electrical charge and they interact only via the weak force. The electron, the muon and the tau together with their neutrinos are collectively called "leptons", and these are shown in the lower part of Table 1.

The weak force is responsible for the so-called β-decay of a nucleus, a process in which a neutron transforms into a proton, by emitting an electron and an electron neutrino. At quark level this means that a d quark (from within the neutron) turns into a u quark (that is now part of a proton). The gauge boson of the weak force involved in this process is called W^- (cf. Fig. 4). The existence of W^- and its antiparticle, W^+, was first discussed by theoreticians in the late 1950s. Experimental evidence in favor of the existence of these force quanta first came from CERN, about twenty-five years later.

Both the electromagnetic and the weak forces can be regarded as flavor forces, since the electric charge depends on the flavor and the weak force involves the changing of flavor. During the 1950s and 1960s, Glashow, Weinberg and Salam formulated quantum flavor dynamics, incorporating both quantum electrodynamics and a theory of the weak forces; the resulting unified interaction is referred to as electro-weak interaction. The theory successfully predicted, among other things, the existence of a new flavor quantum that causes simple scattering of electron neutrinos off neutrons or protons (i.e. off d quarks or u quarks), without change of flavor. This scattering takes place through the exchange of a new, electrically neutral force quantum, called Z^0. Evidence in support of the existence of Z^0 came from the aforementioned experiment.

This completes our presentation of the matter particles of the Standard Model (cf. Table 1) and of the gauge bosons of the electro-weak and strong

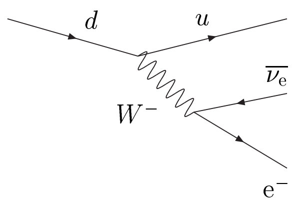

Figure 4: The β-decay process at quark level.

interactions (cf. Table 2).

The matter particles are grouped into "families". The first family consists of the u and d quarks together with the electron and its neutrino, and they make up all the matter that we see around us. The second and the third families can be seen as duplicates of the first, differing only in their being heavier. Because of this, the particles of these additional families are unstable, and eventually decay into those of the first family. This explains why in nature only particles of the first family occur.

In the formulation of the Standard Model, all particles (matter and force carrying) are initially assumed to be massless. In reality the fermions and some of the force quanta have masses, and these are not negligible. The masses of the Standard Model particles span over a wide range, starting with the massless photons and gluons at one end of the spectrum, and going up to 175 GeV (1 GeV = 10^9 eV) for the heaviest quark, t.

The mechanism through which the fundamental particles of the Standard Model aquire a mass is known as the Higgs mechanism. It involves the intro-

Interaction	Gauge Boson	Mass
Electromagnetism	γ	massless
Weak	$W^{\pm}$ Z^0	80 GeV 91 GeV
Strong	8 gluons	massless

Table 2: The gauge bosons of the Standard Model (excluding gravity).

duction of (at least) one new kind of boson, called the Higgs boson. The Higgs boson differs from the other bosons of the Standard Model. An important distinction lies in the value of its spin: while all the force quanta of quantum chromodynamics and quantum flavor dynamics have spin 1, the Higgs boson must have spin 0. Up until the time of writing of this introduction no concrete evidence has been reported on the existence of Higgs.

The Standard Model has proved very successful in describing the bulk of the experimental data observed so far. However, there are still several unanswered questions that need to be looked into.

One issue regards the necessary existence of the Higgs, that has not been proven experimentally. This boson will hopefully be discovered at the energy soon to be available at the new particle accelerator (LHC) at CERN.

Furthermore gravitation has not been incorporated into the Standard Model, as there exists no quantum theory for gravity.

Another obvious problem is the large number of fundamental particles in the Standard Model. The quarks were first introduced in order to explain the multiplicity of observed hadrons; in this sense they represent a simplification. But all in all the Standard Model has come to include a large number of fundamental particles itself. There are in total 18 quarks and 6 leptons, each having a corresponding antiparticle; this makes 48 particles. Moreover there are the force quanta of the different forces: 8 gluons, 1 photon and 3 massive bosons of the weak interaction. In total we obtain thus 60 particles and, together with the Higgs boson, 61. It seems rather improbable that the basic law of all matter in the universe could rest on such a large and mixed collection of fundamental objects.

One could only hope that a solution will come in the shape of a larger, unified theory of all the particles and all their interactions. Any such theory should incorporate the Standard Model, given the fact that the latter is supported by copious evidence from experiment. There exist several theories that attempt to do this, such as supersymmetry and string theory, but as of now they can only be regarded as speculative.

The results presented in this thesis have all been obtained within the framework of the Standard Model.

Theoretical Tools

No matter how beautiful a theory is, sooner or later it needs to be confronted with reality. It is desirable that this theory not only describes the observed phenomena, but also predicts new ones, which later experiments hopefully confirm. In this section we will present some tools that allow us to make theoretical predictions based on the Standard Model. In the subsequent section, some of the experiments, that aim to test the theory, are presented.

Because of the complex nature of the calculations that arise in most practical situations, it is an almost impossible task to use brute force to perform calculations based on the Standard Model. There are several ways out of this: one possibility is to employ approximate methods; another is to make use of computers to perform the calculations.

We begin by describing the approximate method known as "perturbation theory", applicable when the interaction that takes place is weak enough. The general idea is to expand the cross-section for a given particle collision, rewriting it as a (infinite) sum of terms, with successive terms becoming smaller and smaller in magnitude; to a good approximation, the cross-section is given by just the first few terms. The expansion variable is given by the coupling strength, which represents a measure of the strength of the interaction involved. The terms of the expansion may be visualized with the help of Feynman diagrams. For a specific reaction, the contributing Feynman diagrams are collected and so-called Feynman rules are used to convert them into scattering amplitudes; by summing and squaring these amplitudes the cross-section can be obtained.

In the case of QED, the electromagnetic field is of infinite range, with the potential decreasing with distance according to $V \sim 1/r$. This allows an expansion of the cross section in terms of $\alpha_{em} (\approx 1/137)$, which is small enough for perturbation theory to be very successful. Taking the electromagnetic interaction between an electron and a positron as an example, the cross-section for the collision may be expanded as follows:

$$\sigma = a_2 \alpha_{em}^2 + a_3 \alpha_{em}^3 + a_4 \alpha_{em}^4 + \cdots . \tag{1}$$

(The reason why the first two terms of the expansion are not included will become clear shortly.) Each term of the above expansion obtains contributions from several Feynman diagrams, such that the power of the coupling strength occurring in a specific term corresponds to the number of vertices in the diagram. The cross section thus obtains contributions from diagrams with 2 vertices (cf. Fig. 5a), diagrams with 3 vertices (cf. Fig. 5b) and so forth. The dominant contribution comes from 2-vertex diagrams, representing the simplest possible way through which the interaction can take place. (This explains why the expansion of Eq. (1) starts with the α_{em}^2 term).

In the case of QCD, more care needs to be taken because of the intricate way in which the color force works. The difference is mainly due to the way the strong coupling, α_s, varies with the resolution scale of the process. Taking as an example the case of two quarks interacting via one-gluon exchange (cf. Fig. 3a), the strong coupling will be a function of the gluon virtuality Q^2, which presents a measure of the resolution (the larger the value of Q^2, the smaller the distances that can be resolved). The coupling of the strong interaction is such that it decreases with the resolution scale Q^2, i.e. as the distances decrease. Thus, in

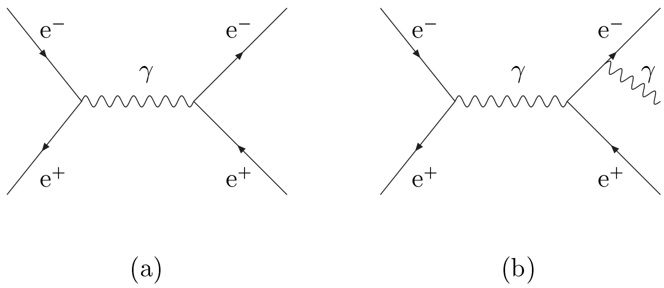

Figure 5: A 2-vertex and a 3-vertex diagram contributing to the e^{-}–e^{+} interaction.

QCD, perturbation theory is only applicable at small enough distances; here the potential varies with distance according to $V \sim 1/r$, and the interaction is dominated by one-gluon exchange, similar to the case of QED.

As the distance is increased (i.e. as Q^2 decreases), on the other hand, the strong coupling will increase up to a point when perturbative theory breaks down. At large distances, the potential depends linearly on the distance $V \sim r$, meaning that an infinite amount of energy is needed to separate the quarks from each other! As mentioned in the previous section, the parton–based picture is no longer appropriate in this case and the description should be in terms of colorless hadrons; the transition between these two regimes, i.e. the hadronization, is currently best described by phenomenological models.

Actually, in the case of QCD, perturbation theory has problems not only at low energies (i.e. low Q^2) but also at very high energies. Even though the scale Q^2 might be high enough in order to make the coupling small, the possibility for additional gluon emissions increases rapidly with the energy due to the increase in the kinematically allowed phase space. As a result the factors a_i in the expansion for the cross section of Eq. (1) become too big and the perturbative approach is no longer satisfactory. The remedy consists of resummation of the leading logarithmic behavior of the cross section to all orders.

There exist a couple of resummation methods and here we will give a brief description of these in the context of deeply inelastic scattering (DIS). Typically, a deeply inelastic electron–proton scattering event is represented by a fan diagram, as the one shown in Fig. 6. The electron emits a photon of virtuality Q^2, that interacts with a parton carrying a fraction x of the proton momentum (labelled k_n in the figure). The 4-momenta of the emitted partons are labelled

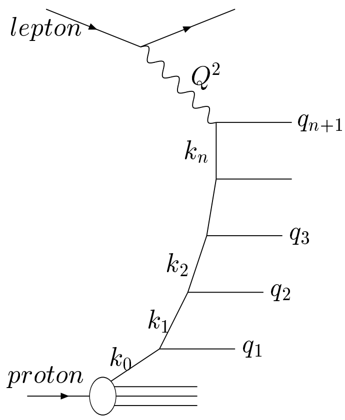

Figure 6: A fan diagram for deeply inelastic electron–proton scattering.

q_i while those of the propagators are labelled k_i.

The most familiar resummation strategy is called DGLAP [3]. It is valid in the region of asymptotically large photon virtualities, Q^2, where the dominant contributions come from fan diagrams whose propagator transverse momenta $k_{\perp i}$ are strongly ordered:

$$Q^2 \gg k_{\perp n}^2 \gg k_{\perp n-1}^2 \gg \cdots .$$

The parton distributions $f_i(x, Q^2)$ that occur in the expression for the cross-section are evolved using the so-called DGLAP evolution equation.

The second resummation strategy is BFKL [4] resummation, valid in the asymptotically small x region (or equivalently at asymptotically high energies). Here, fan diagrams whose propagators are not $k_\perp$–ordered contribute as well and need to be included. As a consequence, the parton distributions that enter in the expression for the cross-section depend on $k_\perp$ rather than on Q^2 (they are therefore referred to as $k_\perp$–unintegrated parton distributions). Their evolution, this time in the $\ln(1/x)$ variable, is given by the so-called BFKL equation.

DGLAP resummation has been very successful in describing most of the experimental results of electron–proton and proton–proton collisions. More recently, electron-proton collisions performed at the HERA accelerator (see next section) in the very-low-x and not-very-high-Q^2 regime have shown that the cross-section rises rapidly with decreasing x. Even though the DGLAP formalism can be modified to account for this behavior, the BFKL approach actually predicted it.

When attempting to give a complete picture of a particle collision, we need to consider all the different steps involved. Assuming an electron-proton collision, we need to describe the distribution of the partons inside the proton, the (perturbatively calculable) cross-section, the recoiling particles, the way in which the partons are transformed into the observed hadrons (hadronization) and how these (when heavy) decay further.

The complexity of the calculations that need to be performed rules out pure analytical descriptions. The most practical way to perform calculations and predict the outcome of experiments, that allows for energy and momentum conservation in each step involved in the calculations, is to make use of the kind of computer programs known as Monte Carlo event generators. The theories and models relevant to the different steps mentioned above are implemented in the event generators, which may then be used to simulate particle collisions.

In this context, an *event* denotes one of the many possible outcomes of a particle collision. The name Monte Carlo comes from the fact that these programs are based on stochastic techniques, meaning that they make use of (pseudo-)random numbers in order to simulate quantum mechanical processes; this is necessary because of the intrinsically non-deterministic nature of these processes.

Experimental Tools

As mentioned in the first section, the advent of particle accelerators greatly improved the experimental situation in particle physics.

Circular accelerators, like those of HERA and LHC described below, make use of electric and magnetic fields in order to force the charged particles into circular paths and accelerate them up to the desired collision energies. Since electrically charged particles, such as electrons, lose energy as their paths bend, it is necessary to build accelerators of large dimensions, thus avoiding too big an energy loss. In the case of protons, another problem arises: as they are more heavy, they are more difficult to force into curved paths. In this case it is rather the strength of the magnets employed that sets a limit on how big a curvature can be achieved. Both HERA and LHC have very large circumferences.

Usually, there are several interaction regions in a circular accelerator; this allows for several experiments to be run at the same time. The detectors employed are typically of sizes comparable to that of four storey buildings! This is due to the fact that they are composed of different layers, each having the special purpose of detecting different types of particles.

The results of this thesis apply to two different classes of experiments, namely those involving $e - p$ and $p - p$ collisions. Below we will mention some characteristics of these collisions. We will also give a short presentation of the HERA accelerator, at which $e-p$ collisions are carried out, and of LHC, where experiments involving $p-p$ collisions are to be performed.

The parton content of protons can most easily be studied by allowing the latter to interact with structureless objects, such as electrons. For this reason, the first category of events under study are high-energy $e-p$ collisions. The only electron-proton collider in the world, HERA (Hadron Electron Ring Accelerator), is situated at the DESY national laboratory [5], in Hamburg. HERA is a circular accelerator with a circumference of about 6 km and has been running since 1991. There are four experiments: two collider experiments, H1 and ZEUS, and two fixed-target experiments, HERMES and HERA-B. At HERA electrons of 30 GeV collide with protons of 900 GeV and these energetic electrons are able to probe distances of a factor 1000 smaller than the proton radius. The cross section is measured and from this proton structure functions, such as F_2, are obtained. The parton distributions, f_i, may then be extracted, the studies of which represent a test of QCD. Since the interaction between the electron and the proton is of electromagnetic nature, only the quark content of the proton can be probed directly. The gluons are electrically neutral and their distribution inside the proton can only be obtained indirectly.

The second category of experiments involves high-energy $p-p$ collisions. One difference with respect to the previous case is that the interaction will be of the strong kind, rather than electromagnetic, since the strong coupling is so much larger. As now both objects that take part in the collision are composite, the outcome is more complicated: besides the hard interaction (i.e. of large momentum transfer) between e.g. a quark from one of the protons and a quark from the other proton, there is also the possibility for soft interactions between the beam remnants. At even higher energies, so-called multiple scatterings are likely to occur, meaning that the hard interaction is accompanied by one or more semi-hard parton interactions. The resulting situation is very complex, a fact that is reflected in the multitude of particles (jets) coming out of such collisions.

Experiments involving collisions between proton beams of energies around 7 TeV each will be performed at a future collider, the LHC (Large Hadron Collider), that is to be built at the European research center CERN [6], in Geneva. Throughout the years, CERN has provided different particle accelerators. One such example is the Super Proton Synchrotron (SPS), which, when modified into a proton–antiproton collider, provided us with the experimental evidence of the W and Z particles. Another example is the Large Electron-Positron collider (LEP). The LHC is intended to take over the 27-kilometer LEP tunnel. The plan is not only to perform tests of the Standard Model, but also to look for new physics.

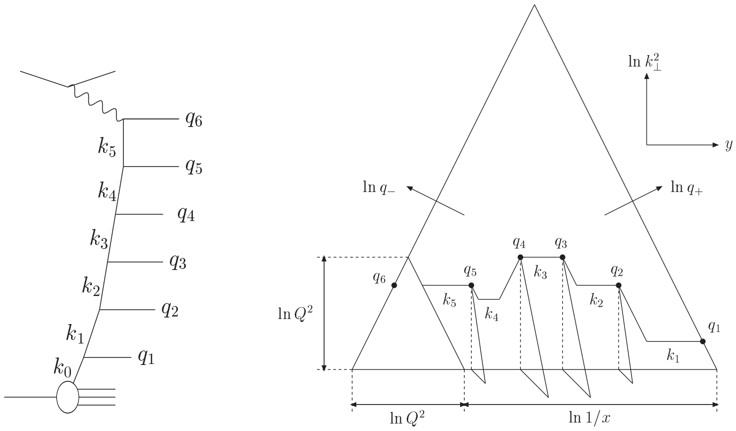

Figure 7: The initial-state emissions q_i of LDC form a chain of linked dipoles in the $(y, \kappa = \ln(k_\perp^2))$-plane. Final-state radiation is allowed in the region beneath the chain.

The Linked Dipole Chain Model

The majority of the results of this thesis have been obtained within the framework of the Linked Dipole Chain (LDC) model, first presented in [7]. Here we will only mention some of its features, while a more complete description can be found in the above reference as well as in the papers contained in this thesis.

The LDC model was originally developed for studies of deeply inelastic electron–proton collisions. It is based on an earlier developed model, the CCFM model [8], but represents a reformulation and generalization of this. Just like CCFM, the LDC model takes into account large logarithms of Q^2, à là DGLAP, and large $(1/x)$–logarithms, typical of the BFKL regime.

To the left in Fig. 7 is shown a fan diagram for deeply inelastic e–p scattering; the virtual links are labeled k_i and the outgoing partons are labeled q_i. When discussing outgoing partons, one distinguishes between *initial state radiation* (ISR) and *final state radiation* (FSR), with the separation between these depending on the model employed. The ISR partons of LDC are defined as those outgoing partons that are ordered in both light-cone components q_{i+} and q_{i-}(or equivalently in rapidity $y = 1/2 \ln{(q_+/q_-)}$), and whose transverse momenta satisfy the constraint

$$q_{\perp i} > \min(k_{\perp i}, k_{\perp i-1});$$

the remaining emissions are treated as FSR. The initial state partons form a chain of linked color dipoles in the $(y, \ln k_\perp^2)$-plane, from which the final state partons are radiated, as illustrated to the right in Fig. 7. The LDC model can be used to describe both inclusive quantities such as the proton structure function, to which only the initial state radiation contributes, and exclusive final states, after the inclusion of the final state radiation in the allowed regions of phase space.

The specific choice for the ISR–FSR separation in LDC results in a simple form for the $k_\perp$-unintegrated parton distribution:

$$\mathcal{F}(x, k_\perp^2) \quad \sim \quad \sum_n \int \prod^n \bar{\alpha}\, dz_i \frac{d^2 q_{\perp i}}{\pi q_{\perp i}^2} P(z_i)\, \Delta_S\, \delta(x - \Pi z_i)\, \delta(\ln k_\perp^2 - \ln k_{\perp n}^2)$$

Here $\bar{\alpha} \equiv 3\alpha_s/\pi$, $P(z)$ is the full gluonic splitting function with Δ_S the associated Sudakov form factor and the splitting parameter z is given by $z_i = k_i/k_{i-1}$. (The integration is over the allowed phase space, as specified above.) This expression may be written in a way that makes it fully left-right symmetric in the sense that the result is independent of whether the evolution starts at the probe (photon) or target (proton) end. Thus, the LDC formalism can easily be modified to account for proton-proton scattering by replacing the (resolved) photon by a proton.

The LDC model has been implemented in the Monte Carlo event generator LDCMC [9]. In this thesis, LDCMC was used to simulate $e-p$ and $p-p$ collisions, allowing for studies of the structure of the proton and of the subsequently produced particle jets.

The Papers

Below follows a brief description of the papers on which this thesis is based; the papers can be found in their entirety in the proceeding chapters. The majority of the results have been obtained within the framework of the Linked Dipole Chain model (LDC).

Paper I

In order to correctly interpret new phenomena that are likely to occur in future high-energy hadron-hadron or nucleus-nucleus collisions, one needs to have a good understanding of (mini)jet production and transverse energy flow. In particular one needs to consider the following two points: accounting for the virtualities of the colliding partons and avoiding double-counting in the case when there can be several hard sub-collisions.

The traditional approach – based on integrated structure functions – results in a cross section that increases rapidly at small $p_\perp$. This unphysical behavior is usually corrected in terms of the *ad hoc* introduction of a cutoff for small transverse momenta, $p_{\perp,min} \sim 2$ GeV; unfortunately, this implies that it is difficult to make predictions for other, higher, energies.

The LCD model is particularly suitable for a study of the above mentioned points. It describes the (mini)jet cross section in a $k_\perp$-factorized formalism, i.e. in terms of $k_\perp$-unintegrated structure functions and off-shell sub-collision cross sections; thus the virtualities of the colliding partons are taken into account. Furthermore, it is formulated in such a way as to make the description completely symmetric with respect to evolution from the target or projectile end; as a consequence the double-counting is easily corrected for in this formalism.

In this article we present qualitative results for the inclusive jet cross section and the transverse energy flow, based on analytic calculations which make use of an approximate version of LDC; the approximation consists of only including purely gluonic chains and using the leading expression for the parton-parton cross section. The results contain a dynamical suppression at small $p_\perp$, indeed of the order 2 GeV, that corresponds to an effective cutoff that is slowly increasing with the total collision energy.

For quantitative estimates of the above observables, we would need to take into account also effects from non-asymptotic energies and the contributions from quarks and non-leading terms in the parton-parton cross section. This is most easily done with the LDC based event generator LDCMC, and it is done in paper IV.

Paper II

In this paper we present a simple model that interpolates between the DGLAP regime – characterized by large $k_\perp^2$ and moderate $\ln(1/x)$ – and the BFKL regime – valid when $1/x$ is large and $k_\perp^2$ is moderate – in deeply inelastic electron-proton scattering. The model, which is based on the CCFM and LDC models, is simple enough in order to give an intuitive qualitative picture of the transition region between the two domains. It is relevant for small x, having a smooth transition between the large-$k_\perp^2$ region, where ordered chains dominate, and the small-$k_\perp^2$ region, where non-ordered chains become important.

To begin with, we only keep the leading terms in $\ln(1/x)$ (thus, in the case of large $k_\perp^2$, this corresponds to the double log approximation rather than to the DGLAP regime) and derive expressions for the non-integrated gluon structure functions for both fixed and running coupling. Assuming a fixed coupling, the transition between the domains occurs at a constant ratio between $\ln k_\perp^2$ and $\ln(1/x)$,

$$\frac{\ln k_\perp^2}{\ln(1/x)} \approx e\overline{\alpha},$$

where $\overline{\alpha} = 3\alpha_s/\pi$. In the case of a running coupling, the transition occurs instead for a constant ratio between $\ln\ln k_\perp^2$ and $\ln(1/x)$,

$$\frac{\ln\ln k_\perp^2}{\ln(1/x)} \approx \frac{\lambda^2}{\alpha_0},$$

with α_0 defined by the relation $3\alpha_s/\pi = \alpha_0/\ln k_\perp^2$ and with λ being the BFKL exponent.

Including some non-leading effects in $\ln(1/x)$ mainly results in a reduction of the value of the BFKL exponent.

Paper III

When calculating e.g. the cross section for jets and heavy quarks in the case of very high energies (i.e. very small x), the effects of finite transverse momenta of partons inside the hadrons become increasingly important. These effects can be systematically accounted for by making use of a formalism based on $k_\perp$-factorization, in which the cross-section for any given physical process is given as a convolution of off-shell ($k_\perp$-dependent) partonic cross-sections and $k_\perp$-unintegrated parton distribution functions. Since the latter are not observables, their definition and properties depend strongly on the choice of formalism.

In this paper we present results for the integrated and unintegrated gluon distribution functions according to the LDC model, obtained with the LDCMC. We compare them with those obtained in other formalisms, in particular those from the CCFM model obtained from the SMALLX and CASCADE event generators, and demonstrate how to make a relevant comparison between the models.

The unintegrated parton distribution functions of the CCFM model depend sensitively to two different scales: $k_\perp$, which is the transverse momentum of the interacting parton, and $\overline{q}$, which determines an angle beyond which there is no (quasi-)real parton in the initial-state radiation chain. Many of the gluons which in the CCFM make up the initial-radiation chain are treated in LDC as final-state radiation, meaning that most of the problem of angular ordering is postponed to the treatment of the final-state radiation. As a result the LDC unintegrated gluon distribution function depends weakly on the second scale, $\overline{q}$, and this dependence can be ignored to leading $\ln(1/x)$.

When studying the $\overline{q}$-dependence of the CCFM gluon distribution function, for fixed $k_\perp$, we observe that it saturates for $\overline{q} \gtrsim 2k_\perp$, before it falls off for larger $\overline{q}$-values. As this corresponds to typical values of $\hat{t}$ and $\hat{s}$, we suggest that for a relevant comparison between the different formalisms, $\overline{q}$ should to be chosen in this saturation region. Indeed, we thus find a reasonable agreement, not only between LDC and CCFM, but also with e.g. the two-scale formalism presented by Kwiecinski, Martin and Ryskin, and the one-scale formalism of Kwiecinski, Martin and Sutton. We actually also notice a rather good agreement with the DGLAP-based result, that uses the derivative of the distribution function GRV98.

Paper IV

In this article we present a new approach for studying hadronic interactions, which makes use of a modified version of the LDC model for DIS.

At high energies, the properties of hadronic collisions seem to be dominated by hard and semi-hard parton sub-collisions. Although the parton-parton collisions are of perturbative nature, effects of non-perturbative character also contribute, and need to be incorporated using phenomenological models.

The traditional approach of collinear factorization results in an inclusive sub-collision cross section which is divergent for small $p_\perp$. This introduces the need for a soft cutoff, whose value has to be fitted to experimental data. The LDC model for DIS uses the $k_\perp$–factorization approach and includes non-$k_\perp$-ordered chains, expected to be important for limited $p_\perp$ and high energies. The symmetric character of LDC, with respect to the photon and proton ends of the parton chain, also makes it suitable for describing hadronic interactions. We find that the number of parton chains per $p-p$ collision is fixed by fits to F_2 data from HERA only, and thus less sensitive to a soft cutoff.

In hadronic interactions the inclusive cross section for parton-parton sub-collisions is known to exceed the total non-diffractive cross section. This means that on average there are more than one hard sub-collision per event and these may be correlated. In the LDC model, some correlations are already accounted for since non-$k_\perp$-ordered chains correspond to the possibility of several hard sub-collisions in one chain. Moreover, we expect the number of chains per event to be larger for more central events than for peripheral ones. Here we study two different distributions for the impact parameter dependence, one purely stochastic and one similar to the double Gaussian distribution of PYTHIA.

Another non-perturbative effect concerns color connections, as the scattered partons must be color connected with each other and with the beam remnants. In this preliminary study we focus on features of jet and minijet production, that are less sensitive to the hadronization effects and postpone a more rigorous treatment of color connections to future work. Thus we compare our results at parton level with corresponding results based on PYTHIA.

We test our approach by applying it to $p-p$ collisions of $\sqrt{s} = 1.8$ TeV. We find that the results based on our two versions agree with those of PYTHIA, on a qualitative level. Our version with uncorrelated chains results in larger fluctuations than the corresponding model with uncorrelated scatterings in PYTHIA, as our chains already include some correlations between multiple scatterings in the same chain. Including correlations from our geometrical chain distribution increases the fluctuations, though not to the level of the corresponding model in PYTHIA based on a double Gaussian impact parameter dependence. This is mainly due to our energy conservation procedure, which suppresses large chain-multiplicities to a larger extent.

In the future, after the color connections have been analysed in more detail and accounted for, we are confident that our model will be able to describe essential features of high energy hadronic collisions, including underlying events and jet-pedestal effects in high $E_\perp$ events.

Acknowledgments

My gratitude goes to my supervisor, Professor G. Gustafson, as well as to Associate Professor L. Lönnblad and Professor T. Sjöstrand. The support received from you all has been invaluable!

I would also like to thank my fellow Ph.D. students and post docs, with a very special “thank you” to S. Mohanty.

References

[1] M. Breidenbach *et al.*, *Phys. Rev. Lett.* **23** (1969) 935.

[2] B. Andersson, G. Gustafson, G. Ingelman and T. Sjöstrand, *Phys. Rep.* **97** (1983) 31.

[3] V. N. Gribov and L. N. Lipatov *Yad. Fiz.* **15** (1972) 781–807.
L. N. Lipatov *Sov. J. Nucl. Phys.* **20** (1975) 94–102.
G. Altarelli and G. Parisi *Nucl. Phys.* **B126** (1977) 298.
Y. L. Dokshitzer *Sov. Phys. JETP* **46** (1977) 641–653.

[4] E. A. Kuraev, L. N. Lipatov, and V. S. Fadin *Sov. Phys. JETP* **45** (1977) 199–204.
I. I. Balitsky and L. N. Lipatov *Sov. J. Nucl. Phys.* **28** (1978) 822–829.

[5] http://www.desy.de/

[6] http://www.cern.ch/

[7] B. Andersson, G. Gustafson, J. Samuelsson, Nucl. Phys. **B467** (1996) 443.

[8] M. Ciafaloni *Nucl. Phys.* **B296** (1988) 49.
S. Catani, F. Fiorani, and G. Marchesini *Phys. Lett.* **B234** (1990) 339.

[9] H. Kharraziha and L. Lönnblad *JHEP* **03** (1998) 006, `hep-ph/9709424`.

Minijets and Transverse Energy Flow in High Energy Collisions

Paper I

Minijets and Transverse Energy Flow in High Energy Collisions

Gösta Gustafson and Gabriela Miu

Department of Theoretical Physics
Lund University, Sölvegatan 14A, S-223 62 Lund, Sweden

Physical Review **D63**, 034004 (2001)

Abstract

When studying the production of minijets and transverse energy flow in high energy hadron-hadron or nucleus-nucleus collisions, two essential points have to be taken into account. First, one has to account for the virtuality of the colliding partons and secondly, it is important to avoid double counting, when many links in a parton chain can be interpreted as the momentum transfer in a hard subcollision. The Linked Dipole Chain model, introduced for low-x DIS, is particularly suitable for a study of these problems. It describes (mini)jet production in a $k_\perp$factorizing formalism, which includes all links in a parton chain on an equal footing, avoiding double counting. In a "naive" calculation based on integrated structure functions, the cross section blows up for small $p_\perp$, which makes it necessary to introduce a soft cutoff. In our approach we find a dynamical suppression at low $p_\perp$, which makes it possible to extrapolate to higher energies and make more reliable predictions for RHIC and LHC.

1.1 Introduction

With increasing energies in hadron-hadron or nucleus-nucleus collisions, the cross section for hard subcollisions increases and becomes more and more important. The amount of minijets and transverse energy becomes essential for understanding the background in searches for new particles or new phenomena at the LHC as well as for the "initial conditions" in nucleus-nucleus collisions. In calculations of the flow in either a quark-gluon plasma or a hadronic phase, the results are very sensitive to the properties of the initial parton state which resulted from a large number of hard subcollisions. Thus a reliable estimate of these initial conditions is essential for the interpretation of signals from a possible plasma formation in experiments at RHIC or LHC.

At high $q_\perp$ the jet cross section can be described by a product of structure functions describing the flux of partons and the cross section for a hard partonic subcollision. Symbolically we write (cf. Fig. 1.1a)

$$\frac{d\sigma}{dq_\perp^2} \sim F(x_1, q_\perp^2)\, F(x_2, q_\perp^2)\, \frac{d\hat{\sigma}}{dq_\perp^2}. \tag{1.1}$$

This is a relevant description when $q_\perp$ is so large that the structure functions can be described by DGLAP evolution, i. e. by $k_\perp$-ordered chains from the incoming hadrons towards the hard subcollision. In the hard collision cross section, $d\hat{\sigma}/dq_\perp^2$, the colliding partons are then approximately on shell. For smaller $q_\perp^2$ and/or larger energies (which implies smaller x-values) we enter the BFKL region, in which non-ordered chains are important. This has two essential consequences:

i) The virtuality of one or both of the colliding partons ($k_{\perp 1}^2$ and/or $k_{\perp 2}^2$ in Fig. 1.1a) can be larger than the momentum transfer $q_\perp^2$. This implies that the virtualities of the colliding partons have to be taken into account. This can be achieved by means of nonintegrated structure functions and off-shell subcollision cross sections.

ii) In a chain with non-ordered $k_\perp$-values a single hard subcollision cannot be isolated. There may be several links in a single chain, which can be regarded as a hard collision. This situation can be analyzed in a formalism in which every link in Fig. 1.1 can be regarded as a hard subcollision. This implies that each final state parton is active in two different subcollisions. (The number of links in the chain determines both the number of subcollisions and the number of final state partons.) Therefore special care has to be taken to avoid double counting.

A formalism for DIS which interpolates between the DGLAP and BFKL regions, and which describes both the cross section and the final state properties, was developed by Ciafaloni, Catani, Fiorani, and Marchesini [1]. This or equivalent formalisms can be used e. g. to calculate the production of heavy

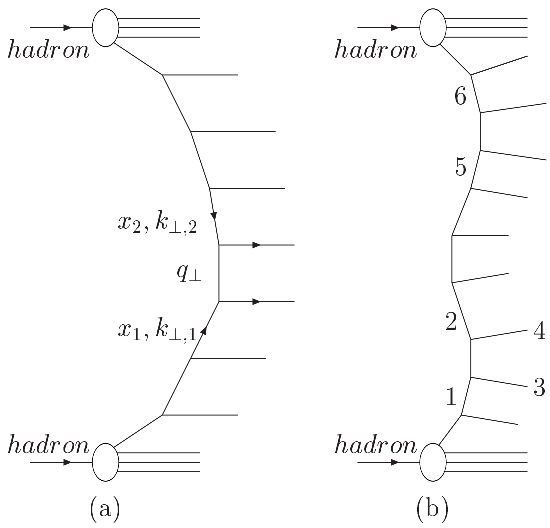

Figure 1.1: A fan diagram for a hadron-hadron collision.

quarks in hadronic collisions. In this reaction there is a single link which contains the heavy quark, and the CCFM formalism or the semihard approach can be used to calculate the unordered evolution towards the heavy quark from the projectile and the target ends [2]. Thus these formalisms can be used to solve problem i) above.

For non-$k_\perp$-ordered chains the single diagram in Fig. 1.1 can correspond to many hard subcollisions, e. g. $1+2 \to 3+4$ and $5+6 \to 7+8$ in Fig. 1.1b. For the first reaction, $1+2 \to 3+4$, the section of the ladder between partons 2 and 5 should be regarded as an evolution from the top (projectile) end, while for the reaction $5+6 \to 7+8$ the same section should be regarded as an evolution from the lower (target) end of the chain. A description of this process is most simple in a formalism in which the evolution is explicitly symmetric between the two ends. It is also essential that the formalism can be interpreted in terms of production probabilities for exclusive final states. The symmetry is not a trivial feature for the following reason. The fan diagrams in Fig. 1.1 should be regarded as the initial state radiation. To get the complete final state, final state emission has to be added in specified kinematic regions. The separation between initial state and final state emission is not determined by Nature, but is defined by the calculation scheme, and therefore the regions for final state emission depend on the formalism used. In the CCFM approach this separation is not symmetric, and consequently also the initial state ladder is asymmetric. Thus the CCFM formalism is not immediately convenient to describe many subcollisions in a single chain, and thus to solve problem ii) above.

The final state emission, when one gluon is split into two, should not significantly affect the flow of energy. Note, however, that the distribution of produced gluons is not a uniquely defined quantity. Besides the arbitrariness in the separation between initial and final state emission, discussed above, also the final state radiation depends on the resolution chosen in the definition of an individual gluon, i. e. on the cut-off in the final state cascades.

The Linked Dipole Chain (LDC) model [3, 4] is a reformulation and generalization of the CCFM formalism. The separation between initial and final state radiation is chosen in such a way that the description is explicitly symmetric between the projectile and target ends of the ladder. It can within a single formalism describe different types of events, "normal DIS", boson-gluon fusion events, and events with hard subcollisions in resolved photon events. For such a resolved photon event the result can be directly interpreted as evolutions from both the proton and the photon ends towards a hard parton-parton collision. This feature implies that the LDC model is also particularly suitable for a description of hard collisions in hadronic interactions. For any link in the ladder, the contribution can be directly interpreted as evolution from the two ends multiplied by an off-shell parton-parton cross section for the link under study. This symmetry property of the LDC model makes it useful in solving problem ii) above (the double-counting is easily corrected for in this formalism).

It is well known that the BFKL formalism with a constant coupling, α_s, implies that the transverse momenta grow like a random walk in y or in $\ln 1/x$ (what is called Bartels' cigar). For a running α_s we obtain instead a saturation of the $k_\perp$-distribution [4]. Therefore very large chains develop a central plateau in rapidity. This means that with increasing beam energy the transverse energy density in each chain will stay limited, although the total $dE_\perp/dy$ will increase as the number of possible chains grows with energy. The fact that the $k_\perp$-distribution stays limited also for high energies implies that the result is sensitive to soft nonperturbative physics, and thus depends on a necessary cut-off for small $k_\perp$. This cut-off can, however, be fixed by a phenomenological fit to experimental data for $F_2(x, Q^2)$, and therefore does not imply a large extra uncertainty.

When comparing our result with the "naive" expression in eq. (1.1) we find that the latter significantly overestimates the cross section for smaller $q_\perp$. In order to agree with experimental data for $E_\perp$-flow, many calculations based on eq. (1.1) introduce a cutoff for small $q_\perp$ of the order 2 GeV/c [5]. This implies, however, that it is difficult to make predictions for higher energies. Without a dynamical understanding of the origin of the overestimate, it is not possible to judge how an effective cut-off should vary with energy. The dynamical suppression in our formalism corresponds to such an effective cut-off, indeed of the order 2 GeV/c, which is growing slowly with the total collision energy.

The results in this paper are mainly based on approximate analytic calculations, which demonstrate the qualitative features. In a future publication we want to present more detailed results based on MC simulations, where e. g. corrections from quark lines, subleading terms in the splitting functions and exact energy-momentum conservation, are also taken into account.

1.2 DIS

A deep inelastic scattering event is generally described in terms of a fan diagram as shown in Fig 1.2. Here q_i denote quasireal partons emitted as initial state radiation, while the links k_i are virtual. The dashed lines denote final state emission, which is assumed to be emitted without changing the cross section and with negligible recoils for the emitting partons q_i.

In the large Q^2 region, the DGLAP region, the dominant contributions come from ordered chains which satisfy $Q^2 > k^2_{\perp,n} > ... > k^2_{\perp,i} > k^2_{\perp,i-1}$ and

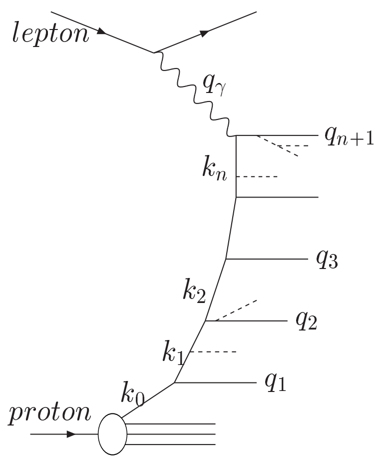

Figure 1.2: A fan diagram for a DIS event. The quasireal partons from the initial state radiation are denoted q_i, and the virtual propagators k_i. The dashed lines denote final state radiation.

$k_{+,i} > k_{+,i+1}$. Each such chain gives a contribution ($x_i \equiv k_{+,i}/P_{+,tot}$)

$$\prod_i^n \bar{\alpha} \frac{dx_i}{x_i} \frac{dk_{\perp,i}^2}{k_{\perp,i}^2} \quad \text{where} \quad \bar{\alpha} \equiv \frac{3\alpha_s}{\pi}. \tag{1.2}$$

Integrating over the appropriate integration regions and summing over possible values of n, the number of links in the chain, we readily obtain (for a fixed coupling $\bar{\alpha}$)

$$F(x, Q^2) \sim \sum_n \bar{\alpha}^n \frac{(\ln 1/x)^n}{n!} \frac{(\ln Q^2)^n}{n!} \approx \exp(2\sqrt{\bar{\alpha} \ln Q^2 \ln 1/x}). \tag{1.3}$$

For a running coupling we get instead of $\ln Q^2$ a factor $\ln \ln Q^2$. We want to stress that to get the properties of the *final state*, we have to add final state emission within regions allowed by angular ordering.

For very small x and limited Q^2, the BFKL region, also non-ordered chains become important, although suppressed. Solutions to the BFKL equation [6] increase like a power $1/x^\lambda$ for small x-values. Such a power-like behavior with $\lambda \sim 0.3$, is indicated in data on F_2 from HERA. (We note, however, that it is also possible to describe this increase by NLO DGLAP evolution.)

In the interpolation region between the DGLAP and BFKL regimes we have to calculate suppressed contributions from non-ordered chains. For each chain of initial state radiation, final state emission should be added within specified kinematic regions. This final state radiation should give negligible recoils. It should also be described by Sudakov form factors, which implies that the final state emission only affects the properties of the final state and not the cross section (i. e. the reaction probability), which is described by the structure function. Thus a chain with specified initial state radiation represents a set of final states with all possible final state emissions within the allowed regions. We want to stress that the separation between initial and final state radiation is not given by Nature, but is defined by the calculation scheme.

A specific scheme, which interpolates between the DGLAP and the BFKL results, was presented by Ciafaloni, Catani, Fiorani and Marchesini, the CCFM model [1]. In this scheme those final state gluons, which are not followed in rapidity (or angle) by a more energetic gluon, are regarded as initial state radiation, all other as final state emission. With this definition they showed that for small x the nonintegrated structure function, f, is given by the expression (see ref [1] for details)

$$\begin{aligned} f(x, k_\perp^2, q^2) \quad \sim \quad & \sum_n \int \prod^n \bar{\alpha} \frac{dz_i}{z_i} \frac{d^2 q_{\perp,i}}{\pi q_{\perp,i}^2} \Delta_{ne}(z_i, k_{\perp,i}^2, q_i^2) \times \\ & \delta(x - \Pi z_i) \delta(k_\perp^2 - k_{\perp,n}^2) \delta(q^2 - q_n^2). \end{aligned} \tag{1.4}$$

Here $q_{\perp,i}$ and $k_{\perp,i}$ are the transverse momentum of the real and virtual partons as indicated in Fig. 1.2, and the variable q is defined by the relation $q \equiv q_\perp/(1-z)$, and the function $\Delta_{ne}(z, k_\perp^2, q^2)$ is a specific non-eikonal form factor. The integration region is restricted by the relation

$$q_{\perp,i+1} > z_i q_{\perp,i}/(1-z_i) \tag{1.5}$$

which follows from angular ordering, and by the kinematic constraint (called the consistency constraint)

$$k_{\perp,i}^2 > z_i q_{\perp,i}^2. \tag{1.6}$$

We note that this nonintegrated structure function $f(x, k_\perp^2, q^2)$ depends on two scales, $k_\perp$ which defines the transverse momentum of the last link in the chain, and q which depends on the angle of the last emission, and therefore specifies the boundary of the angular region in which later emissions are allowed.

1.3 The Linked Dipole Chain Model

The Linked Dipole Chain model [3] (LDC) is a reformulation and generalization of the CCFM model. In the LDC model more gluons are treated as final state radiation. The remaining (initial state) gluons are ordered both in q_+ and in q_-. (This implies that they are also ordered in angle or rapidity y.) Thus a single chain in the LDC model represents a set of chains in the CCFM scheme, all with the same "backbone" of harder gluons. In ref [3] it is demonstrated that if we sum over all states in this set, with their corresponding non-eikonal form factors, then all this adds up to unity. Thus the form factors are exactly canceled, and a nonintegrated structure function $\mathcal{F}$ can be written in the simple form

$$\begin{aligned} \mathcal{F}(x, k_\perp^2) \quad \sim \quad & \sum_n \int \prod^n \bar{\alpha} \frac{dz_i}{z_i} \frac{d^2 q_{\perp,i}}{\pi q_{\perp,i}^2} \theta(q_{+,i-1} - q_{+,i}) \times \\ & \theta(q_{-,i} - q_{-,i-1}) \delta(x - \Pi z_i) \delta(\ln k_\perp^2 - \ln k_{\perp,n}^2). \end{aligned} \tag{1.7}$$

We note in particular that this result is symmetric in q_+ and q_-. (An essential point for this symmetry and the cancelation of the non-eikonal form factors is the consistency constraint in eq. (3.10).) The fact that the ordering in both q_+ and q_- also automatically implies an ordering in y (i. e. in angle), means that the nonintegrated structure function $\mathcal{F}(x, k_\perp^2)$ depends only on *one* scale, $k_\perp^2$. (In contrast, the corresponding form factor, $f(x, k_\perp^2, q^2)$, in the CCFM model also depends on the scale q^2, related to the boundary of the angular region allowed for further emissions.) This fact implies a considerable simplification of the formalism. The symmetry also implies that the chain in Fig 1.2 can be interpreted either as evolving from bottom to top (i. e. from the proton end towards the photon) or evolving from top to bottom (from the photon towards the proton). This feature will be essential for our analysis of the minijet distribution.

Fig. 4.3 shows a typical chain in a $(y, \ln q_\perp^2)$-plane. The real emitted partons q_i are mapped onto points in this figure. The lightcone components $\ln q_\pm = \pm y + \frac{1}{2}\ln q_\perp^2$ grow in the upper right and upper left directions as indicated in the figure. The virtual propagators do not have a well defined rapidity; they are represented by horizontal lines, whose left ends correspond to the values of $k_{\perp,i}$ and $k_{+,i}$, while the right ends correspond to $k_{\perp,i}$ and $k_{-,i}$. The larger region allowed for final state radiation in the LDC model corresponds to the region below the horizontal lines in Fig. 4.3.

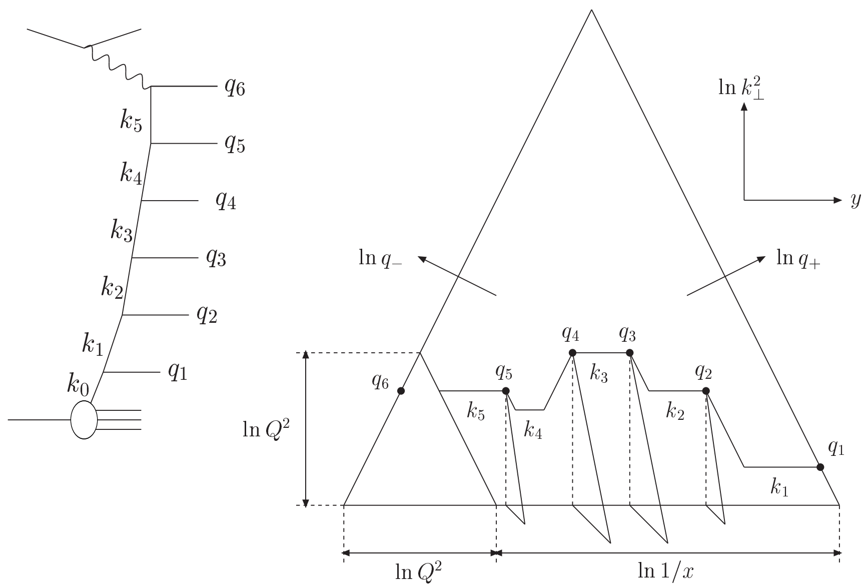

Figure 1.3: The initial state emissions q_i in the $(y, \kappa = ln(k_\perp^2))$-plane. Final state radiation is allowed in the region below the horizontal lines.

It is convenient to express the result in terms of the propagator momenta k_i, using the relations $d^2q_{\perp,i} = d^2k_{\perp,i}$ and $q_{\perp,i}^2 \approx \max(k_{\perp,i}^2, k_{\perp,i-1}^2)$. Thus eq. (1.8) can be written in the form

$$\mathcal{F} \sim \sum \int \prod \bar{\alpha} \frac{dz_i}{z_i} \frac{dk_{\perp,i}^2}{\max(k_{\perp,i}^2, k_{\perp,i-1}^2)}. \tag{1.8}$$

where we have suppressed the θ- and δ-functions. This result implies that for a "step up" or a "step down" in $k_\perp$ we find the following weights

$$\frac{d^2 q_{\perp,i}}{q^2_{\perp,i}} \approx \frac{d^2 k_{\perp,i}}{k^2_{\perp,i}}, \quad k_{\perp,i} > k_{\perp,i-1} \quad \text{and} \tag{1.9}$$

$$\frac{d^2 q_{\perp,i}}{q^2_{\perp,i}} \approx \frac{d^2 k_{\perp,i}}{k^2_{\perp,i}} \cdot \frac{k^2_{\perp,i}}{k^2_{\perp,i-1}}, \quad k_{\perp,i} < k_{\perp,i-1}. \tag{1.10}$$

Thus for a step down we have an extra suppression factor $k^2_{\perp,i}/k^2_{\perp,i-1}$. This implies that if the chain goes up to $k_{\perp,max}$ and then down to $k_{\perp,final}$ we obtain the factor

$$\prod \frac{dk^2_{\perp,i}}{k^2_{\perp,i}} \cdot \frac{k^2_{\perp,final}}{k^2_{\perp,max}}. \tag{1.11}$$

This gives a factor $1/k^4_{\perp,max}$, which corresponds to a hard parton-parton subcollision.

In DIS also chains for which $k^2_{\perp,final} > Q^2$ can contribute to the cross section. These chains correspond to boson-gluon fusion events, and the definition of the structure function $F(x, Q^2)$ implies that these contributions contain a similar suppression factor $Q^2/k^2_{\perp,final}$. Thus the relation between the integrated and the nonintegrated structure functions, sometimes symbolically written as $F(x, Q^2) \sim \int \frac{dk^2_\perp}{k^2_\perp} \mathcal{F}(x, k^2_\perp)$, is more explicitly given by the relation

$$F(x, Q^2) = \int^{Q^2} \frac{dk^2_\perp}{k^2_\perp} \mathcal{F}(x, k^2_\perp) + \int_{Q^2} \frac{dk^2_\perp}{k^2_\perp} \mathcal{F}(x \frac{k^2_\perp}{Q^2}, k^2_\perp) \frac{Q^2}{k^2_\perp}. \tag{1.12}$$

In the second term, besides the suppression factor $Q^2/k^2_\perp$ we have also a shifted x-value. ‘ ‘Normal" chains, for which $k^2_{\perp,final} < Q^2$, end on the line AB in Fig. 1.4, which corresponds to $k_{+,final} = x \cdot P_{+,tot}$, but due to energy-momentum conservation, chains for which $k^2_{\perp,final} > Q^2$ end instead on the line AC, which corresponds to $k_{+,final} = x \cdot \frac{k^2_{\perp,final}}{Q^2} \cdot P_{+,tot}$. Note that the relation in eq. (1.12) is a leading approximation valid when $k^2_\perp$ is either much smaller or much larger than Q^2. Exact energy-momentum conservation implies that the argument in $\mathcal{F}$ should be $x(k^2_\perp + Q^2)/Q^2$, which approaches x or $xk^2_\perp/Q^2$ in the two limits. The exact kinematic relation is included in the MC in the whole chain including this final vertex. Our experience indicates that the approximations presented here are sufficient to understand the essential properties.

We see that in the LDC model different types of reactions are treated in the same formalism, without double counting or missed parts of phase space. Thus Fig. 1.4 shows three chains representing different types of reactions:

I. "normal" DIS,

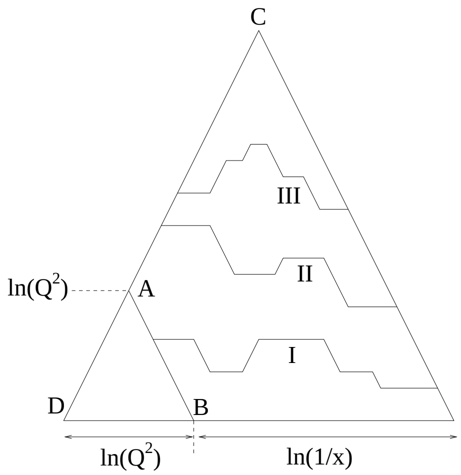

Figure 1.4: Different types of parton chains. I: "Normal" DIS. II: Boson-gluon fusion. III: Hard resolved photon collision.

II. boson-gluon fusion: $k^2_{\perp,final} > Q^2$,

III. hard resolved photon collision: $k^2_{\perp,max} > k^2_{\perp,final}(> Q^2)$.

As mentioned above, the LDC formalism is fully *left-right symmetric*, meaning that the same result is obtained if the chain is generated from the photon end instead of from the proton end. Although not evident from eq. (1.8), this is obvious from the expression in eq. (1.8). This feature also means that the same formalism can be used if the (resolved) photon in one end of the chain is replaced by a hadron. In section 5 we will see that the symmetric property of the LDC formalism makes it particularly effective for an understanding of the minijet distribution in hadronic reactions or nucleus-nucleus collisions. It is also important that the result in eq. (1.8) not only describes inclusive properties, but can be interpreted as the production probability for an exclusive final state.

Before we go into more details about the properties of this minijet plateau, we want to mention some other properties of the LDC model:

- It is straight forward to allow for a running coupling α_s within the formalism.
- It is possible to include quarks and other non-leading effects (non-leading terms in the splitting functions and exact energy-momentum conservation). The result is also improved when the link with highest $p_\perp$ is adjusted to the exact matrix element.

- The chains contain only those gluons (or quarks), which cannot be regarded as final state radiation. This might be called the "backbone" of the chain, and the fact that hard jets are not yet subdivided into many sub-jets may make it more easy to study minijets and $E_\perp$-flow, and to interpret the results of the calculations.
- The fact that there are fewer gluons in the primary chain also implies that typical z-values are smaller, and therefore smaller sub-leading effects are expected.
- The formalism is suitable for MC simulation. Such a program is developed by Lönnblad and Kharraziha [7].

Naturally it is essential to verify that the LDC model also can reproduce experimental data. Preliminary results indicate that the LDC MC indeed is able to successfully describe experimental results, both for the structure functions and for the properties of the final states, for example the production of jets and transverse energy flow [8].

1.4 Integral equations and asymptotic behavior

It is straight forward to derive integral equations for the non-integrated structure function $\mathcal{F}$. From the relation in eq. (1.12) we obtain the equation

$$\frac{\partial \mathcal{F}(l,\kappa)}{\partial l} = \int_{\kappa_0}^{\kappa} d\kappa' \bar{\alpha}(\kappa)\mathcal{F}(l,\kappa') + \int_{\kappa} d\kappa' \bar{\alpha}(\kappa')\mathcal{F}(l+\kappa-\kappa',\kappa') exp[-(\kappa'-\kappa)] \tag{1.13}$$

where $l \equiv \ln(1/x)$ and $\kappa \equiv \ln k_\perp^2$.

It is well known that the BFKL formalism with a constant coupling, α_s, implies that the transverse momenta grow like a random walk in $\ln k_\perp^2$, which gives a Gaussian distribution that widens with $\ln(1/x)$, $<\ln k_\perp^2> \sim \sqrt{\ln(1/x)}$. A running coupling favors smaller $k_\perp$-values, and this implies that the $k_\perp$-distribution does not widen indefinitely, but saturates for small x [4]. The solution to eq. (1.13) can then be written in the factorized form

$$\mathcal{F} \approx \frac{1}{x^\lambda} \cdot f(\kappa), \quad x \text{ small.} \tag{1.14}$$

The fact that small $k_\perp$-values are not suppressed implies that the evolution and the value of λ is sensitive to the soft region, and therefore cannot be determined from perturbative QCD alone. (This feature is consistent with the very large lower order corrections to the BFKL equation [9], which indicates that the perturbative series may converge badly.) This implies that some kind of cutoff, Q_0, has to be introduced, and determined from fits to experimental data. If this cutoff is determined from fits to data on F_2 from DIS, then this result can be used in our calculation of the minijet distribution in hadronic collisions. Although the dependence on x and $k_\perp$ factorizes as expressed in eq. (1.14), the two factors are not independent. The relation in eq. (1.13) implies a correlation such that the power λ also determines the $k_\perp$-dependence. Thus for large $k_\perp$, f takes the asymptotic form

$$f(\kappa) \propto \kappa^{\frac{\alpha_0}{\lambda}-1} \tag{1.15}$$

where α_0 is defined by the relation

$$\bar{\alpha} \equiv \frac{3\alpha_s}{\pi} \equiv \frac{\alpha_0}{\ln(Q^2/\Lambda^2)} \quad \Rightarrow \quad \alpha_0 = \frac{36}{33-2n_f}. \tag{1.16}$$

Actually MC calculations show that the simple power in eq. (1.15) is a surprisingly good approximation, not only for large values of $k_\perp$ (or $\kappa = \ln(k_\perp^2/\Lambda^2)$) but for the whole $k_\perp$-interval [4].

The factorized form in eq. (1.14) implies also, that for limited Q^2 and very small x (or hadronic collisions at very high energies) a central plateau is developed in the minijet distribution. The properties of this plateau will be further studied in the next section.

1.5 Inclusive Jet Cross Section

In this section we present asymptotic results and general properties. A more detailed analysis will be presented in a future publication.

The properties of the fan diagram in Fig 1.2 depend on the chosen separation between initial state and final state radiation. As mentioned above, the same event corresponds to a chain with fewer links in the LDC formalism than in e. g. the CCFM formalism, because in the LDC model more emissions are formally treated as final state radiation. The number of jets is not a well-defined concept, if it is not accompanied by some specification of the resolution, and two different schemes can be equally correct if one jet in one scheme corresponds to two or more sub-jets in the other. The total $E_\perp$-flow is however expected to be approximately unaffected, when one jet is split in two or several smaller jets by final state radiation. As mentioned in section 3, the LDC formalism is fully symmetric with respect to the two ends of the fan or ladder diagram, and we will see that this makes it particularly effective for an analysis of the minijet distribution. (In the CCFM formalism the fan diagram for the initial state radiation is not symmetric; the symmetry is restored only after inclusion of the final state emission.) It is also important that the formalism can be interpreted in terms of production probabilities for exclusive final states.

A long chain as in Fig. 1.5, with a soft probe ($Q^2 \approx Q_0^2$) and with a local maximum $k_{\perp,max} = k_{\perp,i}$, corresponds to a hard scattering between two partons with momenta k_{i-1} and $-k_{i+1}$. Due to the symmetry of the expression in eq. (1.8), these two pieces of the chain can be interpreted as evolution from both ends towards the central hard scattering. The momentum transfer in this hard subcollision is given by k_i, and there is a minus sign in the momentum of one of the colliding partons, as this part of the chain is regarded as evolving from the top of the fan diagram, downwards towards $-k_{i+1}$.

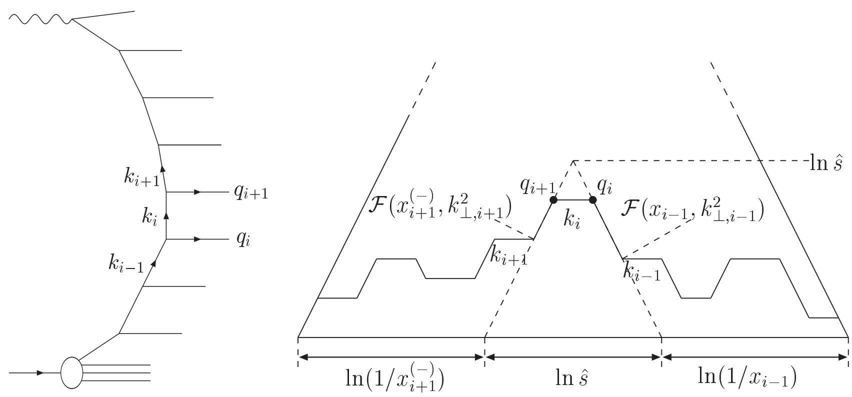

Figure 1.5: A local maximum transverse momentum, $k_{\perp,max} = k_{\perp,i}$, in a long chain, corresponds to a hard subcollision between partons with momenta k_{i-1} and $-k_{i+1}$. x_i and $x_i^{(-)}$ are defined as $x_i \equiv k_{+,i}/P_{+,tot}$ and $x_i^{(-)} \equiv -k_{-,i}/P_{-,tot}$ respectively.

A single chain may also have more than one local maximum, which corresponds to two or more correlated hard subcollisions. If we want to obtain the inclusive jet cross section, or the total $E_\perp$-flow, we have to include all produced partons q_j in the chain. To calculate this we start by studying a single link in the central part of a long chain. There are three different types of links. Besides a local maximum as in Fig. 1.5 and Fig. 1.6a, we have also the two possibilities shown in Fig. 1.6b and Fig. 1.6c. To simplify the notation we call the gluons k_a, k, and k_b as indicated in Fig. 1.6, and study the three cases:

1. $k_\perp > k_{\perp,a}, k_{\perp,b}$. Transverse momentum conservation implies that $q_{\perp,a} \approx q_{\perp,b} \approx k_\perp$, and it corresponds to a normal hard Rutherford scattering between two partons. The two colliding partons have virtualities given by $k_{\perp,a}^2$ and $k_{\perp,b}^2$, which both are small compared to the exchanged momen-

tum $k_\perp^2$. From eqs. (1.8-1.10) we see that the link is associated with the following weight factor

$$\frac{1}{k_\perp^4} \cdot \alpha_s^2(k_\perp^2), \tag{1.17}$$

which corresponds to the cross section for gluon exchange between two quasireal particles.

2. $k_{\perp,b} > k_\perp > k_{\perp,a}$, which implies that $q_{\perp,a} \approx k_\perp$ and $q_{\perp,b} \approx k_{\perp,b}$. From eq. (1.9) we see that instead of the expression in eq. (1.17), this link is associated with the following weight

$$\frac{1}{k_\perp^2 \cdot k_{\perp,b}^2} \cdot \alpha_s(k_\perp^2) \cdot \alpha_s(k_{\perp,b}^2). \tag{1.18}$$

   A similar result is obtained for $k_{\perp,a} > k_\perp > k_{\perp,b}$.

3. $k_\perp < k_{\perp,a}, k_{\perp,b}$, in which case $q_{\perp,a} \approx k_{\perp,a}$ and $q_{\perp,b} \approx k_{\perp,b}$. The corresponding weight is now given by

$$\frac{1}{k_{\perp,a}^2 \cdot k_{\perp,b}^2} \cdot \alpha_s(k_{\perp,a}^2) \cdot \alpha_s(k_{\perp,b}^2). \tag{1.19}$$

We see that when $k_\perp$ is less than $k_{\perp,a}$ or $k_{\perp,b}$, one factor $1/k_\perp^2$ is replaced by $1/k_{\perp,a}^2$ or $1/k_{\perp,b}^2$ respectively. As will be discussed more in the following, this implies that the inclusive cross section becomes non-singular for small transverse momenta. (As discussed after eq. (1.12) non-asymptotic contributions to these weights can be included most easily using the MC.)

Keeping k_a, k, and k_b fixed, we note that integrating and summing over all partons to the right of the link corresponds exactly to the non-integrated structure function $\mathcal{F}(x_a, k_{\perp,a}^2)$, where x_a is the Bjorken variable, i. e. the scaled positive lightcone momentum, $x_a = k_{+,a}/P_{+,tot}$. Similarly, integration

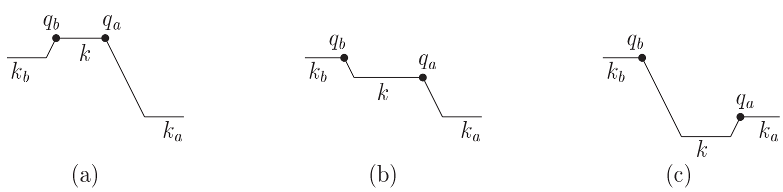

Figure 1.6: The three different possibilities for a link.

and summation of partons to the left of the link gives $\mathcal{F}(x_b, k^2_{\perp,b})$, with x_b the corresponding scaled negative lightcone momentum $x_b = x_b^{(-)} = -k_{-,b}/P_{-,tot}$.

The inclusive jet distribution can then be written in the form ($\hat{s}$ is the Mandelstam variable for the hard subcollision)

$$\begin{aligned} \frac{d\sigma_{incl}}{dq^2_\perp dy} \quad \propto \quad & \int \frac{dx_a}{x_a} \cdot \frac{dx_b}{x_b} \cdot \frac{dk^2_{\perp,a}}{k^2_{\perp,a}} \cdot \frac{dk^2_{\perp,b}}{k^2_{\perp,b}} \cdot \mathcal{F}(x_a, k^2_{\perp,a}) \cdot \mathcal{F}(x_b, k^2_{\perp,b}) \times \\ & \frac{1}{2} \cdot \frac{d\hat{\sigma}}{dq^2_\perp}(q^2_\perp, k^2_{\perp,a}, k^2_{\perp,b}, \hat{s} = x_a x_b s) \cdot \delta(y - \frac{1}{2} \ln \frac{x_a}{x_b}). \end{aligned} \tag{1.20}$$

In this formalism each produced parton is counted in two different links, one to the left and one to the right. In our notation $\frac{d\hat{\sigma}}{dq^2_\perp}$ is the inclusive cross section counting both emitted partons, and therefore a factor $\frac{1}{2}$ is needed to avoid double counting. The cross section $\frac{d\hat{\sigma}}{dq^2_\perp}$ is obtained by integrating eqs. (1.17-1.19) over $k^2_\perp$ with the constraint $k^2_\perp < \hat{s}$. In case 1 above we will then get the integral (for $k_{\perp,b} > k_{\perp,a}$)

$$\int_{k^2_{\perp,b}}^{\hat{s}} dk^2_\perp \cdot \frac{1}{k^4_\perp} \cdot 2 \cdot \delta(q^2_\perp - k^2_\perp) = \frac{2}{q^4_\perp} \cdot \theta(q^2_\perp - k^2_{\perp,b}) \cdot \theta(\hat{s} - q^2_\perp). \tag{1.21}$$

Here the factor 2 in front of the δ-function originates from the fact that we count both $q^2_{\perp,a}$ and $q^2_{\perp,b}$, each being approximately equal to $k^2_\perp$. The contributions from cases 2 and 3 can be calculated in the same way. The result obtained for a running coupling is presented in the appendix. The qualitative features can more easily be understood from the result obtained for a constant α_s, in which case we find (again for $k_{\perp,b} > k_{\perp,a}$)

$$\begin{aligned} \frac{d\hat{\sigma}}{dq^2_\perp} \quad \propto \quad & \alpha_s^2 \left\{ \frac{2}{q^4_\perp} \cdot \theta(q^2_\perp - k^2_{\perp,b}) \cdot \theta(\hat{s} - q^2_\perp) + \right. \\ & \frac{1}{q^2_\perp \cdot k^2_{\perp,b}} \cdot \theta(q^2_\perp - k^2_{\perp,a}) \cdot \theta(k^2_{\perp,b} - q^2_\perp) + \delta(q^2_\perp - k^2_{\perp,b}) \cdot \frac{1}{k^2_{\perp,b}} \cdot \ln \frac{k^2_{\perp,b}}{k^2_{\perp,a}} + \\ & \left. [\delta(q^2_\perp - k^2_{\perp,b}) + \delta(q^2_\perp - k^2_{\perp,a})] \cdot \left[\frac{1}{k^2_{\perp,b}} - \max\left(\frac{1}{\hat{s}} \, , \, \frac{Q_0^2}{k^2_{\perp,a} k^2_{\perp,b}} \right) \right] \right\} \end{aligned} \tag{1.22}$$

Here the first line corresponds to a "normal" hard subcollision, case 1 above. The second line corresponds to case 2, where one of the colliding partons has a virtuality larger than the exchanged momentum $-\hat{t} = k^2_\perp$, and the third line to case 3 where both initial partons have high virtualities. Note that if we have a soft cutoff Q_0^2, the lower limit in the $k^2_\perp$-integral for case 3 is given by $\max(\frac{k^2_{\perp,a} k^2_{\perp,b}}{\hat{s}}, Q_0^2)$.

The inclusive jet cross section is now readily obtained from inserting eq. (1.22) into eq. (1.20) and integrating with respect to $x_a, x_b, k_{\perp,a}$ and $k_{\perp,b}$. Due to the factorized form $\mathcal{F}(x,\kappa) \approx x^{-\lambda} \cdot f(\kappa)$ in eq. (1.14), with a power-like dependence on x, the result is independent of the rapidity of the pair, $y = \frac{1}{2} \ln \frac{x_a}{x_b}$, for fixed value of $x_a \cdot x_b = \hat{s}/s$. Thus the distribution corresponds to a central plateau with a height proportional to $(x_1 \cdot x_2)^{-\lambda}$, which for fixed $\hat{s}$ grows with energy proportional to s^λ.

The integration is straight forward if we assume the power-like approximation for $f(\kappa)$ in eqs. (1.14-1.15), $\mathcal{F}(x,\kappa) \approx x^{-\lambda} \cdot f(\kappa) \propto x^{-\lambda} \kappa^{\frac{\alpha_0}{\lambda}-1}$. As an example, for the term in eq. (1.21) (the first term in eq. (1.22)) the integral over x_a and x_b gives

$$\int \frac{dx_a}{x_a} \frac{dx_b}{x_b} \delta(y - \frac{1}{2} \ln \frac{x_a}{x_b}) \cdot \frac{1}{(x_a x_b)^\lambda} = \int_{q_\perp^2} \frac{d\hat{s}}{\hat{s}} \left(\frac{s}{\hat{s}}\right)^\lambda = \frac{1}{\lambda} \left(\frac{s}{q_\perp^2}\right)^\lambda \tag{1.23}$$

while the integral over $k_{\perp,a}$ and $k_{\perp,b}$ gives (including also the symmetric case $k_{\perp,a}^2 > k_{\perp,b}^2$)

$$\alpha_s^2(q_\perp^2) \int^{\ln q_\perp^2} d\kappa_b \cdot \kappa_b^{\frac{\alpha_0}{\lambda}-1} \int^{\ln q_\perp^2} d\kappa_a \cdot \kappa_a^{\frac{\alpha_0}{\lambda}-1} = \alpha_s^2(q_\perp^2) \cdot \left[\frac{\lambda}{\alpha_0} \kappa^{\frac{\alpha_0}{\lambda}}\right]^2 . \tag{1.24}$$

The full result for a running coupling, presented in the appendix, is rather lengthy and we write it in the form

$$\frac{d\sigma_{incl}^{jet}}{dq_\perp^2 dy} \propto \frac{s^\lambda}{q_\perp^{4+2\lambda}} \cdot \alpha_s^2(q_\perp^2) \cdot h(q_\perp^2). \tag{1.25}$$

The factor $s^\lambda / q_\perp^{2\lambda}$ is a consequence of the increase of $\mathcal{F} \sim x^{-\lambda}$ for small x (cf eq. (1.14)), and we have also extracted a factor $\alpha_s^2(q_\perp^2)$. Thus the function $h(q_\perp^2)$ is defined in such a way, that it would be constant in the unrealistic case, where the parton flux is given by a scaling function $F(x) \sim 1/x^\lambda$, which is independent of Q^2. The result in eq. (1.25) is proportional to s^λ, but we emphasize that this is the growth of the cross section for jet production, and not the number of jets per event.

Results

For a quantitative estimate of the jet cross section and a comparison with the "naive" approach, it would be suitable to use a Monte Carlo, which can take into account also effects from non-asymptotic energy, non-leading terms in the parton-parton cross section and contributions from quarks. However, we believe that the qualitative features can be understood from an approximate analytic calculation, provided the same approximations are used in both approaches.

Thus for $F(x,q_\perp^2)$ and $\mathcal{F}(x,k_\perp^2)$ we use the relations in eq. (1.12) and eqs. (1.14-1.15). We study purely gluonic chains and for the subcollision we use the leading expression $\frac{d\hat{\sigma}}{dq_\perp^2} \propto \frac{\alpha_s^2(q_\perp^2)}{q_\perp^4}$. For the parameters λ and Q_0 (the cut-off for small $k_\perp$) we use the values 0.3 and 0.6 GeV/c respectively, obtained from the MC fit to HERA data. Since we study purely gluonic chains, we may take $n_f = 0$, which implies that the power $\frac{\alpha_0}{\lambda} - 1$ in eq. (1.15) is close to 2. The result, presented in the appendix, can be written in terms of simple elementary functions when this power is an integer. Numerical calculations show that the result is insensitive to the exact value of the power, and that the result using $\frac{\alpha_0}{\lambda} - 1 \approx 2$ agrees well with results from the MC. For these reasons we use this value in the results below, and thus assume the following form:

$$\mathcal{F}(x,\kappa) \propto x^{-\lambda} \cdot \kappa^2 \tag{1.26}$$

which implies that the integrated structure function has the form

$$F(x,\kappa = \ln Q^2) \propto x^{-\lambda} \cdot \left[\frac{1}{3}(\kappa^3 - \kappa_0^3) + \frac{\kappa}{(\lambda+1)^2} + \frac{\kappa^2}{(\lambda+1)}\right] \tag{1.27}$$

(Note that with our convention $F(x)$ describes the density in $\ln x$, and thus corresponds to F_2. Since we have a hard interaction probe we have included the running of α_s in the final vertex, which implies an extra factor $\ln Q^2/\ln k_\perp^2$ in the last term in eq. (1.12).)

The transverse momentum dependence of the function $h(q_\perp^2)$ for a running α_s is shown by the solid line in Fig. 1.7. Also shown in this figure is the contribution from “normal hard subcollisions”, i. e. partons associated to a local maximum in the $k_\perp$ chain. We see that this contribution dominates for large $q_\perp^2$, while for smaller $q_\perp^2$, the partons which are not associated to a local maximum play a more important role, contributing more than 40% for $q_\perp^2 < 5\,\mathrm{GeV}^2$. For large $q_\perp^2$, $h(q_\perp^2)$ behaves as a power of $\ln q_\perp^2$, which corresponds to the scaling violation in the structure functions. For smaller $q_\perp^2$, $h(q_\perp^2)$ is essentially linear in $q_\perp^2$. This implies that the total transverse energy flow $dE_\perp/dy = \frac{1}{\sigma_{tot}} \cdot \int \frac{d\sigma}{dq_\perp^2 dy} dq_\perp^2 \cdot q_\perp$ is convergent for small $q_\perp$ (for $\lambda < 0.5$). Consequently the $E_\perp$ distribution is limited also without a low $q_\perp$ cutoff. In Fig. 1.7a we also show the $q_\perp$-dependence obtained from the MC (normalized to the same total flow), and, as mentioned above, we see a very nice agreement with our analytic result.

We note that although “normal hard collisions” dominate for large $q_\perp$, the other contributions correspond to approximately 25% even for $q_\perp^2 \approx 1000\,\mathrm{GeV}^2$. We expect that most of this difference would be accounted for in a calculation where hard collisions are calculated to next-to-leading order, including also $2 \to 3$ parton reactions, which thus can take into account one extra parton. This approach would, however not solve the problems encountered for small or medium $q_\perp$.

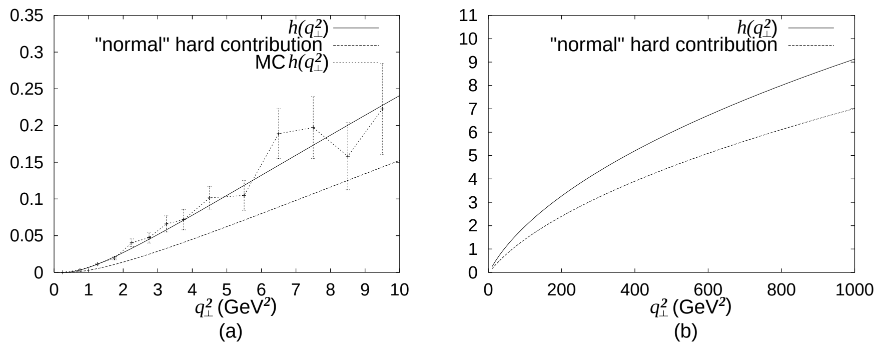

Figure 1.7: The transverse momentum distribution of $h(q_\perp^2)$ for (a) $q_\perp^2 < 10\ GeV^2$ and (b)$q_\perp^2 < 1000\ GeV^2$ according to analytical calculations (continuous curves) and MC simulation (short-dashed line).(The error bars are the estimated statistical uncertainties.) Also shown is the contribution from "normal hard subcollisions" (long-dashed line). The scale is arbitrary.

In the literature the inclusive jet cross section is often estimated from a product of two (integrated) structure functions $F(x, q_\perp^2)$ and a hard subcollision cross section $\frac{d\hat{\sigma}}{dq_\perp^2}$ for quasireal colliding partons. This estimate can be written in the form

$$\frac{d\sigma_{incl}^{jet}}{dq_\perp^2 dy} \propto \int \frac{dx_a}{x_a}\frac{dx_b}{x_b}\delta(y - \frac{1}{2}\ln\frac{x_a}{x_b}) \cdot F(x_a, q_\perp^2) \cdot F(x_b, q_\perp^2) \cdot \frac{1}{q_\perp^4} \cdot \alpha_s^2(q_\perp^2) \propto \frac{1}{q_\perp^{4+2\lambda}} \cdot \alpha_s^2(q_\perp^2) \cdot h_{naive}(q_\perp^2). \quad (1.28)$$

Here the function h_{naive} is defined analogously to the function h in eq. (1.25).

It is interesting to compare this "naive" estimate with our result in eq. (1.25). The relation between $F(x, q_\perp^2)$ and the non-integrated structure function $\mathcal{F}(x, k_\perp^2)$ is shown in eq. (1.12). There are two contributions to F, one (ordered) contribution with $q_\perp > k_\perp$, and another suppressed contribution with $q_\perp < k_\perp$. When one or both colliding partons are virtual, there is a suppression factor $q_\perp^2/k_{\perp,a}^2$ and/or $q_\perp^2/k_{\perp,b}^2$. With a cross section assumed to be proportional to $\frac{\alpha_s^2(q_\perp^2)}{q_\perp^4}$ as in eq. (1.25), we see that each link is given just the weight presented in eq. (1.17), eq. (1.18), or eq. (1.19). The difference lies in the fact that in eq. (1.28) both outgoing partons are assumed to have transverse momenta given by the momentum transfer in the collision. This underestimates the $q_\perp$ for collisions corresponding to the links in Fig. 1.6b and Fig. 1.6c. This underestimate is compensated by the fact that every link in the fan diagram corresponds to a hard collision in eq. (1.28). Thus this equation corresponds to

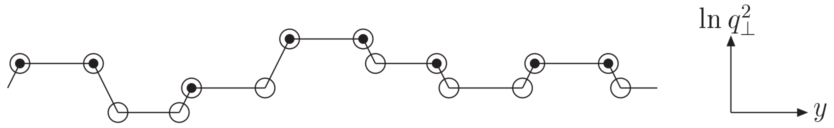

Figure 1.8: The outgoing partons according to a correct formalism (dots) and according to a naive approach (circles).

two produced partons per link instead of one. This double counting does not give a full factor of two, however, due to the underestimate of the $q_\perp$ mentioned above. The result is illustrated in Fig. 1.8. The really emitted partons in a chain are marked by a dot, while the naive expression in eq. (1.28) corresponds to a final state parton at every point marked by a circle. Thus in the naive calculation only the partons at a local maximum are given their proper weight. Those at a minimum value for $k_\perp$ should not be included at all, as no real emitted partons have these $k_\perp$-values, and those in-between are counted twice.

Fig. 1.9 shows the ratio $h(q_\perp^2)/h_{naive}(q_\perp^2)$ as a function of the transverse momentum (note the logarithmic $q_\perp$-scale). For large $q_\perp$ the Rutherford contribution dominates in both cases, making $h(q_\perp^2) \approx h_{naive}(q_\perp^2)$. For smaller $q_\perp$, on the other hand, the naive expectation gives a significant overestimate. This can also be concluded from Fig. 1.10, which shows the distribution in transverse

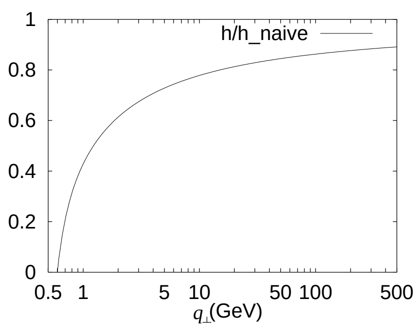

Figure 1.9: The ratio $h(q_\perp^2)/h_{naive}(q_\perp^2)$ between the cross section in our approach and the naive expectation in eq. (1.28), as a function of $q_\perp$. (Note the logarithmic scale on the x-axis.)

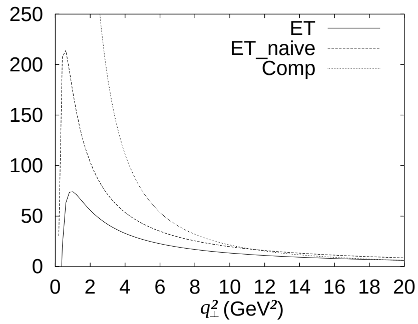

Figure 1.10: Transverse energy distribution, $dE_\perp/dydq_\perp^2$, according to our calculations (continuous curve) and the "naive" estimate in eq. (1.28) (dashed curve). For comparison we also show the result from scaling structure functions, $F(x)$ independent of $q_\perp^2$ (dotted curve). The normalization is arbitrary.

energy, $dE_\perp/dydq_\perp^2 = q_\perp \cdot dn/dydq_\perp^2$. We see that the total $E_\perp$ in the minijet region, $q_\perp \lesssim 5$ GeV, is almost a factor 2 larger in the naive estimate. It is often realized that this large contribution for very low $q_\perp$ must be unphysical, and therefore a soft cutoff, $q_{\perp,min}$, is introduced in many calculations. This cutoff is often assumed to be around 2 GeV and slowly growing with energy (see e.g. [5]). In Fig 1.11 we show the integrated transverse energy $\int^{q_\perp^2} dq_\perp^2 \frac{dE_\perp}{dydq_\perp^2}$. From

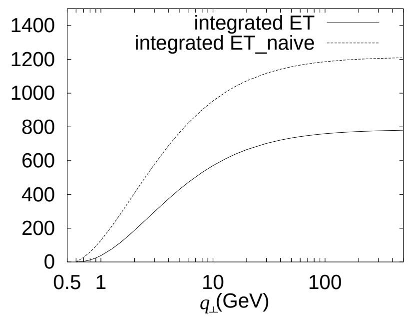

Figure 1.11: Integrated transverse energy distribution, $\int^{q_\perp^2} dq_\perp^2 dE_\perp/dydq_\perp^2$, according to our calculations (continuous curve) and the "naive" estimate in eq. (1.28) (dashed curve). The normalization is as in Fig. 1.10.

this figure we see that

$$\int_{Q_0^2}^{\infty} dq_\perp^2 \left.\frac{dE_\perp}{dy dq_\perp^2}\right|_{our\ result} \approx \int_{q^2_{\perp,min}}^{\infty} dq_\perp^2 \left.\frac{dE_\perp}{dy dq_\perp^2}\right|_{naive} \tag{1.29}$$

for $q_{\perp,min} \approx 2.1$ GeV. (Remember that the low $k_\perp$-cutoff Q_0 was given by 0.6 GeV.) This means that for asymptotic energies the total $E_\perp$ in our approach equals the naive result when $q_{\perp,min} \approx 2.1$ GeV. For smaller energies the maximal value of $q_\perp$ is limited, which implies that a somewhat smaller value of $q_{\perp,min}$ is needed. A reliable quantitative estimate would need a calculation which includes quark jets and non-leading contributions, which could be obtained with the help of the MC program. We note in particular that in our approach the corresponding effective cutoff of the naive approach, $q_{\perp,min}$, saturates for very large energies. In the conventional approach it is difficult to make predictions for higher energies without a physical understanding of the energy dependence of $q_{\perp,min}$.

Only for comparison, we have in Fig. 1.10 also included the distribution one would obtain from eq. (1.25) if the structure function F were scaling and independent of $q_\perp^2$. (The normalization is adjusted to our result for large momenta.) As is seen, this would give a very much larger (and totally unrealistic) increase for small $q_\perp$.

We end this section by noting that one chain forms a set of correlated jets. The fact that the $k_\perp$-distribution saturates for long chains (cf eq. (1.14)) implies that not only the $p_\perp$ of the jets, but also their density (the number of jets per unit rapidity) is independent of the length of the chain, i. e. independent of the energy in the collision. The jet density grows because the number of possible chains increases proportional to s^λ. It is also conceivable that the number of chains is not random, but e. g. correlated with the impact parameter, so that central collisions have more and peripheral collisions fewer chains [10]. In this paper we have only studied the average jet multiplicity, and we postpone the study of different types of correlations to future investigations.

The possible correlation between different chains may also affect the total cross section. We want to stress that the results in eq. (1.25) correspond to the cross section for jet production. To find the number of jets per event we have to divide by the total cross section, which is not directly obtained from our formulae.

1.6 Conclusions

A good understanding of jet and minijet production, and transverse energy flow, is essential for a proper interpretation of new phenomena in *pp* collisions at LHC or a possible formation of a quark-gluon plasma in nucleus collisions at

RHIC or LHC. For very high $p_\perp$ the parton flux can be described by DGLAP ($k_\perp$-ordered) evolution. The large momentum transfer between the colliding partons implies that the two evolving chains are independent of each other. For moderate and smaller $p_\perp$ (and high energies) we enter the BFKL regime and non-ordered chains become important. Here it is essential to take coherence effects and correlations into account. As we can then have several hard subcollisions in a single chain or ladder diagram, it is also important to avoid double counting.

The parton evolution in the BFKL regime can be described e. g. by the CCFM model or the semisoft formalism. The LDC model is a reformulation and generalization of the CCFM formalism, and the symmetric structure of the LDC model makes it particularly suited for a description of (mini)jet production. The result can be interpreted as the production probability for exclusive final states, which makes it convenient for treating the problem of double counting. The (mini)jet cross section is described in a $k_\perp$-factorizing form in terms of non-integrated structure functions and off-shell subcollision cross sections. The result is a dynamical suppression of small-$p_\perp$ jets, which removes the strong sensitivity to a low-$p_\perp$ cutoff in "naive" estimates based on integrated structure functions.

1.7 Acknowledgments

We want to thank Bo Andersson and Leif Lönnblad for valuable discussions, and Lönnblad for help with the Monte Carlo simulations.

References

[1] M.Ciafaloni, Nucl.Phys. **B296** (1988) 49;
S.Catani, F.Fiorani and G.Marchesini, Phys.Lett. **B234** (1990) 339; Nucl.Phys. **B336** (1990) 18.

[2] S. Catani, M. Ciafaloni and F. Hautmann, Phys.Lett. **B242**, (1990) 97;
S. Catani, M. Ciafaloni and F. Hautmann, Nucl.Phys. **B366**, (1991) 135;
J. C. Collins and R. K. Ellis, Nucl.Phys. **B360**, (1991) 3;
E. M. Levin, M. G. Ryskin, Y. M. Shabelski and A. G. Shuvaev, Sov.J.Nucl.Phys. **54**, (1991) 867.

[3] B.Andersson, G.Gustafson, J.Samuelsson, Nucl. Phys. **B467** (1996) 443.

[4] B.Andersson, G.Gustafson, H.Kharraziha, Phys.Rev. **D57** (1998) 5543.

[5] T.Sjöstrand, Lund preprint, LUTP 99-42.

[6] E.A.Kuraev, L.N.Lipatov and V.S.Fadin, Zh.Eksp.Teor.Fiz. **72** (1977) 373 [Sov.Phys.JETP **45** (1977) 199];

Ya.Ya. Balitsky and L.N.Lipatov, Yad.Fiz. **28** (1978) 1597 [Sov.J.Nucl.Phys. **28** (1978) 822].

[7] H.Kharraziha and L.Lönnblad, Lund preprint, LUTP 97-34;
H.Kharraziha and L.Lönnblad, JHEP **03** (1998) 006.

[8] H.Jung, L.Lönnblad, Proceedings of the UK Phenomenology Workshop, Durham, Sept. 1999.

[9] V.S.Fadin and L.N.Lipatov, Phys.Lett. **B429** (1998) 127;
G.Camici and M.Ciafaloni, Phys.Lett. **B430** (1998) 349.

[10] T.Sjöstrand and M.van Zijl, Phys.Rev. **D36** (1987) 2019.

1.8 Appendix

In this appendix we derive the explicit form of the function $h(q_\perp^2)$, which appears in the expression for the total cross section in eq. (1.25), for the case of a running coupling constant $\alpha_s \propto 1/\ln(k_\perp^2/\Lambda^2) \equiv 1/\kappa$. In each vertex the scale in α_s is taken to be the largest transverse momentum, which due to the consistency constraint in eq. (3.10) approximately coincides with the largest virtuality. Thus we write the cross section given by eq. (1.20) in the form

$$\frac{d\sigma_{incl}^{jet}}{dq_\perp^2 dy} \propto \frac{s^\lambda}{q_\perp^{4+2\lambda}} \cdot \alpha_s^2(q_\perp^2) \cdot h(q_\perp^2). \tag{1.30}$$

As before, we consider separately each of the three possible cases for the relative sizes of the transverse momenta of the gluons k_a, k, and k_b in Fig. 1.6:

Case 1. $k_\perp > k_{\perp,a}, k_{\perp,b}$, which implies that $q_{\perp,a} \approx q_{\perp,b} \approx k_\perp$,
Case 2. $k_{\perp,b} > k_\perp > k_{\perp,a}$, which implies that $q_{\perp,a} \approx k_\perp$ and $q_{\perp,b} \approx k_{\perp,b}$,
Case 3. $k_\perp < k_{\perp,a}, k_{\perp,b}$, which implies that $q_{\perp,a} \approx k_{\perp,a}$ and $q_{\perp,b} \approx k_{\perp,b}$.

We also assume the power-like approximation for $f(\kappa)$ in eqs. (1.14-1.15), $\mathcal{F}(x,\kappa) \approx x^{-\lambda} \cdot f(\kappa) \propto x^{-\lambda}\kappa^{\frac{\alpha_0}{\lambda}-1} \approx x^{-\lambda} \cdot \kappa^2$, where $\frac{\alpha_0}{\lambda} - 1$ is approximately equal to 2.

We start by considering the contribution from case 1. Here the scale in α_s is given just by $k_\perp^2 \approx q_\perp^2$. Thus the only modification to eq. (1.21) is a factor $\alpha_s^2(q_\perp^2) \propto 1/\ln^2(q_\perp^2)$, which is factored out explicitly in the definition of $h(q_\perp^2)$ in eq. (1.30). Thus we find

$$\left.\frac{d\hat\sigma}{dq_\perp^2}\right|_{contr\ 1} \propto 2 \cdot \frac{1}{q_\perp^4} \cdot \frac{1}{\ln^2(q_\perp^2)}. \tag{1.31}$$

We have a factor 2 in the inclusive cross section, because we count both outgoing partons. When this expression is inserted into eq. (1.20), the integrations with respect to $k_{\perp,a}$ and $k_{\perp,b}$ give

$$\frac{1}{2}\int_{\kappa_0}^{l_q} d\kappa_b \int_{\kappa_0}^{l_q} d\kappa_a \cdot \frac{2}{q_\perp^4} \cdot \frac{1}{l_q^2} \cdot \kappa_a^2 \cdot \kappa_b^2 = \frac{1}{q_\perp^4} \cdot \frac{1}{l_q^2} \cdot \frac{1}{9} \cdot (l_q^3 - \kappa_0^3)^2 \tag{1.32}$$

where $l_q \equiv \ln q_\perp^2$ and $\kappa_0 \equiv \ln Q_0^2$. Here the factor $1/2$ compensates for double counting as described in the main text. The remaining integrations with respect to x_a and x_b (cf eq. (1.23)) give finally:

$$\left.\frac{d\sigma}{dq_\perp^2 dy}\right|_{contr\ 1} \propto \frac{s^\lambda}{q_\perp^{4+2\lambda}} \cdot \frac{1}{l_q^2} \cdot \frac{1}{\lambda} \cdot \frac{1}{9} \cdot (l_q^3 - \kappa_0^3)^2. \tag{1.33}$$

For case 2, the subcollision cross section $\frac{d\hat{\sigma}}{dq_\perp^2}$ is given by

$$\begin{aligned}\left.\frac{d\hat{\sigma}}{dq_\perp^2}\right|_{contr\ 2} \propto\ & \int_{k_{\perp,a}^2}^{k_{\perp,b}^2} dk_\perp^2 \cdot [\delta(q_\perp^2 - k_{\perp,b}^2) + \delta(q_\perp^2 - k_\perp^2)] \cdot \frac{1}{k_{\perp,b}^2} \cdot \frac{1}{k_\perp^2} \cdot \frac{1}{\kappa_b} \cdot \frac{1}{\kappa} = \\ & \frac{1}{k_{\perp,b}^2} \cdot \frac{1}{\kappa_b} \cdot \Bigg[\delta(q_\perp^2 - k_{\perp,b}^2) \ln(\frac{\kappa_b}{\kappa_a}) + \theta(k_{\perp,b}^2 - q_\perp^2) \times \\ & \theta(q_\perp^2 - k_{\perp,a}^2) \cdot \frac{1}{q_\perp^2} \cdot \frac{1}{l_q}\Bigg]\end{aligned} \tag{1.34}$$

After insertion into eq. (1.20), calculations analogous to the ones in case 1 give the following result for the contribution to the total cross section:

$$\begin{aligned}\left.\frac{d\sigma}{dq_\perp^2 dy}\right|_{contr\ 2} \propto\ & \frac{s^\lambda}{q_\perp^{4+2\lambda}} \cdot \frac{1}{l_q^2} \cdot \frac{1}{3} \cdot \left\{\frac{1}{\lambda}\left[\frac{l_q^6}{3} - \frac{\kappa_0^3 l_q^3}{3} - \kappa_0^3 l_q^3 \cdot ln\left(\frac{l_q}{\kappa_0}\right)\right] + \right. \\ & \left. l_q \cdot (l_q^3 - \kappa_0^3) \cdot \left[\frac{1 + l_q}{\lambda(\lambda+1)} - \frac{1}{(\lambda+1)^2}\right]\right\}\end{aligned} \tag{1.35}$$

In case 3 the appropriate expression for the subcollision cross section $\frac{d\hat{\sigma}}{dq_\perp^2}$ is

$$\begin{aligned}\left.\frac{d\hat{\sigma}}{dq_\perp^2}\right|_{case\ 3} \propto\ & \int^{k_{\perp,a}^2} dk_\perp^2 \cdot [\delta(q_\perp^2 - k_{\perp,a}^2) + \delta(q_\perp^2 - k_{\perp,b}^2)] \times \\ & \frac{1}{k_{\perp,b}^2} \cdot \frac{1}{k_{\perp,a}^2} \cdot \frac{1}{\kappa_b} \cdot \frac{1}{\kappa_a},\end{aligned} \tag{1.36}$$

where the lower integration limit is given by $\max(\frac{k_{\perp,a}^2 k_{\perp,b}^2}{\hat{s}}, Q_0^2)$. Inserting this into eq. (1.20) and performing the integrations we obtain

$$\left.\frac{d\sigma}{dq_\perp^2 dy}\right|_{contr\ 3} \propto \frac{s^\lambda}{q_\perp^{4+2\lambda}} \cdot \left[\frac{1}{\lambda(\lambda+1)} \cdot l_q \cdot \left(\frac{l_q^2-\kappa_0^2}{2} + l_q - \kappa_0\right) - \frac{1}{(\lambda+1)^2} \cdot l_q \cdot (l_q - \kappa_0)\right]. \tag{1.37}$$

Adding the three contributions, and including the symmetric situation $k_{\perp,a} > k_{\perp,b}$ to case 2, we find finally for the function $h(q_\perp^2)$ in eq. (1.30)

$$\begin{aligned} h(q_\perp^2) \propto & \left\{\frac{1}{\lambda} \cdot \frac{1}{9} \cdot (l_q^3 - \kappa_0^3)^2\right\} + \left\{\frac{1}{\lambda} \cdot \frac{1}{3} \cdot \left[\frac{l_q^6}{3} - \frac{\kappa_0^3 l_q^3}{3} - \kappa_0^3 l_q^3 \cdot ln\left(\frac{l_q}{\kappa_0}\right)\right] + \right. \\ & \left. \frac{1}{3} \cdot l_q \cdot (l_q^3 - \kappa_0^3) \cdot \left[\frac{1+l_q}{\lambda(\lambda+1)} - \frac{1}{(\lambda+1)^2}\right]\right\} + \\ & \left\{\frac{1}{\lambda(\lambda+1)} \cdot l_q^3 \cdot (\frac{l_q^2}{2} - \frac{\kappa_0^2}{2} + l_q - \kappa_0) - \right. \\ & \left. \frac{1}{(\lambda+1)^2} \cdot l_q^3 \cdot (l_q - \kappa_0)\right\}. \end{aligned} \tag{1.38}$$

This can be compared with the "naive" expression obtained from eq. (1.27). With the same normalization we get

$$h_{naive} \propto \frac{2}{\lambda}\left[\frac{1}{3}(l_q^3 - \kappa_0^3) + \frac{l_q}{(\lambda+1)^2} + \frac{l_q^2}{(\lambda+1)}\right]^2, \tag{1.39}$$

where the factor 2 in the inclusive cross section follows because each hard subcollision produces two jets. We see that the leading term for large $q_\perp$, $\frac{2}{9\lambda}(\ln q_\perp^2)^6$, is the same in both cases, but h_{naive} is significantly larger for smaller $q_\perp$-values.

A Simple Model for the BFKL-DGLAP Transition in DIS

Paper II

A Simple Model for the BFKL-DGLAP Transition in Deep Inelastic Scattering

Gösta Gustafson and Gabriela Miu

Department of Theoretical Physics
Lund University, Sölvegatan 14A, S-223 62 Lund, Sweden

European Physical Journal **C23**, 267 – 274 (2002)

Abstract

A simple model is presented, which interpolates between the DGLAP and BFKL regimes in deep inelastic *ep* scattering. The model is based on the CCFM and LDC models, and it is simple enough to provide an intuitive picture of the transition region between the two domains. Results are presented for both fixed and running coupling; for fixed coupling the transition between the domains occurs at a constant ratio between $\ln k_{\perp}^2$ and $\ln 1/x$, while for a running coupling it occurs for constant ratio between $\ln \ln k_{\perp}^2$ and $\ln 1/x$.

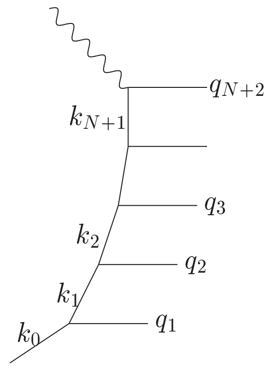

Figure 2.1: *A fan diagram.*

2.1 Introduction

When $k_\perp$ is large and $1/x$ is limited we are in the DGLAP regime, and when $1/x$ is large and $k_\perp$ is limited we are in the BFKL regime. An essential question is then: What is large? Where is the boundary between the regimes, and what is the behaviour in the transition region? We will here present a simple interpolating model, which can illuminate these questions. The model is based on the CCFM [1] and LDC [2] models, and is simple enough to provide an intuitive picture of the dynamical mechanisms.

The model is relevant for small x, and has a smooth transition between large $k_\perp$, where ordered chains dominate, and small $k_\perp$, where non-ordered chains are most important. We will first study only leading terms in $\ln 1/x$, and for large $k_\perp$ the result therefore corresponds to the double log approximation and not really to the DGLAP regime. Some non-leading effects in $\ln 1/x$ will be discussed in a subsequent section.

For large $k_\perp$ the non-integrated structure function $\mathcal{F}(x, k_\perp^2)$ is dominated by contributions from ordered chains which satisfy [3] (for notation see Fig 2.1)

$$\begin{aligned} x &\equiv x_{N+1} < x_N < \dots\ x_1 < 1 \\ k_\perp^2 &\equiv k_{\perp N+1}^2 > k_{\perp N}^2 > \dots\ k_{\perp 1}^2 > Q_0^2. \end{aligned} \tag{2.1}$$

In the simpler case with a fixed coupling α_s, and including only the $1/z$ pole in the splitting function, the contribution from each chain is a product of factors

$\frac{3\alpha_s}{\pi} \cdot \frac{dx_i}{x_i} \cdot \frac{dk_{\perp,i}^2}{k_{\perp,i}^2}$. This implies

$$\begin{aligned}
\mathcal{F}(x,k_\perp^2) \quad &\sim \quad \bar{\alpha}\sum_N \int \prod^N \bar{\alpha}\frac{dx_i}{x_i}\frac{dk_{\perp,i}^2}{k_{\perp,i}^2}\theta(x_{i-1}-x_i)\theta(k_{\perp,i}^2-k_{\perp,i-1}^2) = \\
&\quad\ \bar{\alpha}\sum_N \int \prod^N \bar{\alpha}\ dl_i\theta(l_i-l_{i-1})\ d\kappa_i\theta(\kappa_i-\kappa_{i-1}) \\
\text{where}\ \ \bar{\alpha} \equiv \frac{3\alpha_s}{\pi},&\quad l \equiv \ln(1/x) \ \ \text{and}\ \ \kappa \equiv ln(k_\perp^2/\Lambda_{QCD}^2).
\end{aligned} \tag{2.2}$$

Integration over κ_i with the θ-functions gives the phase space for N ordered values κ_i. The result is $\kappa^N/N!$. (If there is a soft cutoff $k_{\perp cut}$ we obtain more exactly $(\kappa-\kappa_{cut})^N/N!$. For a fixed coupling we could use $k_{\perp cut}$ as the scale in the definition of κ, but this would be less convenient for a running coupling.) The integrations over l_i give a similar result, and defining the rescaled structure function $G = 1/\bar{\alpha}\cdot\mathcal{F}$, we obtain the well-known DLLA result

$$G(x,k_\perp^2) \equiv \frac{1}{\bar{\alpha}}\mathcal{F}(x,k_\perp^2) \sim \sum_N \bar{\alpha}^N \cdot \frac{l^N}{N!}\cdot\frac{\kappa^N}{N!} = I_0(2\sqrt{\bar{\alpha}l\kappa}) \tag{2.3}$$

where I_0 is a modified Bessel function.

In the BFKL region non-ordered chains contribute, and the result is a power-like increase for small x-values [4],

$$\mathcal{F} \sim \frac{1}{x^\lambda}f(\kappa,l) \tag{2.4}$$

where the function $f(\kappa,l)$ describes a random walk in κ [4, 5].

In the interpolation region we must calculate suppressed contributions from non-ordered chains. It is then necessary to specify the separation between initial state radiation and final state radiation, which is not given by Nature, but has to be defined by the calculation scheme. This separation should have the property that final state emissions do not affect the total cross section, i. e. the structure function, and their effect on the final state can be described by Sudakov form factors. A particular scheme was chosen by Ciafaloni, Catani, Fiorani, and Marchesini (the CCFM model) [1]. Here the initial state radiation is ordered in *angle* (or rapidity) and *energy* (or $q_+ = q_0 + q_L$). The contribution from a particular chain is then given by the expression

$$\prod \bar{\alpha}\frac{dz_i}{z_i}\frac{dq_{\perp,i}^2}{q_{\perp,i}^2}\Delta_{ne}(z_i,k_{\perp,i},q_{\perp,i}) \tag{2.5}$$

where Δ_{ne} is a noneikonal form factor and $z_i = x_i/x_{i-1}$.

The Linked Dipole Chain (LDC) model [2] is a reformulation and generalization of the CCFM result in a scheme, where more gluons are treated as final state radiation. The initial chain is ordered in $q_+ = q_0 + q_L$ *and* $q_- = q_0 - q_L$, and $q_\perp$ satisfies $q_\perp > \min(k_{\perp,i}, k_{\perp,i-1})$. This implies that there are fewer chains; one LDC chain corresponds to a set of CCFM chains. It then turns out that all the corresponding noneikonal form factors add up to just unity, and thus the contribution from each such chain is given by the simple product

$$\prod \bar{\alpha} \frac{\mathrm{d}z_i}{z_i} \frac{\mathrm{d}q^2_{\perp,i}}{q^2_{\perp,i}}. \tag{2.6}$$

We note in particular that this expression is totally left-right symmetric, meaning that we get the same result if we start the chain in the photon end, instead of in the proton end. (This implies that the formalism automatically takes into account contributions from "resolved photons".)

We can express this result in the link momenta k_i, instead of the final state momenta q_i. For ordered chains we have $q_{\perp,i} \approx k_{\perp,i}$, and thus for these chains the expression in eq. (2.6) agrees with eq. (2.2), but for non-ordered chains this is no longer the case. Using the relations $\mathrm{d}^2 q_{\perp,i} = \mathrm{d}^2 k_{\perp,i}$ and $q^2_{\perp,i} \approx \max(k^2_{\perp,i}, k^2_{\perp,i-1})$ we find the following weights

$$\begin{aligned} \frac{\mathrm{d}^2 q_{\perp,i}}{q^2_{\perp,i}} &\approx \frac{\mathrm{d}^2 k_{\perp,i}}{k^2_{\perp,i}} \quad \text{for} \quad k_{\perp,i} > k_{\perp,i-1} \text{ and} \\ \frac{\mathrm{d}^2 q_{\perp,i}}{q^2_{\perp,i}} &\approx \frac{\mathrm{d}^2 k_{\perp,i}}{k^2_{\perp,i}} \cdot \frac{k^2_{\perp,i}}{k^2_{\perp,i-1}} \quad \text{for} \quad k_{\perp,i} < k_{\perp,i-1}. \end{aligned} \tag{2.7}$$

Thus, for a step down in $k_\perp$ we have an extra suppression factor $k^2_{\perp,i}/k^2_{\perp,i-1}$, which reduces the weight for non-ordered chains. (This suppression also implies that if the chain goes up to $k_{\perp,max}$ and then down to $k_{\perp,final}$ we obtain a factor $1/k^4_{\perp,max}$, which corresponds to the cross section for a hard parton-parton subcollision.)

In the following we will first discuss a model for a fixed coupling, and after that the more relevant situation with a running α_s. In section 4 we discuss some effects of non-leading terms in $\ln 1/x$. We end by some comments on the Laplace transforms in section 5.

2.2 Fixed coupling

As discussed in the introduction, in the LDC and CCFM models downward steps in $k_\perp$ are suppressed by the factor $k^2_{\perp,i}/k^2_{\perp,i-1}$ in eq. (2.7). Expressed in the logarithmic variable κ, large downward steps are thus suppressed by an exponential factor $\exp(\kappa_i - \kappa_{i-1})$. This implies that the effective allowed distance, δ, for a downward step is given by the average value of this exponential, which means

$$\delta \sim \int_{\kappa_i} (\kappa_{i-1} - \kappa_i) e^{-(\kappa_{i-1}-\kappa_i)} \mathrm{d}\kappa_{i-1} = 1. \tag{2.8}$$

This increases the phase space; the boundary is effectively given by $\kappa_i > \kappa_{i-1} - \delta$ instead of the strict ordering $\kappa_i > \kappa_{i-1}$ in eq. (2.2) relevant in the DGLAP limit. (This has similarities with the van der Waals gas formula, where the gas molecules take up a fixed volume. Here the corresponding "volume" is negative, which thus increases the phase space.) The result is that the phase space factor $\frac{\kappa^N}{N!}$ is replaced by $\frac{(\kappa+N\delta)^N}{N!}$ [1]. Thus we obtain

$$G(x, k_\perp^2) \sim \sum_N \frac{(\bar{\alpha}l)^N}{N!} \frac{(\kappa + N\delta)^N}{N!}. \tag{2.9}$$

When κ *is very large* we can neglect the term $N\delta$, and thus obtain the DGLAP result from eq. (2.3):

$$G(x, k_\perp^2) \sim \sum_N \frac{(\bar{\alpha}l\kappa)^N}{(N!)^2} = I_0(2\sqrt{\bar{\alpha}l\kappa}) \approx \frac{\exp(2\sqrt{\bar{\alpha}l\kappa})}{\sqrt{4\pi\sqrt{\bar{\alpha}l\kappa}}}. \tag{2.10}$$

The last approximation is relevant when the argument of I_0 is large compared to 1.

When κ *is small*, it can instead be neglected compared to $N\delta$, and we obtain using Sterling's formula

$$\begin{aligned} G &\sim \sum_N \frac{(\bar{\alpha}l)^N}{N!} \frac{(N\delta)^N}{N!} \approx \sum_N \frac{(\bar{\alpha}l)^N}{N!} \delta^N \frac{e^N}{\sqrt{2\pi N}} \approx \\ & \frac{\exp(\bar{\alpha}\delta e l)}{\sqrt{2\pi\bar{\alpha}\delta e l}} = \frac{1}{\sqrt{2\pi\lambda \ln 1/x}} \cdot \frac{1}{x^\lambda} \\ \text{with } \lambda &= e\delta\bar{\alpha}. \end{aligned} \tag{2.11}$$

Thus for $\delta = 1$ we get $\lambda = e\bar{\alpha} = 2.72\bar{\alpha}$. This should be compared with the leading order result for the BFKL equation, $\lambda = 4\ln 2\,\bar{\alpha} = 2.77\bar{\alpha}$.

We now also want to study the behaviour of the sum in eq (2.9) in the *transition region* between the two extreme situations. This can be estimated by the saddle point method. Using Sterling's formula we get from eq. (2.9)

$$G \sim \sum_N \exp\left\{N[\ln(\bar{\alpha}l) + \ln(\kappa + N\delta) - 2\ln N + 2]\right\} \equiv \sum_N \exp\{h(N)\}. \tag{2.12}$$

[1] This result is exactly correct only if the non-ordered variables κ_i are allowed to take on negative values in the middle of the chain. If all κ_i are restricted to be positive, we get instead $(\kappa+\delta)[\kappa+(N+1)\delta]^{N-1}/N!$. This small difference does not modify our conclusions.

In this sum the terms with N-values around N_{max} dominate, where N_{max} is the solution to the equation

$$h'(N_{max}) = \ln(\bar{\alpha}l) + \ln(\kappa + N_{max}\delta) - 2\ln N_{max} + \frac{N_{max}\delta}{\kappa + N_{max}\delta} = 0. \quad (2.13)$$

Let us first assume that $k_\perp$ is large and satisfies the inequality $N_{max}\delta < \kappa$. This implies that for the dominating terms in the sum we have $\kappa + N\delta \approx \kappa$, which corresponds to the "DGLAP region" as discussed above. Inserted into eq. (2.13) this implies $N_{max} \approx \sqrt{\bar{\alpha}l\kappa} + \bar{\alpha}l\delta$. For consistency with our assumption, we must then demand this expression to be smaller than κ/δ, which implies $\kappa > \bar{\alpha}\frac{3+\sqrt{5}}{2}\delta^2 l$. For $\delta = 1$ we thus obtain

$$\kappa > \frac{3+\sqrt{5}}{2}\,\bar{\alpha}\,l \approx 2.62\,\bar{\alpha}\,l. \quad (2.14)$$

Next we assume that $N_{max}\delta > \kappa$. This implies that for the dominating terms in the sum we have $\kappa + N\delta \approx N\delta$, which corresponds to the BFKL region. Eq. (2.13) now gives $N_{max} \approx \bar{\alpha}\,l\,\delta\,e$. Consistency with the assumption, $N_{max} > \kappa/\delta$, now demands $\kappa < \bar{\alpha}\,e\,\delta^2 l$. For $\delta = 1$ we therefore obtain in this case

$$\kappa < \bar{\alpha}\,e\,l \approx 2.72\,\bar{\alpha}\,l. \quad (2.15)$$

This is very close to the limit in eq. (2.14). Consequently this line in the (l, κ) plane corresponds to the transition between the BFKL and DGLAP regions. Due to the result for the exponent λ in eq. (2.11) this line can be written $\kappa/l \approx \lambda$.

For small x we can also go one step further, and expand eq. (2.13) in powers of κ/l. This gives $N_{max} \approx e\delta\bar{\alpha}l + \kappa^2/(2e\delta^3\bar{\alpha}l) - 1$, which implies (with λ still given by $e\delta\bar{\alpha}$)

$$G \sim \frac{1}{\sqrt{2\pi\lambda l}} \exp\left[\lambda l + \frac{\kappa}{\delta} - \frac{\kappa^2}{2\delta^2\lambda l}\right]. \quad (2.16)$$

We recognize here the Gaussian distribution with a width proportional to λl, corresponding to a random walk in κ. This can be compared with the result of the BFKL equation [5]:

$$G \sim \frac{1}{\sqrt{2\pi\lambda l}} \exp\left[\lambda l + \frac{\kappa}{2} - \frac{\kappa^2}{\Delta\lambda l}\right]; \quad \Delta = \frac{14\zeta(3)}{\ln 2} \approx 24.3. \quad (2.17)$$

We see that for $\delta \approx 1$ the distribution in eq. (2.16) is significantly more narrow. This is perhaps not surprising as the exponential suppression for large values of $\kappa_{i-1} - \kappa_i$ in eq. (2.8) is replaced by the sharp cut for $\kappa_i = \kappa_{i-1} - \delta$. The model is, however, only intended to illustrate the qualitative features and not to give a quantitative description.

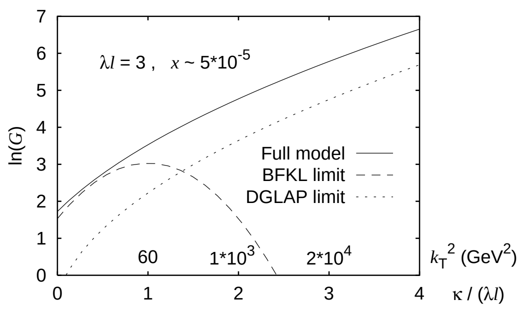

Figure 2.2: *The logarithm of the rescaled structure function obtained for a fixed coupling, for $\lambda l = 3$, which corresponds to $x \sim 5 \cdot 10^{-5}$. The approximations for small and large $k_\perp$-values are indicated by the dashed and doted lines respectively. The horizontal axis is the combination $\kappa/\lambda l$, chosen so that the transition occurs when this variable has values around 1. Corresponding values of $k_\perp^2$ in GeV^2 are also indicated.*

The result of a numerical evaluation of eq. (2.9) is presented in Fig. 2.2 together with the DGLAP and BFKL approximations of eqs. (2.10) and (2.16). We have here chosen $\delta = 1$. The result depends only on the two combinations λl and $\kappa/\lambda l$, where the last combination is chosen so that the transition occurs when this variable is around 1. We see in this figure how our result interpolates between the BFKL and DGLAP expressions, although the normalization of the DGLAP approximation is off by roughly a factor e, even for large values of $k_\perp$. An essential feature is also that G grows monotonically with κ. The Gaussian behaviour is only obtained in an expansion of $\ln \mathcal{F}$ to second order in powers of κ/l.

Conclusion:

The expression $\mathcal{F}(x, k_\perp^2) \sim \bar{\alpha} \sum_N \frac{(\bar{\alpha} l)^N}{N!} \frac{(\kappa + N\delta)^N}{N!}$ with $\delta \approx 1$ reproduces DGLAP evolution (or more correctly the double log approximation $\sim \exp(2\sqrt{\bar{\alpha} l \kappa})$) for large values of κ/l, and reproduces BFKL evolution $\sim x^{-\lambda}$ with $\lambda \approx e\bar{\alpha}$ for smaller κ/l. The transition occurs for a fixed ratio between κ and l:

$$\frac{\kappa}{l} = \frac{\ln k_\perp^2}{\ln 1/x} \approx \lambda \approx e\,\bar{\alpha}. \tag{2.18}$$

We also note that the structure function grows monotonically with increasing $\ln k_\perp^2$, in contrast to the Gaussian distribution in the BFKL approximation, related to a random walk in $\ln k_\perp^2$. The Gaussian distribution is only obtained in a second order expansion in κ/l.

2.3 Running Coupling

For a running coupling we use the notation

$$\begin{aligned}
\bar{\alpha} &= \frac{3\alpha_s}{\pi} \equiv \frac{\alpha_0}{\kappa} \\
u &\equiv \ln(\kappa/\kappa_{cut}) = \ln\ln(k_\perp^2/\Lambda^2) - \ln\ln(k_{\perp cut}^2/\Lambda^2) \\
G &\equiv \frac{\kappa}{\alpha_0} \cdot \mathcal{F}.
\end{aligned} \tag{2.19}$$

As we only include purely gluonic chains, it would be most consistent to use the value for α_s obtained for no flavours, which corresponds to $\alpha_0 = 12/11 \approx 1$. In eq. (2.6) the scale in α_s at a certain vertex should be given by the largest of the associated virtualities, which means $\max(k_{\perp,i}^2, k_{\perp,i-1}^2)$. For a step up this is $k_{\perp,i}^2$, and thus the running coupling contains a factor $1/\kappa_i$. For these steps we also have $q_\perp \approx k_\perp$, and thus the weight in eq. (2.6) becomes

$$\prod \frac{\alpha_0}{\kappa_i} \mathrm{d}l_i \mathrm{d}\kappa_i = \prod \alpha_0 \mathrm{d}l_i \mathrm{d}u_i. \tag{2.20}$$

In the DGLAP region u is large, and downward steps can be neglected. In analogy with eqs. (2.3) and (2.10) we then find the well-known result

$$G \sim \sum \alpha_0^N \frac{l^N}{N!} \cdot \frac{u^N}{N!} = I_0(2\sqrt{\alpha_0 l u}), \tag{2.21}$$

which resembles eq. (2.10) for fixed coupling, only with $\ln k_\perp^2$ replaced by $\ln\ln k_\perp^2$.

Including downward steps we see, however, that the effect of the suppression factor $k_{\perp,i}^2/k_{\perp,i-1}^2$ becomes quite different for a running coupling compared to the case with a fixed coupling. Expressed in the variables u_i, this factor is

$$\exp[-(e^{u_{i-1}} - e^{u_i})] \sim \exp[-e^{u_{i-1}}(u_{i-1} - u_i)]. \tag{2.22}$$

When u_i and u_{i-1} are large, this factor drops rapidly with increasing difference $u_{i-1} - u_i$. This implies that it is easy to go down when u_i and u_{i-1} are small, but very difficult when they are large. A consequence of this feature is the result observed in ref. [6], that a typical chain contains two parts. In the first part the $k_\perp$-values are relatively small, and it is therefore easy to go up and down in u (or $k_\perp$), and non-ordered $k_\perp$-values are important. The second part is an ordered, DGLAP-type, chain, where $k_\perp$ increases towards its final value.

In ref. [7] we also found that for large l (small x) an approximate solution to the LDC equation has the factorized form

$$G \sim \frac{1}{x^\lambda} \cdot \kappa^{\frac{\alpha_0}{\lambda}}. \tag{2.23}$$

Let us study a chain with N links, out of which $N-k$ correspond to the first part with small non-ordered $k_\perp$, and the remaining k links belong to the second part with increasing $k_\perp$. Assume that the effective space for each u_i in the soft part is given by a quantity Δ, and we will below estimate its magnitude. The total weight for this part then becomes Δ^{N-k}. For the k links in the second, ordered, part the phase space becomes as before $u^k/k!$. Thus the total result is

$$G \sim \sum_N \frac{(\alpha_0 l)^N}{N!} \sum_{k=0}^{N} \frac{u^k}{k!} \Delta^{N-k} = \sum_N \frac{(\alpha_0 l \Delta)^N}{N!} \sum_{k=0}^{N} \frac{(u/\Delta)^k}{k!}. \tag{2.24}$$

We first study the behaviour of this expression in the two extreme situations with small and large $k_\perp$-values.

i) BFKL limit, u small.

Assume first that u/Δ is small compared to dominating values of N. Then the sum over k gives approximately $\exp(u/\Delta)$. Thus G takes the form

$$G \sim \sum_N \frac{(\alpha_0 l \Delta)^N}{N!} \exp(u/\Delta) = \exp(\alpha_0 l \Delta + u/\Delta) = \frac{1}{x^\lambda} \cdot \kappa^{\alpha_0/\lambda} \tag{2.25}$$

$$\text{where} \quad \lambda = \alpha_0 \Delta. \tag{2.26}$$

We note that this result has just the factorized form of eq. (2.23), which was obtained in ref. [7]. From eq. (2.25) we see that our assumptions imply that the sum over N is dominated by N-values around $\alpha_0 l \Delta$. For consistency we therefore demand $u/\Delta < \alpha_0 l \Delta$ or

$$u < \alpha_0 l \Delta^2 = \frac{\lambda^2 l}{\alpha_0}. \tag{2.27}$$

ii) DGLAP limit, u large.

We now assume that u is so large that u/Δ is larger than N for the most important values of N. The sum over k is then dominated by its last term, $\frac{(u/\Delta)^N}{N!}$, which gives the result in eq. (2.21):

$$G \sim \sum_N \frac{(\alpha_0 l u)^N}{(N!)^2} = I_0(2\sqrt{\alpha_0 l u}). \tag{2.28}$$

Using Sterling's formula we find that in this case the sum is dominated by N-values around $N_{max} = \sqrt{\alpha_0 lu}$. For consistency we therefore now demand

$$u/\Delta > \sqrt{\alpha_0 lu} \;\text{ or }\; u > \alpha_0 l \Delta^2 = \frac{\lambda^2 l}{\alpha_0}. \tag{2.29}$$

We see that this limit coincides exactly with the BFKL limit in eq. (2.27). Thus the regions of validity for the BFKL and DGLAP approximations of eqs. (2.25) and (2.28) respectively join at the common boundary for the fixed ratio between u and l:

$$u/l \approx \lambda^2/\alpha_0. \tag{2.30}$$

These results are confirmed by a numerical evaluation of eq. (2.24) presented in Fig. 2.3. Introducing the variables $v = \lambda l$ and $w = \frac{\alpha_0 u}{\lambda^2 l}$ we have

$$\begin{aligned} \ln G &\sim v(1+w)\,; & w < 1\ (BFKL) \\ \ln G &\sim \ln I_0(2v\sqrt{w}) \approx 2v\sqrt{w} - \tfrac{1}{2}\ln(4\pi v\sqrt{w})\,; & w > 1\ (DGLAP) \end{aligned} \tag{2.31}$$

The variables v and w are chosen so that the transition occurs around $w = 1$. Note that the asymptotic approximation for the Bessel function, $I_0(z) \approx \exp(z)/\sqrt{2\pi z}$, is relevant in all of the interesting kinematic region. The model should be applied to small x. For $x < 0.03$ and $\lambda \sim 0.3$ we have $\lambda l > 1$, which together with the constraint in eq. (2.29) implies that $\alpha_0 lu > 1$. Thus the argument in the Bessel function is here always larger than 2, and for these values the error in the approximation is less than 10%.

It is also interesting to rewrite eq. (2.24) in the following form, where $m = N - k$:

$$G \sim \sum_m (\alpha_0 l \Delta)^m \sum_{N=m}^{\infty} \frac{(\alpha_0 lu)^{N-m}}{N!(N-m)!} = \sum_m \left(\frac{\alpha_0 l \Delta^2}{u}\right)^{\frac{m}{2}} I_m(2\sqrt{\alpha_0 lu}). \tag{2.32}$$

Here m is the number of steps in the initial non-ordered part, and I_m are modified Bessel functions. The DGLAP approximation in eq. (2.28) corresponds to just the first term with $m = 0$, and Fig. 2.3b shows how this series approaches the full result when more terms are included.

Estimate of the effective phase space Δ

We now want to study in more detail the initial part of the chain, where $k_\perp$ is small, α_s large and where it therefore is easy to go up and down in $k_\perp$. If α_s is assumed to be proportional to $1/\kappa$, the result is sensitive to the infrared region, and thus depends on the effective cutoff for small $k_\perp$ [7, 5]. Experience from the LDC MC shows that long chains often have the form illustrated in Fig. 2.4, with alternating steps up and down in $k_\perp$. Occasionally there are also

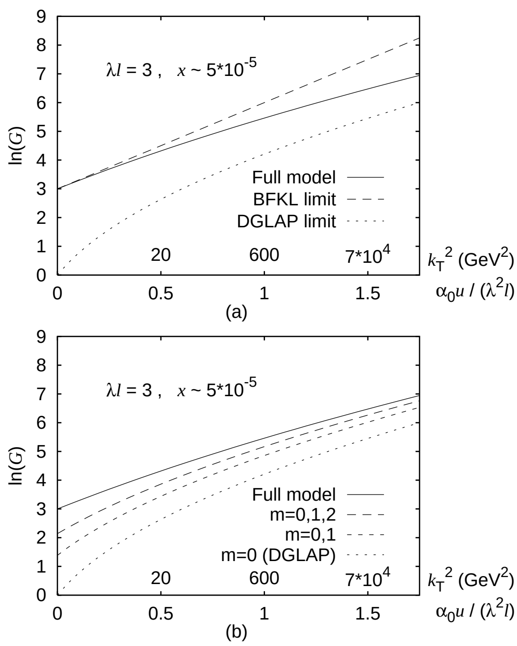

Figure 2.3: *(a) The logarithm of the rescaled structure function for a running coupling. $\lambda l = 3$, which corresponds to $x \sim 5 \cdot 10^{-5}$. The approximations for small and large $k_\perp$-values are indicated by the dashed and doted lines respectively. The horizontal axis is the combination $\alpha_0 u/(\lambda^2 l)$, chosen so that the transition occurs when this variable has values around 1. Corresponding values of $k_\perp^2$ in GeV^2 are also indicated. (b) The contributions from the first three terms in eq. (2.32). Note that $m = 0$ corresponds to the DGLAP limit.*

two steps in the same direction (e. g. the step κ_4 in Fig. 2.4). Neglecting such "stairs" will underestimate the power λ but, as we will see, qualitatively it does reproduce the dependence of λ on the cutoff.

Let us study two typical steps, a step up to a high level κ_1, followed by a step down to a low level κ_2 (cf. Fig. 2.4). (For simplicity we use the indices 1 and 2, even if these steps are not in the beginning of the chain.) The definition of Δ implies that the κ-integrations in these two steps (including the factors $\bar{\alpha}(\kappa)$) should correspond to a factor $(\alpha_0 \Delta)^2$. In each vertex the argument in α_s is given by the largest of the adjacent $k_\perp$-values. This implies in this case two factors α_0/κ_1 and no factor α_0/κ_2. (Due to the singular behaviour of α_s, we should not neglect the difference between α_0/κ_1 and α_0/κ_2 for these low κ-values.) Neglecting constraints other than the fact that κ_1 must be larger

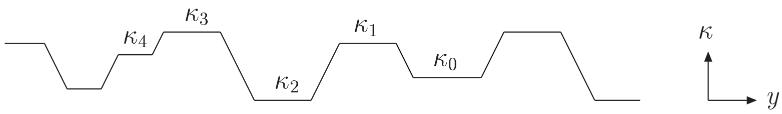

Figure 2.4: *The initial part of a chain dominated by alternating steps up and down in κ.*

than κ_2, we therefore get as a first estimate the relation

$$(\alpha_0 \Delta)^2 = \int_{\kappa_c}^{\infty} \left(\frac{\alpha_0}{\kappa_1}\right)^2 d\kappa_1 d\kappa_2 \theta(\kappa_1 - \kappa_2) \exp[-(1+\lambda)(\kappa_1 - \kappa_2)]. \tag{2.33}$$

Here $\kappa_c \equiv \ln(k_{\perp cut}^2/\Lambda^2)$. A factor $\exp[-(\kappa_1 - \kappa_2)]$ corresponds to the factor $k_{\perp,i}^2/k_{\perp,i-1}^2$ in eq. (2.7) when $k_\perp$ is decreasing. A further factor $\exp[-\lambda(\kappa_1 - \kappa_2)]$ follows because $\kappa_1 - \kappa_2$ is the minimum step in $l = \ln 1/x$, and in this interval there can be no other vertices. Without such a constraint G would in this l-interval grow by a factor $\exp[\lambda(\kappa_1 - \kappa_2)]$, and the constraint therefore corresponds to the compensating factor $\exp[-\lambda(\kappa_1 - \kappa_2)]$ in the integrand.

In the estimate in eq. (2.33) the constraints $\kappa_1 > \kappa_0$ and $\kappa_2 < \kappa_3$ are not taken into account. Most important is here the first inequality. Due to the factor $1/\kappa_1^2$, small κ_1-values give a large contribution to the integral in eq. (2.33), which is reduced when the constraint $\kappa_1 > \kappa_0$ is taken into account. Integrating over κ_1, we obtain from eq. (2.33) also the normalized distribution, $P(\kappa_2)$, in κ_2:

$$P(\kappa_2) = \frac{1}{e^{\widehat{\lambda}\kappa_c} E_1(\widehat{\lambda}\kappa_c)} \left\{ \frac{1}{\kappa_2} - \widehat{\lambda} e^{\widehat{\lambda}\kappa_2} E_1(\widehat{\lambda}\kappa_2) \right\} \tag{2.34}$$

where the function E_1 is an exponential integral and $\widehat{\lambda} \equiv 1 + \lambda$. Within our approximation, this expression also describes the distribution in the earlier "low step" κ_0. Thus the constraint $\kappa_1 > \kappa_0$ gives an extra weight (where P is given by eq. (2.34))

$$Prob(\kappa_0 < \kappa_1) = \int_{\kappa_c}^{\kappa_1} P(\kappa_0) d\kappa_0 = 1 - \frac{e^{\widehat{\lambda}\kappa_1} E_1(\widehat{\lambda}\kappa_1)}{e^{\widehat{\lambda}\kappa_c} E_1(\widehat{\lambda}\kappa_c)}. \tag{2.35}$$

Including this factor in the integrand in eq. (2.33) we obtain (after integrating over κ_2) the relation

$$\Delta^2 = \int_{\kappa_c}^{\infty} \left(\frac{1}{\kappa_1}\right)^2 d\kappa_1 \left[1 - \frac{e^{\widehat{\lambda}\kappa_1} E_1(\widehat{\lambda}\kappa_1)}{e^{\widehat{\lambda}\kappa_c} E_1(\widehat{\lambda}\kappa_c)}\right] \frac{1}{\widehat{\lambda}} \left[1 - e^{-\widehat{\lambda}(\kappa_1 - \kappa_c)}\right]. \qquad (2.36)$$

It would be possible to include a similar factor representing the constraint $\kappa_2 < \kappa_3$, and then, in an iterative scheme, also use the improved distributions to find new weights. This procedure would, however, be algebraically quite complicated, and not motivated in view of the qualitative nature of our approximation.

A numerical evaluation of the integral in eq. (2.36) gives the relation between $\Delta = \lambda/\alpha_0$ and κ_c presented in Fig. 2.5.[2] In this figure we also show the exact result presented in ref. [7], obtained by solving an integral equation which includes the effect from all possible chains. The dotted line is obtained using a more accurate integration over azimuth angles, while the dashed line is obtained using the approximations in eq. (2.7), and therefore corresponds more directly to our present model. We see that the result from eq. (2.36) indeed well reproduces the qualitative behaviour of the full solution. The neglect of "double steps" in the chains implies a somewhat lower value for Δ (our result lies between the two curves from ref. [7]), but the qualitative agreement gives further support to our assumption that this type of chains gives the dominant contribution for small x, for both large and small $k_\perp^2$.

Conclusion:

For a running coupling it is easy to go up and down in $k_\perp$, only as long as $k_\perp$ is small and α_s large. Therefore dominating chains contain a non-ordered part with small $k_\perp$-values, and an ordered part, where $k_\perp$ increases towards its final value. If the effective phase space for the variables $u_i = \ln k_{\perp i}^2$ in the non-ordered part is denoted Δ, then the expression in eq. (2.24) interpolates smoothly between the DGLAP and BFKL regions. The BFKL exponent is given by $\lambda = \alpha_0 \Delta$, and the transition between the regimes occurs for a fixed ratio between $u = \ln\ln k_\perp^2$ and $l = \ln(1/x)$, $u/l \approx \lambda^2/\alpha_0$.

2.4 Non-leading contributions

The replacement $\kappa^N \to (\kappa + N\delta)^N$ in eq. (2.9) includes the effect of non-leading terms in $\ln k_\perp^2$. In ref. [2] it is discussed how a similar modification of the factor l^N can account for some non-leading $\ln 1/x$ effects.

[2]We note that the integral in eq. (2.36) is a function only of the product $\widehat{\lambda}\kappa_c$. Thus the relation between Δ and κ_c is easily obtained by calculating the integral for different values of $\widehat{\lambda}\kappa_c$. This gives directly Δ and its corresponding value for $\kappa_c = \widehat{\lambda}\kappa_c/(1 + \Delta\alpha_0)$.

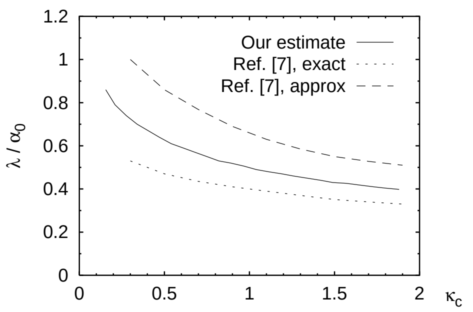

Figure 2.5: *The effective phase space $\Delta = \lambda/\alpha_0$ as a function of $\kappa_{cut} = \ln(k_{\perp cut}^2/\Lambda^2)$. The estimate from eq. (2.36) is shown together with the results from solving the LDC integral equation in reference [7]. Here the upper (dashed) line is obtained using the approximations in eq. (2.7), which are also used in our model.*

It is well-known that non-leading contributions have a significant influence on the value of the BFKL exponent λ [2, 8]. The $1/z$ pole in the splitting function gives the leading contribution to the growth of the structure functions for small x. The contribution from the $1/(1-z)$ pole is compensated by a Sudakov form factor [1]. This is related to the fact that, when a gluon is split into two gluons with energy fractions z and $1-z$ with $z << 1$, then the softer one can be regarded as a new emission, while the harder one (with energy $1-z$) corresponds to the original parent gluon, only with slightly reduced energy. Instead of including the $1/z$ pole for $0 < z < 1$ and neglecting the $1/(1-z)$ pole, it would also be possible to take both poles into account, but restrict the z-interval to $0 < z < 0.5$. This gives approximately the same result due to the relation

$$\int_\epsilon^1 \frac{1}{z} dz = \int_\epsilon^{0.5} \left[\frac{1}{z} + \frac{1}{1-z} \right] dz = \ln 1/\epsilon. \tag{2.37}$$

Including the non-singular terms in the splitting function

$$P_{gg} \propto \frac{1}{z} + \frac{1}{1-z} - 2 + z(1-z) \tag{2.38}$$

reduces this integral. Integrating from ϵ to 0.5 gives

$$\int_\epsilon^{0.5} P_{gg}(z) dz \propto \ln 1/\epsilon - \frac{11}{12}. \tag{2.39}$$

In analogy with eq. (2.37) we get exactly the same result if we split P_{gg} in the following way in two symmetric parts, singular at $z = 0$ and $z = 1$ respectively

$$P_{gg} \propto \frac{1 + (1 - z)^3}{2z} + \frac{1 + z^3}{2(1 - z)} \tag{2.40}$$

and then integrate the first term from 0 to 1. (This division corresponds to the separation used in the dipole cascade model [9], but the same result is obtained for any other symmetric separation.) The result in eq. (2.39) implies that the effective phase space for the l_i integrations in e. g. eq. (2.2) is reduced. It corresponds to an effective limit $\ln 1/z_i = l_i - l_{i-1} > a$ instead of $l_i - l_{i-1} > 0$, with $a \approx 11/12$. This means that instead of the factor $l^N/N!$, the l_i integrals give the result $(l - aN)^N/N!$. Thus in eqs. (2.9) and (2.24) we should make the substitutions

$$l^N/N! \rightarrow (l - aN)^N/N!. \tag{2.41}$$

Such a substitution was discussed in ref. [2] and shown to imply a significant reduction in the value of λ. Using Sterling's formula it is easy to show the following relation between the old value λ and the new, called λ':

$$\ln \frac{\lambda}{\lambda'} = a\lambda'. \tag{2.42}$$

Thus for $a = 11/12$ and $\lambda = 0.5$ we obtain $\lambda' \approx 0.35$.

In principle the effect is, however, not restricted to a reduction of the exponent λ. The factor $(l - aN)^N/N!$ also means that there is a strict upper limit, $N < l/a$, to the sum over N in eqs. (2.9) and (2.24). The increase for very large $k_\perp$-values is due to contributions from large values of N, and therefore this restriction implies that the distribution in κ will turn over for large values of κ. In the large $k_\perp$-limits of eqs. (2.10) and (2.28) the dominating contributions come from N-values around $N_{max} = \sqrt{\bar{\alpha} l \kappa}$ (fixed coupling) or $N_{max} = \sqrt{\alpha_0 l u}$ (running coupling). Therefore there is a suppression for $k_\perp$-values such that $N_{max} > l/a \approx l$, which means $\kappa > l/\bar{\alpha}$ for fixed coupling and $u = \ln(\kappa/\kappa_c) > l/\alpha_0$ for running coupling. For running coupling and small x this corresponds, however, to unrealistically large $k_\perp$-values. Consequently the dominant effect of these non-leading terms is just a reduction of the BFKL exponent λ, in accordance with eq. (2.42). (This reduction also implies that the boundary between the the BFKL and DGLAP regimes becomes somewhat modified. Thus the ratios in eqs. (2.18) and (2.30) are reduced by a factor $\frac{\lambda'}{\lambda(1+a\lambda')}$.)

2.5 Laplace transforms

Taking the Laplace transform of the sum in eq. (2.9), relevant for a fixed coupling, does not give a simple expression. However, for a running coupling it is easy to calculate the Laplace transforms of the expression in eq. (2.24). For the single Laplace transform we find

$$\widetilde{G}(\omega, u) = \int dl e^{-\omega l} G(l, u) = \frac{1}{\omega - \lambda} \cdot e^{\frac{\alpha_0 u}{\omega}}. \tag{2.43}$$

Thus we have a simple pole for $\omega = \lambda$ and an essential singularity for $\omega = 0$. The simple pole is in contrast to the case with a fixed coupling, where the factor $(\ln 1/x)^{-1/2}$ in eq. (2.11) implies a cut for $\omega < \lambda$. Denoting the mth term in the series in eq. (2.32) by $G_m(l, u)$ we also find

$$\widetilde{G}_m(\omega, u) = \frac{1}{\omega}(\frac{\lambda}{\omega})^m \cdot e^{\frac{\alpha_0 u}{\omega}}. \tag{2.44}$$

Here we see how the contributions for different m-values add up to the pole at $\omega = \lambda$, and thus to the power-like increase $\sim x^{-\lambda}$ for small x.

Including the non-leading effects from the substitution in eq. (2.41), the result is somewhat more complicated, but the singularity at $\omega = \lambda$ is still a simple pole and not a cut.

Finally we note that the double Laplace transform of eq (2.24) has a very simple form (note that this is the Laplace transform in $u = \ln\ln k_\perp^2$ and not in $\ln k_\perp^2$)

$$\widetilde{G}(\omega, \gamma) = \int dl\, e^{-\omega l} \int du\, e^{-\gamma u} G(l, u) = \frac{1}{(\omega - \lambda)(\gamma - \frac{\alpha_0}{\omega})}. \tag{2.45}$$

2.6 Summary

A simple model is presented, which interpolates smoothly between the DGLAP and BFKL regimes. It is based on the CCFM and LDC models and incorporates the most essential features of these models. Although not meant for quantitative analyses, it provides an intuitive picture of the transition between the two domains.

To leading order in $\ln 1/x$ we get for a constant coupling

$$\mathcal{F}(x, k_\perp^2) \approx \bar{\alpha} \sum_N \frac{(\bar{\alpha} l)^N}{N!} \frac{(\kappa + N\delta)^N}{N!} \tag{2.46}$$

where $\mathcal{F}$ is the non-integrated gluon structure function, $l = \ln 1/x$, $\kappa = \ln k_\perp^2$, and $\bar{\alpha} = 3\alpha_s/\pi$. The parameter δ should be of order 1, and the BFKL power is given by $\lambda = e\delta\bar{\alpha}$, which is very close to the leading order BFKL result. The transition between the DGLAP and BFKL regimes occurs for the fixed ratio

$$\frac{\kappa}{l} = \frac{\ln k_\perp^2}{\ln 1/x} \approx e\,\bar{\alpha}. \tag{2.47}$$

For a running coupling we get instead

$$\frac{\kappa}{\alpha_0}\mathcal{F} \equiv G \approx \sum_N \frac{(\alpha_0 l \Delta)^N}{N!} \sum_{k=0}^{N} \frac{(u/\Delta)^k}{k!} \tag{2.48}$$

where $u = \ln\ln k_\perp^2 - \ln\ln k_{\perp cut}^2$ and α_0 is defined by the relation $3\alpha_s/\pi = \alpha_0/\kappa$. The parameter Δ is sensitive to the cutoff for small $k_\perp$ (see Fig. 2.5), and related to the BFKL power by the equation $\lambda = \alpha_0 \Delta$. In this case the transition occurs for

$$\frac{u}{l} = \frac{\ln\ln k_\perp^2}{\ln 1/x} \approx \frac{\lambda^2}{\alpha_0}. \tag{2.49}$$

Some non-leading effects in $\ln 1/x$ can be taken into account by replacing the factor l^N in eqs. (2.9) and (2.24) by $(l - aN)^N$ with $a \approx 11/12$. The result is mainly just a smaller value for the BFKL exponent λ (in agreement with results in refs. [2, 4]).

While the Laplace transform for a fixed coupling has a cut for $\omega < \lambda$, for a running coupling the singularity at $\omega = \lambda$ is only a simple pole.

2.7 Acknowledgments

We would like to thank Bo Andersson and Leif Lönnblad for many valuable discussions.

References

[1] M. Ciafaloni, Nucl. Phys. **B296** (1988) 49
S. Catani, F. Fiorani and G. Marchesini, Phys. Lett. **B234** (1990) 339, Nucl. Phys. **B336** (1990) 18.

[2] B. Andersson, G. Gustafson and J. Samuelsson, Nucl. Phys. **B467** (1996) 443
H. Kharraziha and L. Lönnblad, JHEP **03** (1998) 006

[3] V.N. Gribov and L.N. Lipatov, Sov. J. Nucl. Phys. **15** (1972) 438 and 675
G. Altarelli and G. Parisi, Nucl. Phys. **B126** (1977) 298
Yu.L. Dokshitzer, Sov. Phys. JETP **46** (1977) 641

[4] E.A. Kuraev, L.N. Lipatov and V.S. Fadin, Sov. Phys. JETP **45** (1977) 199
Ya.Ya. Balitsky and L.N. Lipatov, Sov. J. Nucl. Phys. **28** (1978) 822

[5] E.M. Levin and M.G. Ryskin, Phys. Rep. **189** (1990) 267
J. Bartels and H. Lotter, Phys. Lett. **B309** (1993) 400
J.R. Forshaw, P.N. Harriman and P.J. Sutton, Nucl. Phys. **B146** (1994) 739

[6] B. Andersson, G. Gustafson, H. Kharraziha and J. Samuelsson, Z. Phys. **C71** (1996) 613

[7] B. Andersson, G. Gustafson and H. Kharraziha, Phys.Rev. **D57** (1998) 5543

[8] V.S. Fadin and L.N. Lipatov, Phys. Lett. **B429** (1998) 127
M. Ciafaloni and G. Camici, Phys. Lett. **B430** (1998) 349

[9] G. Gustafson and U. Pettersson, Nucl. Phys. **B306** (1988) 746

Gluon Distribution Functions in the $k_\perp$-factorization Approach

Paper III

Gluon Distribution Functions in the $k_\perp$-factorization Approach

Gösta Gustafson, Leif Lönnblad and Gabriela Miu

Department of Theoretical Physics
Lund University, Sölvegatan 14A, S-223 62 Lund, Sweden

Journal of High Energy Physics **09**, 005 (2002)

Abstract

At small x, the effects of finite transverse momenta of partons inside a hadron become increasingly important, especially in analyses of jets and heavy-quark production. These effects can be systematically accounted for in a formalism based on $k_\perp$-factorization and unintegrated distribution functions. We present results for the unintegrated distribution function, together with the corresponding integrated one, obtained within the framework of the Linked Dipole Chain model. Comparisons are made to results obtained within other approaches.

3.1 Introduction

In the description of a given cross section in deeply inelastic lepton–hadron scattering (DIS), it is not enough to consider only the leading order perturbative terms. Although $\alpha_{\rm s}$ may be small, each power of $\alpha_{\rm s}$ may be accompanied by large logarithms due to the large phase space available for additional gluon radiation. It is, however, often possible to resum these emissions to all orders in the leading logarithmic approximation (LLA).

The most familiar resummation strategy is based on DGLAP [1, 2, 3, 4] evolution, which resums large logarithms of the virtual photon momentum transfer, Q^2. Within this formalism, the cross-section for any given physics process is calculated using collinear factorization of the form

$$\sigma(x,Q^2) = \sigma_0(x,Q^2)\sum_a \int \frac{\mathrm{d}z}{z}\, C^a(z)\, f_a(\frac{x}{z},Q^2), \tag{3.1}$$

i.e. as a convolution of coefficient functions C^a and parton densities $f_a(x,Q^2)$.

DGLAP evolution describes most experimental results[1] from electron–proton and proton–proton colliders. By using input parton densities which are sufficiently singular when $x \to 0$, this formalism can also account for the strong rise of F_2 for small x, as observed at HERA. However, there are problems with the description of non-inclusive observables such as forward jet production in ep and heavy-quark production in ep and pp collisions.

In the region of very small x (asymptotically large energies), effects of finite transverse momenta of the partons may become more and more important. The appropriate description in this region of phase space is BFKL evolution [6, 7]. The cross-sections are calculated in the $k_\perp$-factorization approach of the form

$$\sigma(x,Q^2) = \int \frac{\mathrm{d}z}{z}\, \mathrm{d}^2k_\perp\, \hat{\sigma}(z,Q^2,k_\perp^2)\, \mathcal{F}(\frac{x}{z},k_\perp^2), \tag{3.2}$$

i.e. as a convolution over the energy fraction z and the transverse momentum $k_\perp$ of the incoming parton of off-shell partonic cross-sections $\hat{\sigma}$, and $k_\perp$-unintegrated parton densities[2], $\mathcal{F}(x,k_\perp^2)$. This corresponds to a resummation of large logarithms of $1/x$. The BFKL evolution equation actually predicts a strong power-like rise of F_2 at small x.

Both the DGLAP and BFKL evolution were developed to describe inclusive quantities such as F_2, but they can be interpreted as an explicit summation of initial-state bremsstrahlung of quasi-real partons, and can thus, together

[1] see e.g. [5] for a recent review.

[2] In this paper we will use $\mathcal{F}$ for the unintegrated parton distributions in general, and $\mathcal{G}$ for the unintegrated gluon distribution, treated as densities in $\log 1/x$, i.e. $\mathcal{G}(x) = xG(x)$. For the integrated ones we will use the standard notation f and g respectively.

with appropriately added final-state bremsstrahlung, also be used to describe exclusive multi-parton final states.

There exist a couple of models which take into account large logarithms of both Q^2 and $1/x$ in DIS. One such model, valid for both small and large x, has been developed by Ciafaloni, Catani, Fiorani and Marchesini, and is known as the CCFM model [8, 9]. The resulting unintegrated distribution functions, $\mathcal{F}(x, k_\perp^2, \overline{q})$, depend on two scales, the additional scale, $\overline{q}$, being a variable related to the maximum angle allowed in the emission. A problem with this approach is that the non-singular terms in the splitting function have not been included in a fully consistent way, and therefore CCFM does not fully reproduce the DGLAP result in the large Q^2 limit.

The Linked Dipole Chain model (LDC) [10, 11] is a reformulation and generalization of the CCFM model. It is based on the observation that the dominant features of the parton chains are determined by the subset of emitted gluons, which are ordered in both light-cone components, q_+ and q_-, and which significantly change the transverse momentum of the propagating gluon. This subset was called "primary" gluons, or the backbone of the chain. In LDC this subset of emissions is treated as initial state radiation, while all other emissions are treated as final state radiation. The result is that the evolution can be described by essentially single-scale dependent unintegrated distributions, $\mathcal{F}(x, k_\perp^2)$. However, as discussed further below, the $1/(1-z)$ pole in the splitting function does imply some dependence on the scale $\bar{q}$ also in the LDC formalism. It should be noted that the standard LDC formulation does not exactly reproduce the leading BFKL behavior for fixed coupling, but with a small modification almost identical results can be obtained (see section 4.3).

Like the DGLAP and BFKL equations, also the CCFM and LDC formalisms can be used to describe exclusive final states. To do this it is essential to add final state radiation in regions appropriate for the particular formalism used. In particular many gluons included as initial state radiation in the evolution chain in CCFM are added in a later phase as final state radiation in LDC. Although very similar, this separation is also different in the BFKL and CCFM formalisms, as discussed in refs. [12] and [13]. These schemes give the same result only after soft collinear emissions have been included as final state radiation.

In this article we present results for the integrated and unintegrated gluon distribution functions obtained within the LDC formalism and make comparisons with the CCFM model and with results from other formalisms. The article is organized as follows. We start in section 4.2 by giving a short introduction to the DGLAP and BFKL formalisms for deeply inelastic *ep* scattering, moving over to a description of the CCFM model. We end this section with a somewhat more elaborate description of the Linked Dipole Chain model for DIS, which is implemented in the Monte Carlo event generator LDCMC [14].

This program can be used to describe both structure functions and exclusive properties of the hadronic final states.

As mentioned above the definition of the chains in the initial parton evolution is different in the different schemes. Therefore also the gluon distribution functions, which are not experimental observables, are not uniquely defined, but depend on the formalism used. We discuss this problem, and some different approaches presented in the literature, in section 3.3.

In section 4.6 we present our results for the unintegrated and integrated gluon distribution functions, obtained in the LDC formalism as implemented in LDCMC. These results are also compared to those of other approaches, and we discuss how to make relevant comparisons between the different formalisms.

We end this article with a summary in section 3.5.

3.2 Deep Inelastic Scattering

Typically a deeply inelastic scattering event is represented by a fan diagram, as the one shown in figure 4.1. The (quasi-)real emitted gluons, constituting the initial-state radiation, are labeled q_i, while the virtual propagators are referred to as k_i. The figure represents an exclusive final state, with the final-state radiation explicitly marked as the dashed lines. The final-state emissions have to be defined so that they do not affect the cross-section and give negligible recoils to the emitting partons. The exact separation between initial- and final-state radiation is not the same in the different formalisms discussed in the following subsections, and consequently the exclusive initial chains, as well as the distribution functions, are also different. This problem will be further discussed in sections 3.3 and 4.6.

We will here mostly discuss purely gluonic chains, which should give the dominating contributions at small x. We will use different approximations of the gluon splitting function $P_{\mathrm{gg}}(z) = \frac{1}{z} + \frac{1}{1-z} - 2 + z(1-z)$. Splitting a gluon means that we have two new gluons, carrying fractions z and $1-z$ of the original gluon energy, which contribute to the gluon density, while the contribution from the original one must be subtracted.

In analytical calculations of the distribution functions, the subtraction is achieved with the so-called plus prescription for the pole at $z = 1$ and the addition of a term proportional to $\delta(1-z)$ to the splitting function. At asymptotically small x, in the double leading logarithmic approximation, the distribution functions can be obtained by considering only the $1/z$ pole of the splitting function, thus effectively only adding one gluon, neglecting the recoil for the emitting mother gluon. In this way the problem with subtraction is avoided altogether. (Although less important for the qualitative properties, the non-leading terms are very essential for the quantitative results, e.g. for the power λ determining the increase for small x-values [10, 15, 16].)

The singularity at $z = 1$ is less important for the distribution functions, but if one is also interested in the properties of exclusive final states the effects of this pole cannot be neglected. When both poles are included in the splitting function the subtraction can be handled by a Sudakov form factor, which multiplies each splitting and represents the probability that the gluon to be split has not already been split before. Here *before* has to be defined by the ordering imposed on the emissions (e.g. $k_\perp$-ordering in DGLAP and angular ordering in CCFM). In an approximation where the non-singular terms in P_{gg} (i.e. the terms $-2 + z(1-z)$) are neglected, the Sudakov form factor, Δ_{S}, is given by

$$\ln \Delta_{\mathrm{S}} = -\int \overline{\alpha} \frac{dq_\perp^2}{q_\perp^2} \frac{dz}{1-z} \Theta_{\mathrm{order}}, \tag{3.3}$$

where $\overline{\alpha} = 3\alpha_{\mathrm{s}}/\pi$. This definition is used in the CCFM approach. Equivalently the Sudakov form factor can be obtained by considering energy-momentum conservation [17] and be written

$$\ln \Delta_{\mathrm{S}} = -\int \overline{\alpha} \frac{dq_\perp^2}{q_\perp^2} z dz P_{\mathrm{gg}}(z) \Theta_{\mathrm{order}}. \tag{3.4}$$

Here the non-singular terms in P_{gg} can be included without problems, and this method is used in the LDCMC generator.

As mentioned above, the $1/(1-z)$ singularity and the associated Sudakov form factor are essential for the exclusive final state properties, but not equally important for the distribution functions. To simplify the notation and make the presentation more transparent, we will in the discussions in the rest of this section only include the effects of the $1/z$ pole. The effects of the remaining terms in the splitting function and the associated Sudakov form factor will instead be discussed in sections 3.3 and 4.6. In section 4.6 we will also consider the convolution of the perturbative evolution with non-perturbative input parton densities, which will also be ignored in the remainder of this section.

3.2.1 DGLAP and BFKL

In the DGLAP region, characterized by large Q^2 and limited $1/x$, the dominating contributions come from $k_\perp$-ordered chains which fulfill $Q^2 \gg k_{\perp n}^2 \gg k_{\perp,n-1}^2 \gg \ldots$ and $k_{+i} > k_{+,i+1}$. In the limit where also x is small, so that we can approximate the gluon splitting function with $P_{gg}(z) \approx 1/z$ (in the double leading log approximation – DLLA) we can write the unintegrated gluon distribution function for a fixed coupling α_{s} on the form

$$\mathcal{G}(x, k_\perp^2) \quad \sim \quad \sum_n \int \prod^n \bar{\alpha} \frac{dx_i}{x_i} \frac{dk_{\perp i}^2}{k_{\perp i}^2} \theta(x_{i-1} - x_i) \theta(k_{\perp,i}^2 - k_{\perp,i-1}^2)$$

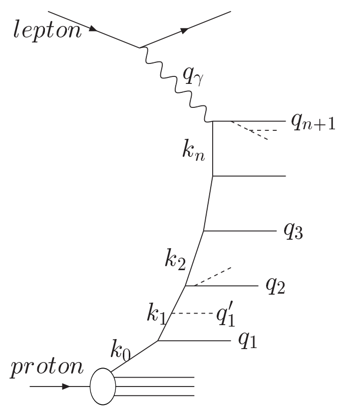

Figure 3.1: A fan diagram for a DIS event. The quasi-real partons from the initial-state radiation are denoted q_i, and the virtual propagators k_i. The dashed lines denote final-state radiation.

$$\sim \sum_n \bar{\alpha}^n \frac{(\ln 1/x)^n}{n!} \frac{(\ln Q^2)^n}{n!} \approx \exp(2\sqrt{\bar{\alpha} \ln Q^2 \ln 1/x}).$$
$$\text{where } \bar{\alpha} \equiv \frac{3\alpha_s}{\pi} \text{ and } x_i \equiv k_{+i}/P_{+,tot}. \tag{3.5}$$

In the case of a running coupling, $\overline{\alpha}(Q^2) \equiv \alpha_0 / \ln Q^2$, we get the same exponential expression but with $\ln Q^2$ replaced by $\ln(\ln Q^2)$ and $\overline{\alpha}$ by α_0.

In the BFKL region of very small x and limited Q^2, chains that are not ordered in $k_\perp$ need to be accounted for, even though they are suppressed. The resulting unintegrated distribution function increases like a power at small x:

$$\mathcal{G} \sim \frac{1}{x^\lambda} \, \mathrm{f}(k_\perp, x), \tag{3.6}$$

with the function $\mathrm{f}(k_\perp, x)$ describing a random walk in $\ln(k_\perp^2/\Lambda_{QCD}^2)$ [18, 19, 20, 11]. Such a power-like behavior is in approximate agreement with HERA data, with $\lambda \sim 0.3$. We note, however, that a corresponding increase is also obtained from NLO DGLAP evolution with appropriately adjusted input distribution functions.

3.2.2 CCFM

The particular calculation scheme adopted by Ciafaloni, Catani, Fiorani and Marchesini has resulted in the well-known CCFM model [8, 9]. This model has been developed assuming purely gluonic chains. Further, only the singular terms in the splitting functions are included in a fully consistent way. Colour coherence implies that the initial-state emissions are ordered in angle (or equivalently in rapidity). According to the definition of the separation between initial- and final-state radiation, they are also ordered in the positive (along the incoming proton) light-cone momentum q_+. All other kinematically allowed emissions (symbolized by the q'_1 emission in figure 4.1) are defined as final-state emissions.

The CCFM model is based on the $k_\perp$-factorization formalism, and if we neglect the $1/(1-z)$ pole, the unintegrated distribution function in the small-x limit is given by

$$\begin{aligned}\mathcal{G}(x, k_\perp^2, \overline{q}) \quad \sim \quad & \sum_n \int \prod^n \bar{\alpha} \frac{dz_i}{z_i} \frac{d^2 q_{\perp i}}{\pi q_{\perp i}^2} \Delta_{ne}(z_i, k_{\perp i}^2, \overline{q}_i) \times \\ & \delta(x - \Pi z_i) \theta(\overline{q}_i - \overline{q}_{i-1} z_{i-1}) \delta(k_\perp^2 - k_{\perp n}^2) \theta(\overline{q} - \overline{q}_n z_n).\end{aligned} \tag{3.7}$$

The notation is that of figure 4.1, i.e. $q_{\perp i}$ and $k_{\perp i}$ are the transverse momenta of the real and virtual partons, respectively. The splitting parameter z is defined as $z_i = k_{+,i}/k_{+,i-1}$, and the so-called rescaled transverse momentum $\overline{q}_i$ is defined by $\overline{q}_i \equiv q_{\perp i}/(1 - z_i)$. The interval for the z-variables is between 0 and 1, which guarantees ordering in q_+, and the angular ordering condition is satisfied by the constraint

$$\overline{q}_i > \overline{q}_{i-1} z_{i-1}, \tag{3.8}$$

explicitely written out in eq. (4.1). Moreover, we note the occurrence of the so-called non-eikonal form factor $\Delta_{ne}(z, k_\perp^2, \overline{q})$ defined in ref. [9]. The distribution function, $\mathcal{G}$, depends on two separate scales, the transverse momentum, $k_\perp$, of the interacting gluon, and $\overline{q}$, which determines an angle beyond which there is no (quasi-) real parton in the chain of initial-state radiation. In the rest frame of the incoming proton, this limiting angle corresponds to a rapidity given by (if counted negative in the direction of the probe)

$$y_{\lim} = \ln \left(x \frac{m_p}{\overline{q}} \right) \tag{3.9}$$

In the original formulation there was also the so-called consistency constraint

$$k_{\perp i}^2 > z_i q_{\perp i}^2, \tag{3.10}$$

which guarantees that the virtuality k^2 is well approximated by $-k_\perp^2$. The relevance of this constraint has been debated and has been disregarded in some analyses [21].

The CCFM evolution has been implemented in two hadron-level event generators, SMALLX [22, 23] and CASCADE [24] (which of course include also the $1/(1-z)$ pole), both maintained by Hannes Jung. These programs reproduce HERA data on F_2 well for small x, where purely gluonic chains should give the dominating contribution. For larger x, we expect a large contribution from valence quarks; such chains are not easily accounted for in the CCFM formalism and are not included in the programs.

Both programs are able to reproduce a wide range of final-state observables. We note, however, that there is a large sensitivity to uncertain non-leading corrections. In particular this is the case for forward-jet production at HERA. The non-singular terms in the gluon splitting function can not be included in a fully consistent way, and they are not included in the original CCFM formulation. With this version of the MC the experimental forward-jet rates are well described. If, however, the non-singular terms are included in an approximate way, which would be a more natural option, the jet rates come out approximately a factor two below the data [5].

3.2.3 The Linked Dipole Chain Model

The Linked Dipole Chain model (LDC) is also formulated in terms of $k_\perp$-factorization and unintegrated distribution functions. It is a reformulation and generalization of the CCFM model, in which the separation between initial state bremsstrahlung (ISB) and final state bremsstrahlung (FSB) has been modified. This results in a more simple description, with the unintegrated distribution functions being (essentially) dependent on only one scale and allowing for some sub-leading corrections to be introduced in a rather straight-forward manner.

The LDC model is based on the observation that the dominant features of the parton chains are determined by the subset of emitted gluons, which is ordered in both light-cone components, q_+ *and* q_-, (which implies that they are also ordered in angle or rapidity y) and with $q_{\perp i}$ satisfying the constraint

$$q_{\perp i} > \min(k_{\perp i}, k_{\perp, i-1}). \tag{3.11}$$

In LDC this subset (called “primary” gluons, or the backbone of the chain) forms the chain of initial state radiation, and all other emissions are treated as final state radiation.

This redefinition of the ISB–FSB separation implies that one single chain in the LDC model corresponds to a set of CCFM chains. As was shown in ref. [10], when one considers the contributions from all chains of this set, with their corresponding non-eikonal form factors, they just add up to one. Thus, the non-eikonal form factors do not appear explicitly in LDC. The result is a simpler form for the unintegrated distribution functions, $\mathcal{F}(x, k_\perp^2)$, which essentially depend only on a single scale, $k_\perp^2$. Since many of the gluons which make up the initial-radiation chain in the CCFM model, are treated as final-state radiation in the LDC formalism, typical z-values are smaller in the LDC model and most of the problem of angular ordering is postponed to the treatment of the final-state radiation. However, as discussed further below, the $1/(1-z)$ pole in the splitting function does imply some dependence on the scale $\bar{q}$ also in the LDC formalism.

Again keeping only the $1/z$ pole, we find for the gluon distribution in the LDC formalism

$$\begin{aligned}\mathcal{G}(x,k_\perp^2) \quad &\sim \quad \sum_n \int \prod^n \bar{\alpha}\frac{dz_i}{z_i}\frac{d^2q_{\perp i}}{\pi q_{\perp i}^2}\theta(q_{+,i-1}-q_{+i})\theta(q_{-i}-q_{-,i-1}) \times \\ &\qquad \delta(x-\Pi z_i)\delta(\ln k_\perp^2 - \ln k_{\perp n}^2). \end{aligned} \tag{3.12}$$

The notation in the above and what will follow refers to that of figure 4.3. Here, a typical DIS event is shown together with the corresponding phase space available in the γ-p rest frame, where the rapidity, y, and the transverse momentum, $q_\perp$, of any final-state parton are limited by a triangular region in the $(y, \ln q_\perp^2)$-plane. The proton direction is towards the right end of the triangle, and the photon direction is towards the left. The real emitted (ISB) gluons are represented by points in this diagram. The virtual propagators do not have well defined rapidities, and are represented by horizontal lines, the left and right ends of which have the coordinates $(\ln[k_{+i}/k_{\perp i}], \ln k_{\perp i}^2)$ and $(\ln[-k_{\perp i}/k_{-i}], \ln k_{\perp i}^2)$ respectively. The phase space available for FSB is given by the area below the horizontal lines (including the folds that stick out of the main triangle).

The fact that the dominant properties of the evolution are determined by the subset of "primary" emissions has been further studied in ref. [12], where they are called k-changing gluons. That paper also discusses the effect of emissions close to the boundary of the constraint in eq. (3.11), which are important for single logarithmic accuracy. In fact, with the constraint (3.11) LDC does not exactly reproduce the BFKL result. An almost identical value for the power λ, determining the increase for small x, is, however, obtained by the modified cut $q_{\perp i} > \sqrt{k_{\perp i}\cdot k_{\perp,i-1}}$ (in leading order for fixed α_s) [25].

Due to the different separation between ISB and FSB, it is important to include final state emissions before a comparison between exclusive final states in LDC and CCFM or BFKL. For a comparison between the final states obtained in CCFM and BFKL see refs. [12] [13].

The ordering of the CCFM evolution in q_+ but not in q_- means that this formalism is not left–right symmetric. In contrast the LDC formulation is completely symmetric, which implies that the chain in figure 4.3 can be thought of as evolved from either the photon or the proton end. (Thus, the LDC formalism automatically takes into account contributions from "resolved virtual photons".)

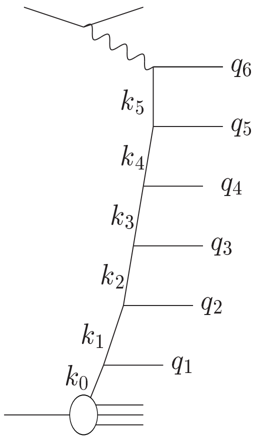

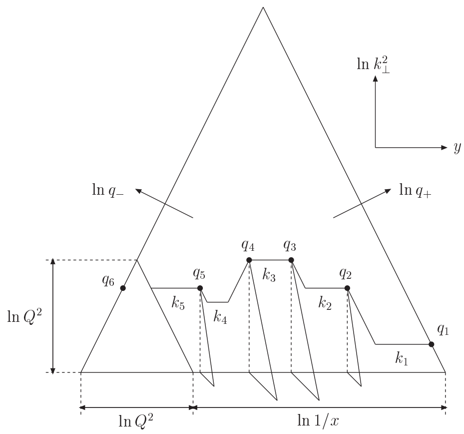

Figure 3.2: The initial-state emissions q_i in the $(y, \kappa = ln(k_\perp^2))$-plane. Final-state radiation is allowed in the region below the horizontal lines. The height of the horizontal lines determine $\ln k_{\perp i}^2$. The light-cone momenta k_{+i} and k_{-i} can be read off as described in the text.

Returning to eq. (3.12), we note that it can equally well be expressed in terms of the virtual propagator momenta. Due to the condition in eq. (3.11) we have $q_{\perp i}^2 \approx \max(k_{\perp i}^2, k_{\perp,i-1}^2)$ and, suppressing the θ- and δ-functions, we obtain

$$\mathcal{G} \sim \sum \int \prod \bar{\alpha} \frac{dz_i}{z_i} \frac{dk_{\perp i}^2}{\max(k_{\perp i}^2, k_{\perp,i-1}^2)}. \tag{3.13}$$

In particular we note that this implies that, for a "step up" or a "step down" in $k_\perp$, the following weights result:

$$\frac{d^2 q_{\perp i}}{q_{\perp i}^2} \approx \frac{d^2 k_{\perp i}}{k_{\perp i}^2}, \quad k_{\perp i} > k_{\perp,i-1} \quad \text{and} \tag{3.14}$$

$$\frac{d^2 q_{\perp i}}{q_{\perp i}^2} \approx \frac{d^2 k_{\perp i}}{k_{\perp i}^2} \cdot \frac{k_{\perp i}^2}{k_{\perp,i-1}^2}, \quad k_{\perp i} < k_{\perp,i-1}. \tag{3.15}$$

Thus, for a step down there occurs an additional suppression factor $k_{\perp i}^2 / k_{\perp,i-1}^2$.

The relation between the integrated and the unintegrated distribution functions are symbolically written as $xf(x, Q^2) \sim \int \frac{dk_\perp^2}{k_\perp^2} \mathcal{F}(x, k_\perp^2)$. The exact relationship is somewhat dependent on the evolution scheme used for $\mathcal{F}(x, k_\perp^2)$. For LDC we have

$$xf(x, Q^2) = \int^{Q^2} \frac{dk_\perp^2}{k_\perp^2} \mathcal{F}(x, k_\perp^2) + \int_{Q^2} \frac{dk_\perp^2}{k_\perp^2} \mathcal{F}(x\frac{k_\perp^2}{Q^2}, k_\perp^2) \frac{Q^2}{k_\perp^2}, \tag{3.16}$$

assuming a single-scale dependent unintegrated distribution function.

The first term of eq. (3.16) corresponds to chains whose struck parton is less virtual than the probe, $k_\perp^2 < Q^2$. The second term contains the suppressed contributions that come from chains whose struck parton has $k_\perp^2 > Q^2$; the suppression factor $Q^2/k_\perp^2$ is analogous to the one occurring in eq. (3.15). Note also that the x-argument in the unintegrated distribution function of the second term has been rescaled by the factor $k_\perp^2/Q^2$.

Below we list some properties of the LDC model:

- The natural scale in the running coupling, α_s, is $q_{\perp i}^2$, which coincides with $\max(k_{\perp i}^2, k_{\perp,i-1}^2)$.
- Non-leading effects such as those coming from quark-initiated chains, from the non-singular terms in the splitting functions and from energy-momentum conservation can be included in a straight-forward manner. It is also possible to correct the two emissions connected with the highest-virtuality link with the full $2 \to 2$ matrix element, thus improving the result. Finally, for the ISB emission closest to the photon end, the full off-shell $\mathcal{O}(\alpha\alpha_s)$ matrix element is used.
- The fact that fewer gluons are considered as initial-state radiation implies that typical z-values are smaller, thus resulting in smaller sub-leading corrections.
- The formalism is greatly simplified by the fact that the non-eikonal form factors do not appear explicitly in the model.
- The LDC formalism is fully left-right symmetric, in the sense that the result is independent of whether the evolution starts at the probe (photon) or target (proton) end. Hence it can easily be generalized to the case when the photon is replaced by a hadron. As a result, the formalism can be applied to the study of jet production in hadronic collisions [26, 27].
- Besides giving an inclusive description of the events, the result in eq. (3.13) (modified to include also the remaining terms of the splitting function) can also be interpreted as the production probability for an exclusive final state.

These qualities make LDC particularly suitable for implementation in an event generator. One such LDC-based Monte Carlo event generator, LDCMC, has been developed by Kharraziha and Lönnblad [14].

The LDCMC has been shown to be able to reproduce available F_2 data very well (see further section 4.6), not only the small-x data from of HERA but also data at higher x from fixed target experiments. This success relies on the fact that quark-initiated chains are easily incorporated in the evolution.

It should be mentioned that, just like the CCFM-based CASCADE, LDCMC has problems describing the H1 forward-jet data. Again the data can be reproduced only when the non-singular terms of the gluon splitting function are omitted. The more physical case of including the full splitting function predicts a distribution which is approximately a factor 2 below the data.

In section 4.6 we present results for the integrated and unintegrated gluon distribution functions obtained within the LDC formalism using the LDCMC simulation program. Before comparing these results with those of other approaches, we discuss in the following section the relationship between the integrated and unintegrated distribution functions in different formalisms.

3.3 Discussion on Different Distribution Function Definitions

In contrast to the structure function F_2, the unintegrated parton distributions are not experimental observables, and therefore depend on the specific scheme in which they are defined. The parton distribution functions and the hard sub-collision cross sections $\hat{\sigma}$ have to be defined consistently, so that the convolution in eq. (3.2) gives the experimentally observable cross section. It has also been argued that the unintegrated distributions are not gauge-invariant objects, which implies that there is a dependence on the gauge choice used for the off-shell matrix elements in the convolution [3].

For asymptotically large values of Q^2 or $1/x$ it is possible to define unintegrated parton distribution functions, $\mathcal{F}(x, k_\perp^2)$, which depend on a single scale, $k_\perp^2$, specifying the transverse momentum (or virtuality) of the interacting parton. In the DGLAP region the $k_\perp$-ordering of the links implies that we can define $\mathcal{F}(x, k_\perp^2)$ as the derivative of the integrated distribution functions, $xf(x, Q^2)$, and thus

$$xf(x, Q^2) = \int^{Q^2} \frac{dk_\perp^2}{k_\perp^2} \mathcal{F}(x, k_\perp^2) \tag{3.17}$$

Also in the BFKL equation the distribution functions are determined by a single scale. However, since the chains are not ordered in $k_\perp$, the integrated distribution function, $f(x, Q^2)$, also obtains contributions from $k_\perp$-values larger than Q^2, and therefore the simple relation in eq. (3.17) is not satisfied.

As discussed in section 3.2.2 the angular ordering in the CCFM model implies that the unintegrated distribution functions depend on two scales, $k_\perp$

[3]See e.g. discussions in [5] and [28]

and $\overline{q}$, where $\overline{q}$ specifies the limiting angle in eq. (3.9). (Note that the strong ordering in $k_\perp$ in DGLAP, or in x in BFKL, also automatically implies an ordering in angle, which makes this second scale redundant.) Varying this angular constraint has two effects:

(a) Increasing $\overline{q}$ implies additional contributions from chains with one (or more) emissions with rapidity in the now allowed angular range. These chains give a positive contribution to the distribution function. We also note that, as the chains have to end with transverse momentum $k_\perp$, most of them will have $q_\perp \lesssim k_\perp$, where $q_\perp$ is the transverse momentum of the emission in the new angular region.

(b) Emission of an extra gluon with $q_\perp > k_\perp$ will change the $k_\perp$ of the active gluon. This will give a negative contribution, which is described by a Sudakov form factor.

For large values of $\overline{q}$ the suppression from the Sudakov dominates, and $\mathcal{G}(x, k_\perp^2, \overline{q})$ decreases with increasing $\overline{q}$ for fixed x and $k_\perp$. However, for $\overline{q} \lesssim k_\perp$ the first effect dominates, and $\mathcal{G}$ increases with $\overline{q}$. In the CCFM formalism this dependence on $\overline{q}$ for fixed x and $k_\perp$ is very strong, when $\overline{q}$ varies in the neighborhood of $k_\perp$. The angular constraint is expressed by the last θ-function in eq. (4.1), which guarantees the relation

$$\overline{q} > \overline{q}_n z_n, \quad \text{where } \overline{q}_n \equiv \frac{q_{\perp n}}{1 - z_n} \tag{3.18}$$

This implies an upper limit for z_n of the last emission given by

$$z_n < z_{\text{lim}} = \frac{\overline{q}}{\overline{q} + q_\perp} \tag{3.19}$$

From this result we can see that if the scale $\overline{q}$ is chosen in the neighborhood of $k_\perp$, then a large fraction of the possible chains are cut away. To realize this we make two observations:

(i) For $\overline{q} = k_\perp$ we find $z_{\text{lim}} \approx 0.5$ when the last link is a step up in $k_\perp$ (in which case $q_\perp \approx k_\perp$), and $z_{\text{lim}} < 0.5$ when the last link is a step down (and $q_\perp > k_\perp$).

(ii) In the CCFM model the $1/z$ pole in the splitting function is screened by the non-eikonal form factor, and the z-distribution obtained in the SMALLX and CASCADE MCs therefore does not peak at small z-values, but has a maximum around $z = 0.5$ [5].

This implies that for $\overline{q} = k_\perp$ the constraint in eq. (3.19) will exclude a large fraction of the possible chains. Furthermore, the fact that for $\overline{q} = k_\perp$, z_{lim} approximately coincides with the maximum in the z-distribution implies that increasing (decreasing) $\overline{q}$ in the neighborhood of $k_\perp$ includes (excludes) a significant set of chains. Consequently, for fixed $k_\perp$, the structure functions depend strongly on $\overline{q}$ in this region. As we will see in the next section, $\mathcal{G}(x, k_\perp^2, \overline{q})$ approximately saturates when $\overline{q}$ approaches $2k_\perp$, before it decreases for very large $\overline{q}$-values.

A similar angular constraint can be introduced also in the LDC formalism, giving distribution functions depending on two separate scales. However, many emissions with $q_\perp < k_\perp$, which are treated as initial-state emissions in CCFM, are treated as final-state emissions in LDC. Typical z-values are smaller, since small z are not screened by a non-eikonal form factor. Therefore such a constraint on the initial state emissions has a smaller effect in LDC than in the CCFM scheme, and the LDC distributions vary much more slowly with $\overline{q}$ in the region $q_\perp \lesssim k_\perp$.

The quantities of primary interest are not the unobservable parton distributions, but the cross sections for physical processes, where the parton distribution is convoluted with a hard parton-parton sub-collision, $\hat{\sigma}$. A Sudakov suppression as in point (b) above, for the evolution between the virtuality of the active parton and the scale of the hard sub-collision, could in principle be included in either the distribution functions or in $\hat{\sigma}$. It is, however, not normally included in calculations of $\hat{\sigma}$, and it is therefore more natural to include it in the distribution functions. In the LDC formalism, the relevant scale should then correspond to a limiting angle given by the final state partons in the hard collision. It is easy to show that using the parton (colour-) connected to the incoming one implies

$$\overline{q}^2 = \frac{\hat{t}\hat{s}}{\hat{u}} \tag{3.20}$$

where $\hat{t}$, $\hat{s}$, and $\hat{u}$ are the Mandelstam variables for the sub-collision. Thus if $\hat{s}$ is large compared to $\hat{t}$ we find $\overline{q}^2 \approx -\hat{t}$. For a very hard collision we find $\overline{q}^2$ of the same order as $\hat{s}$. In the CCFM formalism this choice would according to point (a) above exclude contributions with softer emissions in between the two partons produced in the hard collision (and somewhat underestimate the result). An alternative choice would be $\overline{q}^2 = \hat{s}$, which corresponds to a limiting angle equal to 90° in the rest frame of the hard sub-collision. This would then include a Sudakov suppression between $\hat{t}$ and $\hat{s}$, and thus possibly give a slight underestimate. This may, however, not be a very big problem. The important point is that the scale $\overline{q}$ should be determined by the scales in the hard sub-collision, which normally are substantially larger than $k_\perp$. As we will see in the following section, in the range $\overline{q} \sim 2k_\perp$ the variation with $\overline{q}$ is not dramatic, and actually it turns out that here the different schemes will give rather similar results.

Many other schemes are presented in the literature to treat unintegrated parton distributions. Besides with the CCFM formalism in the CASCADE and

SMALLX MCs, which in the following will be referred to as JS (Jung and Salam) [29], we compare in the following section our results also with the formalisms presented by Kwiecinski, Martin, and Stasto (KMS) [30] and by Kimber, Martin, and Ryskin (KMR) [31]. In KMS a term describing leading order DGLAP evolution is added to the BFKL equation. The parton distribution is described by a single scale, $k_\perp$, and is assumed to satisfy the relation in eq. (3.17). In KMR two-scale parton distributions are extracted from the same unified DGLAP-BFKL evolution equation, but the angular constraint is imposed on the last link in the chain. As the value of $\overline{q}$ only puts a limit on the last emission, the dependence on $\overline{q}$ is significantly weaker than in the CCFM model. Finally we will compare to a simple derivative, according to eq. (3.17), of the integrated gluon density from the GRV98 [32] parameterization, referred to as dGRV in the following.

3.4 Results

In this section we discuss some results obtained from LDCMC. To illuminate the effect of the different contributions we study the following three different versions:

1. *Standard*: Including non-leading contributions from quarks and non-singular terms in the splitting functions.
2. *Gluonic*: Including non-singular terms in the splitting functions, but no quark links in the evolution.
3. *Leading*: Also purely gluonic chains, but with only the singular terms in the gluon splitting function.

To get realistic results from these three versions we now also need to consider the convolution of non-perturbative input parton densities. These are not à priori known, but need to be parameterized in some way. We will use the same parameterization as in [14] given by

$$xf_i(x, k_{\perp 0}^2) = A_i x^{a_i} (1-x)^{b_i}, \tag{3.21}$$

where $i = d_v, u_v, g$ and s for the d-valence, u-valence, gluon and sea-quark densities respectively (where the sea flavour densities are assumed to be $f_{\bar{d}} = f_{\bar{u}} = 2f_{\bar{s}}$). The parameters A_i, a_i, b_i and the perturbative cutoff, $k_{\perp 0}$, are then fitted to reproduce the measured data on F_2. There are some sum rules which fix the relationship between some of the parameters. The A_{d_v} and A_{u_v} are fixed by flavour conservation and A_s is fixed by momentum conservation. The fits to F_2 do not constrain the remaining parameters very strongly, so we have fixed the b parameters to 3 in the valence densities and to 4 in the sea and gluon

fit	A_g	a_g	b_g	a_d	b_d	a_u	b_u	a_s	b_s	$k_{\perp 0}$	$\int xg(x)$	χ^2/d.o.f.
standard	1.86	**0**	**4**	1.78	**3**	0.57	**3**	**0**	**4**	0.99	*0.37*	694/625
gluonic	2.71	**0**	**4**							1.80	*0.54*	193/86
gluonic-2	3.11	**0**	**7**							2.17	*0.39*	125/86
leading	2.34	**0**	**4**							1.95	*0.47*	126/86

Table 3.1: The result of the fit of the parameters for the input parton densities. The *standard* version has been fitted to data from H1 [33], ZEUS [34], NMC [35] and E665 [36] in the region $x < 0.3$, $Q^2 > 1.5$ GeV^2, while the *gluonic* and *leading* have been fitted to H1 data only, in the region $x > 0.013$ and $Q^2 > 3.5$ GeV^2. The last two columns give the resulting fraction of the proton momentum carried by the gluons and the χ^2 over the number of fitted data points, respectively. Parameters in bold face have not been fitted.

densities. We have also chosen to fix $a_g = a_s = 0$. To check the sensitivity to the b parameter we have an additional fit for the *gluonic* case with $b = 7$ called *gluonic-2*. In table 4.1 we present the result of the fits. Note that in the case of the *gluonic* and *leading* versions, only the gluon input density is considered.

In figure 3.3 we show the resulting reproduction of F_2 data. Clearly, all versions give a satisfactory fit to the data. The *standard* version gives an excellent description for all values of x. The *gluonic* and *leading* versions are naturally unable to fit the large-x data, as the inclusion of quark-initiated chains is essential for a description of large x-values. These versions are therefore only fitted to the small-x H1 data, and these fits are shown separately in figure 3.3b. We note that *gluonic-2* gives a better fit than *gluonic*, but we will anyway in the following concentrate on the latter, to make the comparison with the JS results (which also uses $b_g = 4$) more informative.

It should be noted that the version of LDCMC used here has not been released yet, and differs somewhat from the one described in [14]. The main difference is the handling of the Sudakov form factors, which were not quite correct in the original version. Also the full off-shell $\gamma^* g^* \to q\bar{q}$ matrix element is now included[4]. These, and other minor changes, do not give a big effect on the results.

In the following subsections we discuss the corresponding results for the integrated and the unintegrated gluon distribution functions. As we will see, the results are very similar for the *standard* and the *gluonic* version. The differences in the cascade can here be compensated by the adjustment of the input distribution functions and the perturbative cutoff, $k_{\perp 0}$. For the *leading* version, without the non-singular terms in the splitting function, we find, however, that the resulting differences are small but not negligible.

[4]Note, however, that the matrix element in [37] is used, rather than the one from [38] used in SMALLX and CASCADE

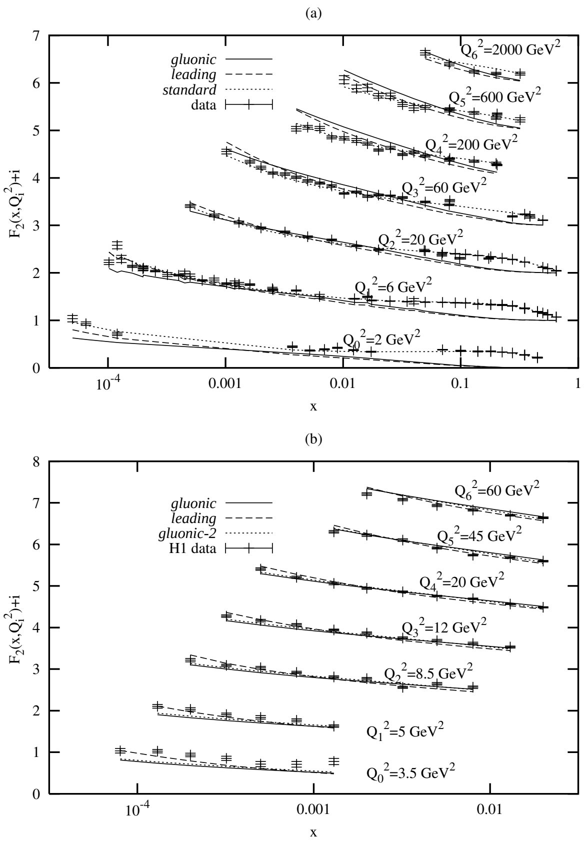

Figure 3.3: The description of F_2 data as a function of x for the different fits presented in this paper. To separate the results for different Q^2, what is shown is $F_2 + i$ for Q_i^2. In (a) both small and large x data from H1, ZEUS [34], NMC [35] and E665 [36] are included. The full line is *gluonic*, dashed is *leading* and the dotted line is *standard*. In (b) the versions with only gluonic chains are compared to small-x H1 data [33]. As in (a), full line is the *gluonic* case, dashed is *leading*, whereas dotted is *gluonic-2* (with b_g=7).

3.4.1 Results for the Integrated Gluon Distribution Function

We start by studying the results obtained for the integrated gluon distribution function. As mentioned in section 4.3 (cf. eq. (3.16)), in the LDC model the relation between the integrated and the unintegrated gluon distribution functions is as follows:

$$\begin{aligned} xg(x,Q^2) &= \int_{k_{\perp 0}^2}^{Q^2} \frac{\mathrm{d}k_\perp^2}{k_\perp^2}\mathcal{G}(x,k_\perp^2,Q) + \int_{Q^2}^{Q^2/x} \frac{\mathrm{d}k_\perp^2}{k_\perp^2}\mathcal{G}(x\frac{k_\perp^2}{Q^2},k_\perp^2,Q)\frac{Q^2}{k_\perp^2} + \\ & \quad xg_0(x,Q_0^2) \times \Delta_\mathrm{S}. \end{aligned} \tag{3.22}$$

Thus, the integrated distribution function receives contributions from three different terms. The first term corresponds to struck gluons of transverse momenta below the virtuality of the probe, $k_\perp^2 < Q^2$ (the full line in the triangular phase space of figure 3.4 is an example of such a chain), while the second term originates from chains whose struck gluons have $k_\perp^2 > Q^2$ (e.g. the long-dashed line in figure 3.4). Finally, the third term is the contribution from the input distribution function, corresponding to the case when no evolution has taken place.

As discussed in sections 4.3 and 3.3, the distribution function $\mathcal{G}(x,k_\perp^2,Q)$ in the LDC model depends only very weakly upon the scale Q. This dependence is due to the Sudakov form factor corresponding mainly to the $1/(1-z)$ term in the splitting function. Although this dependence is weak and can essentially be neglected in the first two terms in eq. (3.22), it has a larger effect on the last term, where it is explicitely included as a multiplicative factor. This term

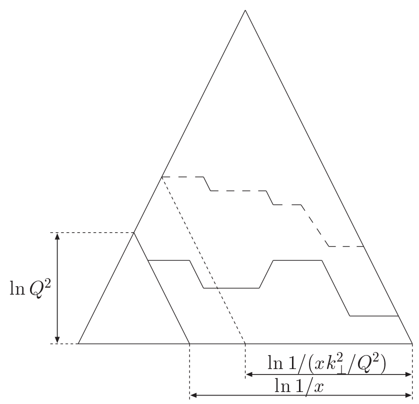

Figure 3.4: The hard colour-neutral probe Q^2 probes the gluon. The continuous line and the long-dashed line chains correspond to a struck gluon of $k_\perp^2 < Q^2$ and $k_\perp^2 > Q^2$, respectively.

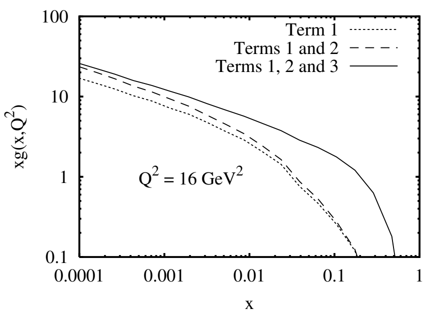

Figure 3.5: Relative importance of the different terms contributing to the LDC integrated gluon distribution function, for fixed $Q^2 = 16$ GeV^2. The dotted curve corresponds to keeping only the first term in eq. (3.22); keeping the first and second terms we obtain the dashed curve. The total result is represented by the full curve.

dominates at large x, and the effect of the form factor is a suppression for larger values of Q^2.

We first study the relative importance of the different terms contributing to the LDC integrated gluon distribution function. In figure 3.5 the integrated gluon distribution function is shown as a function of x, for fixed $Q^2 = 16$ GeV^2. As can be seen, at small x-values the first term of eq. (3.22) dominates; as x decreases the second term becomes noticeable. At large x-values, the behavior is governed by the input distribution function.

Next we compare the LDC results with those obtained by other analyses. In figure 3.6 we show the LDC integrated gluon distribution function as a function of x for $Q^2 = 16$ GeV^2 and $Q^2 = 100$ GeV^2. We show our result for the *gluonic* together with the *gluonic-2* case. As discussed above, they both give a good fit to F_2. We see that the LDCMC results lie significantly below the JS curve for large x, but above JS for smaller x-values. Also shown in figure 3.6 are the corresponding results for CTEQ5M1 [39] and MRST20011 [40]. An important point is that, while the LDC and JS results have been fitted to F_2 data only, the CTEQ and MRST curves have been fitted to more data. We see that these latter curves are more or less in agreement at large x, where there is more data available, while they separate more for smaller x-values. Clearly the LDC result agrees well with these curves for small x, where it almost coincides with CTEQ5M1. For larger x the LDC curve lies above CTEQ and MRST for *gluonic*, but agrees well with them for *gluonic-2*.

This comparison leads to increased confidence in the physical relevance of the LDC model in general and in the LDC unintegrated gluon distribution

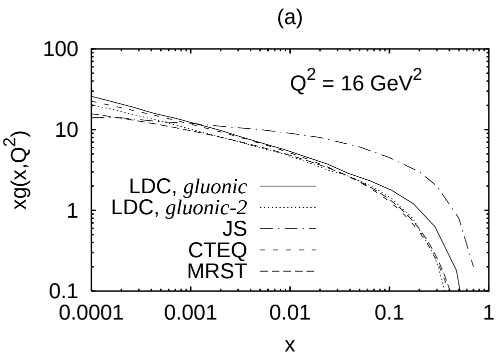

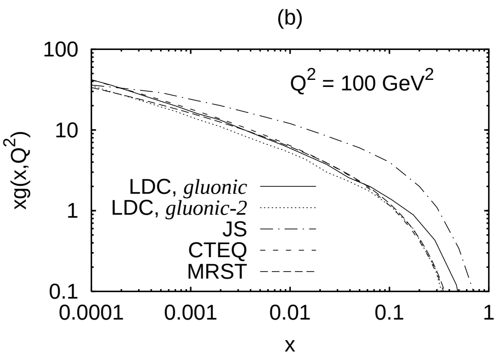

Figure 3.6: The LDC integrated gluon distribution function (full curve is *gluonic*, dotted curve is *gluonic-2*), compared to the corresponding results of JS (dash-dotted curve), CTEQ (short-dashed curve) and MRST (long-dashed curve), for (a) $Q^2 = 16$ GeV^2 and (b) $Q^2 = 100$ GeV^2

function in particular. We shall study this in the next subsection.

3.4.2 Results for the Unintegrated Gluon Distribution Function

We now turn our attention to the topic of unintegrated gluon distribution functions, and we first want to study the effects from sub-leading corrections caused by the inclusion of quarks and by the inclusion of the non-singular terms in the gluon splitting function, in order to verify the statements made earlier in this section.

In figure 3.7 the unintegrated LDC gluon distribution function is shown both as a function of x and $k_\perp^2$. Comparing the result for the purely gluonic

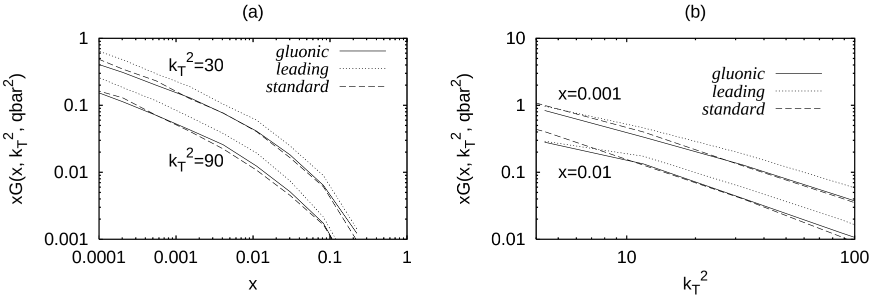

Figure 3.7: The LDC unintegrated gluon distribution function as a function of (a)x and (b) $k_\perp^2$. Study of sub-leading effects caused by inclusion of quarks and non-singular terms in the gluon splitting function. Full line is *gluonic*, dotted line is *leading* and dashed line is *standard*. (In these figures $\overline{q}$ is put equal to $k_\perp$.)

case to that when we allow for quarks as well, we see that the differences are very small. (Note that the input distribution functions have been refitted.)

Even though the effect of omitting the non-singular terms in the gluon splitting function is rather small, it is nevertheless not completely negligible: as can be seen in figure 3.7a, at small x there is a discrepancy of about a factor of two, a result that is related to the problem with the description of H1 forward-jet data that was mentioned in Section 4.2.

Our conclusion is that the non-leading effects can be largely compensated by slight modifications of the input distribution functions; we note in particular that the results with and without quark links are almost identical.

We note that there is a slight drop in the *gluonic* and *leading* curves for small $k_\perp^2$ in figure 3.7b (this is also visible in some of the following figures). This is due to the rather high cutoff used for these fits and because the input distribution is treated as a delta function at $k_\perp = 0$. In the JS, KMR and KMS approaches, the input gluon is added with a Gaussian distribution in $k_\perp$.

We now want to study the dependence upon the two different scales discussed in section 3.3. We show in figure 3.8 the dependence on $\overline{q}$ for fixed $k_\perp$ for the LDC, CCFM, and KMR formalisms. As discussed in section 3.3, the $\overline{q}$-dependence is relatively weak in the LDC model, but very strong in the CCFM approach. We also see that the result in the KMR formalism is quite insensitive to variations in $\overline{q}$, and rather similar to the LDC results. This is also illustrated in figure 3.9, which shows the results as functions of $k_\perp^2$ for fixed $\overline{q} = 10$ GeV. We see that the JS results start to fall dramatically below the other two, as $k_\perp$ approaches $\overline{q}$.

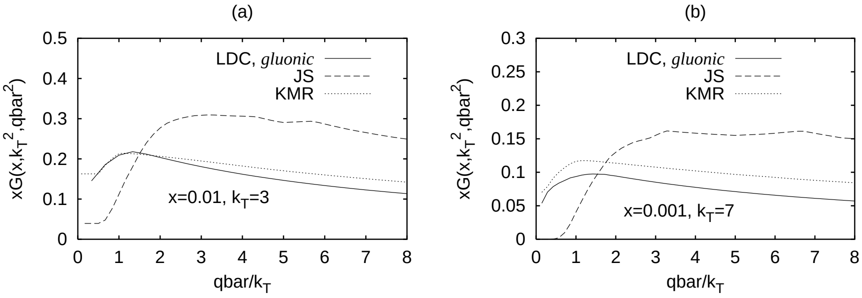

Figure 3.8: The LDC *gluonic* unintegrated gluon distribution function (full curve), compared to the corresponding results of JS (long-dashed curve) and KMR (dotted curve), as functions of $\overline{q}/k_\perp$ for (a) $x = 0.01$ and $k_\perp = 3$ GeV and (b) $x = 0.001$ and $k_\perp = 7$ GeV.

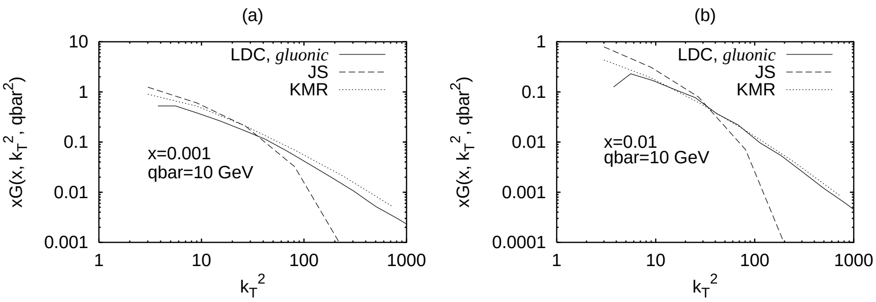

Figure 3.9: The LDC *gluonic* unintegrated gluon distribution function (full curve), compared to the corresponding results of JS (long-dashed curve) and KMR (dotted curve), as functions of $k_\perp^2$ for (a) $x = 0.001$ and (b) $x = 0.01$. (In these figures $\overline{q}$ is put equal to 10 GeV.)

From figure 3.8 we note, however, that the CCFM result appears to saturate for $\overline{q} \gtrsim 2k_\perp$, before it falls off for large values of $\overline{q}/k_\perp$. In a hard-interaction event the scales $|\hat{t}|$ and $\hat{s}$ are normally larger than $k_\perp^2$, and often characteristically by a factor of this order. For this reason we want to argue that when comparing the different formalisms, it is more relevant to study the CCFM distributions for $\overline{q}$ equal to the saturation value, rather than e.g. for $\overline{q} = k_\perp$. Indeed, for this larger $\overline{q}$-value we see in figure 3.8 that there is a rather good agreement between the three models.

This feature is further illustrated in figure 3.10, which shows the distribution functions for $\overline{q} = 2k_\perp$, as a functions of $k_\perp^2$ for fixed x and as a functions x for fixed $k_\perp^2$, and we see indeed a reasonable agreement between the LDC, JS, and KMR results, even if the JS result for $k_\perp^2 = 10$ GeV^2 lies somewhat above the other two for large x and below for smaller x-values. In these figures we also show the single scale KMS and dGRV results. Although these earlier parameterizations are somewhat lower for larger x-values, we note a fair overall agreement between all five models.

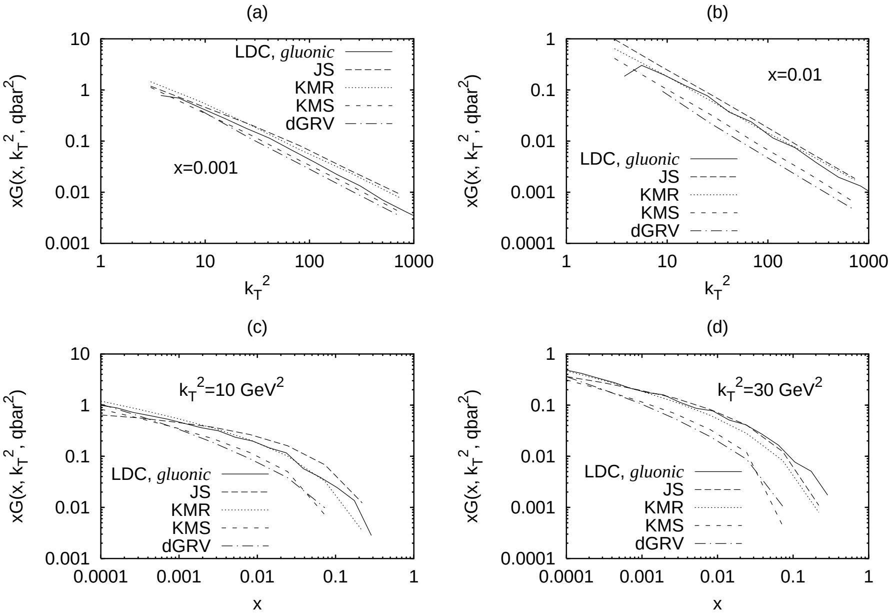

Figure 3.10: The LDC *gluonic* unintegrated gluon distribution function (full curve), compared to the corresponding results of JS (long-dashed curve), KMR (dotted curve), KMS (short-dashed curve) and dGRV (dash-dotted curve) as functions of $k_\perp^2$ for (a) $x = 0.001$ and (b) $x = 0.01$, and as functions of x for (c) $k_\perp^2 = 10$ GeV^2 and (d) $k_\perp^2 = 30$ GeV^2. Results for LDC, JS and KMR, with $\overline{q} = 2k_\perp$, are shown together with the 1-scaled distribution functions of KMS and dGRV.

3.5 Summary

Unintegrated parton distribution functions are not uniquely defined. They are not experimental observables, and their definition and properties depend critically on the formalism used. Thus when calculating e.g. cross-sections for production of jets or heavy quarks it is necessary to use a consistent formalism for off-shell parton cross-sections and parton distribution functions.

In this paper we present results for integrated and unintegrated gluon distribution functions according to the definitions in the Linked Dipole Chain model, obtained from the LDCMC program. We compare them with those obtained in other formalisms, in particular with results from the CCFM model obtained from the SMALLX and CASCADE MCs, and we demonstrate how to make a relevant comparison between the models. Indeed we find in this way a reasonable agreement between distributions obtained in different formalisms.

Adjusting the input distribution functions for $k_\perp = k_{\perp 0}$, it is possible to find a good fit to the structure function F_2 from LDCMC. The corresponding integrated gluon distribution function agrees well with fits to more complete data sets obtained by the CTEQ or MRST collaborations. The result is rather insensitive to non-singular contributions in the gluon splitting function or from quark links in the chain. The contributions from quarks can be almost fully compensated by adjusting the input distribution functions. Omitting the non-singular terms in the gluon splitting function has a somewhat larger effect, reducing the gluon distribution for small x by roughly a factor 2.

In the CCFM formalism the unintegrated parton distribution functions depend sensitively on two different scales: $k_\perp$, which specifies the transverse momentum and the virtuality of the interacting parton, and $\overline{q}$, which determines an angle beyond which there is no (quasi-)real parton in the chain of initial-state radiation. Many of the gluons which make up the initial-radiation chain in the CCFM model are treated as final-state radiation in the LDC formalism. Therefore typical z-values are smaller in LDC, and most of the problem of angular ordering is postponed to the treatment of the final-state radiation. This implies that in the LDC formalism the gluon distribution function is much less sensitive to the second scale $\overline{q}$, and to leading $\log 1/x$ it depends only on a single scale $k_\perp$.

In a typical hard sub-collision the relevant additional scale $\overline{q}$ should be given by $\overline{q}^2 \sim |\hat{t}|$ or $\hat{s}$. We observe that in the CCFM formalism, for a fixed $k_\perp$, the gluon distribution function saturates for $\overline{q} \gtrsim 2k_\perp$, before it falls off for larger $\overline{q}$-values. This corresponds to typical values of $\hat{t}$ or $\hat{s}$, and we therefore suggest that for a relevant comparison between the different formalisms we should choose $\overline{q}$ in this saturation region. Here we find indeed a reasonable agreement, not only between LDC and CCFM, but also with e.g. the two-scale formalism presented by Kimber, Martin and Ryskin, and the one-scale formalism by Kwiecinski, Martin and Sutton. Actually we see that it also agrees rather well with the derivative of the integrated distribution function GRV98, obtained in the pure DGLAP formalism.

Acknowledgments

We want to thank Hannes Jung for valuable discussions, and in particular for help in evaluating the distribution functions for the JS, KMS, and KMR models.

References

[1] V. N. Gribov and L. N. Lipatov *Yad. Fiz.* **15** (1972) 781–807.

[2] L. N. Lipatov *Sov. J. Nucl. Phys.* **20** (1975) 94–102.

[3] G. Altarelli and G. Parisi *Nucl. Phys.* **B126** (1977) 298.

[4] Y. L. Dokshitzer *Sov. Phys. JETP* **46** (1977) 641–653.

[5] **Small x** Collaboration, B. Andersson *et al.* `hep-ph/0204115`.

[6] E. A. Kuraev, L. N. Lipatov, and V. S. Fadin *Sov. Phys. JETP* **45** (1977) 199–204.

[7] I. I. Balitsky and L. N. Lipatov *Sov. J. Nucl. Phys.* **28** (1978) 822–829.

[8] M. Ciafaloni *Nucl. Phys.* **B296** (1988) 49.

[9] S. Catani, F. Fiorani, and G. Marchesini *Phys. Lett.* **B234** (1990) 339.

[10] B. Andersson, G. Gustafson, and J. Samuelsson *Nucl. Phys.* **B467** (1996) 443–478.

[11] B. Andersson, G. Gustafson, and H. Kharraziha *Phys. Rev.* **D57** (1998) 5543–5554, `hep-ph/9711403`.

[12] G. P. Salam *JHEP* **03** (1999) 009, `hep-ph/9902324`.

[13] G. Marchesini *Nucl. Phys.* **B445** (1995) 49–80, `hep-ph/9412327`.

[14] H. Kharraziha and L. Lönnblad *JHEP* **03** (1998) 006, `hep-ph/9709424`.

[15] M. Ciafaloni and G. Camici *Phys. Lett.* **B430** (1998) 349–354, `hep-ph/9803389`.

[16] V. S. Fadin and L. N. Lipatov *Phys. Lett.* **B429** (1998) 127–134, `hep-ph/9802290`.

[17] Y. L. Dokshitzer, V. A. Khoze, A. H. Mueller, and S. I. Troyan, *Basics of perturbative QCD.* Ed. Frontieres, Gif-sur-Yvette, France (1991), 1991.

[18] E. M. Levin and M. G. Ryskin *Phys. Rept.* **189** (1990) 267–382.

[19] J. Bartels and H. Lotter *Phys. Lett.* **B309** (1993) 400–408.

[20] J. R. Forshaw, P. N. Harriman, and P. J. Sutton *Nucl. Phys.* **B416** (1994) 739–750.

[21] J. Kwiecinski, A. D. Martin, and P. J. Sutton *Z. Phys.* **C71** (1996) 585–594, `hep-ph/9602320`.

[22] G. Marchesini and B. R. Webber *Nucl. Phys.* **B349** (1991) 617–634.

[23] G. Marchesini and B. R. Webber *Nucl. Phys.* **B386** (1992) 215–235.

[24] H. Jung *Comput. Phys. Commun.* **143** (2002) 100–111, `hep-ph/0109102`.

[25] Hamid Kharraziha. private communication.

[26] G. Gustafson and G. Miu *Phys. Rev.* **D63** (2001) 034004, `hep-ph/0002278`.

[27] G. Gustafson, L. Lönnblad, and G. Miu. Preprint in preparation.

[28] Discussions with Y.L. Dokshitzer et al., "Lund workshop on small-x evolution." Lund, June 2002. To be published in the proceedings.

[29] H. Jung and G. P. Salam *Eur. Phys. J.* **C19** (2001) 351–360, `hep-ph/0012143`.

[30] J. Kwiecinski, A. D. Martin, and A. M. Stasto *Phys. Rev.* **D56** (1997) 3991–4006, `hep-ph/9703445`.

[31] M. A. Kimber, A. D. Martin, and M. G. Ryskin *Phys. Rev.* **D63** (2001) 114027, `hep-ph/0101348`.

[32] M. Glück, E. Reya, and A. Vogt *Eur. Phys. J.* **C5** (1998) 461–470, `hep-ph/9806404`.

[33] **H1** Collaboration, S. Aid *et al. Nucl. Phys.* **B470** (1996) 3–40, `hep-ex/9603004`.

[34] **ZEUS** Collaboration, M. Derrick *et al. Z. Phys.* **C72** (1996) 399–424, `hep-ex/9607002`.

[35] **New Muon** Collaboration, M. Arneodo *et al. Phys. Lett.* **B364** (1995) 107–115, `hep-ph/9509406`.

[36] **E665** Collaboration, M. R. Adams *et al. Phys. Rev.* **D54** (1996) 3006–3056.

[37] V. N. Baier, E. A. Kuraev, V. S. Fadin, and V. A. Khoze *Phys. Rept.* **78** (1981) 293–393.

[38] S. Catani, M. Ciafaloni, and F. Hautmann *Nucl. Phys.* **B366** (1991) 135–188.

[39] **CTEQ** Collaboration, H. L. Lai *et al. Eur. Phys. J.* **C12** (2000) 375–392, `hep-ph/9903282`.

[40] A. D. Martin, R. G. Roberts, W. J. Stirling, and R. S. Thorne *Eur. Phys. J.* **C23** (2002) 73–87, `hep-ph/0110215`.

Hadronic Collisions in the Linked Dipole Chain Model

Paper IV

Hadronic Collisions in the Linked Dipole Chain Model

Gösta Gustafson, Leif Lönnblad and Gabriela Miu

Department of Theoretical Physics
Lund University, Sölvegatan 14A, S-223 62 Lund, Sweden

hep-ph/0209186

Abstract

We apply the Linked Dipole Chain model to hadronic collisions using a modified version of the LDCMC Monte Carlo program. In particular we investigate the effects of multiple scatterings, which in this framework are reformulated in terms of the production of multiple chains of dipoles. We find, among other things, that this way of describing multiple scatterings is less sensitive to the treatment of soft, non-perturbative, scatterings.

Although the results presented here are only at parton level, by comparing with corresponding results from PYTHIA, we are confident that our model will be able to describe essential features of high energy hadronic collisions, including underlying events and jet-pedestal effects in high $p_\perp$ events. The model should also be applicable to estimates of transverse energy flow in high energy heavy ion collisions, of interest in analyses of signals for quark-gluon plasma formation.

4.1 Introduction

Although the main aim for the future Large Hadron Collider at CERN is to discover and study the Higgs boson, and to possibly discover new physics, it is important to keep in mind that our understanding of the strong interactions, which make up the bulk of the cross section in hadronic collisions, is far from complete. The hard production of large transverse momentum jets may be described to a reasonable precision by perturbative QCD, but for the dominating soft and semi-hard interactions we have to rely on phenomenological models. There may be some gold-plated signals for new physics, where these so-called minimum bias interactions may be disregarded, but as soon as observables include jets, a more detailed understanding of the event structure is needed. Not only is the luminosity so high at the LHC that any signal event will be accompanied by several overlayed minimum bias collisions. In addition the inclusive cross section for parton-parton scatterings becomes larger than the total non-diffractive cross section already at present day energies, which implies that there are several parton-parton scatterings in each single hadron-hadron collision. Such additional scatterings can be rather soft, and can therefore not be described by purely perturbative calculations. The production of minijets is also of interest in high energy heavy ion collisions, and the analysis of signals for plasma formation. They are essential for the initial conditions in studies of the flow in either a quark-gluon plasma or a hadronic phase [1].

Further studies of hadronic collisions are also interesting in its own right, in order to understand the nature of strong interaction and the interplay between soft and hard physics. Many models have been presented to describe and simulate hadronic collisions. The Fritiof model [2] successfully describes hadron collisions at lower energies, up to the ISR range. It is based on a soft momentum transfer and gluon bremsstrahlung due to the separation of colour charges. These charges are in the model connected by strings of the same nature as in e^+e^--annihilation. For higher energies hard sub-collisions were added [3]. The formalism did, however, not give a unique description for how to combine the soft and hard subprocesses, and therefore the predictive power at high energies is reduced.

The Dual Parton Model (DPM) [4, 5] aims at a combined description of soft and hard interactions in an eikonalized form, including besides a soft and a hard pomeron also triple- and loop-pomeron contributions. The aim is to describe not only non-diffractive events, but also elastic scattering and single and double diffraction, and the model is able to reproduce a large set of experimental data [6].

At high energies, in the $\bar{p}p$ collider regime, the cross section for hard or semi-hard parton sub-collisions becomes large, and the properties of non-diffractive events appear to be dominated by these subprocesses. In this energy range it is therefore essential to have a good description of jets from hard parton collisions, including initial and final state bremsstrahlung. In ISAJET [7] and HERWIG [8] a description of the hard sub-collisions is complemented by an "underlying event" due to interactions between the beam remnants. In PYTHIA [9] this underlying event is modeled by including multiple parton interactions in the generation of the hard parton collision, rather than adding them as an independent component to the hard sub-collisions.

Even if the parton-parton collisions are of perturbative nature, with a $p_\perp$ above a couple of GeV, there are many difficulties, which cannot be solved by perturbative methods alone. The parton sub-collisions are typically modeled using collinear factorization. This gives a divergent expression for the inclusive cross section at small $p_\perp$, which has to be treated by some kind of cut-off. Clearly collisions with large impact parameter must be suppressed due to screening effects, when the impact parameter is larger than the proton radius. The impact parameter dependence is also expected to influence the correlations between sub-collisions in a single event. It is natural to assume that central collisions have a higher activity than more peripheral collisions and therefore, on average, a larger number of sub-collisions [10]. Both these effects, the $p_\perp$ cutoff and the multiplicity correlations, have to be adjusted to experimental data, which makes it more difficult to make reliable extrapolations to higher energies.

In collinear factorization the hard partonic cross section is convoluted with parton densities, which are evolved using DGLAP [11, 12, 13, 14] evolution. The parton densities are fitted to data on e.g. F_2 in DIS and high $E_\perp$ jets in hadronic collisions. For moderate $p_\perp$ at very large c.m. energies, $\sqrt{s}$, the parton evolution contains large logarithms of $s/p_\perp^2$ which need to be resummed to all orders. For these $p_\perp$values it would therefore be more appropriate to use BFKL evolution [15, 16], which gives the correct description, at least for asymptotic energies and fixed coupling. The BFKL evolution is related to $k_\perp$-factorization, and in ref. [17] it is argued that this approach gives a dynamical suppression for small $p_\perp$, which reduces the infrared sensitivity. This is mainly a consequence of a suppression of the partonic cross section when the virtualities of the colliding partons are larger than the transverse momentum exchanged in the hard collision.

The study in ref. [17] is based on the Linked Dipole Chain (LDC) model [18, 19] for DIS. This model is based on the observation that the dominant features of the parton evolution is determined by a subset of emitted gluons, which are ordered in both positive and negative light-cone components. These *primary* gluons make up a linked chain of colour dipoles, and the sum over all such possible chains, convoluted with non-perturbative input parton densities, will give the proton structure function. (For exclusive properties of the final states also final state radiation has to be included.) The LDC model is completely forward-backward symmetric – i.e. it does not matter if the evolution is performed from the proton towards the virtual photon or vice versa. This means that LDC is also very suited for a description of hadronic collisions, where the sum over all possible chains, convoluted with input parton densities from both hadrons, will give the inclusive partonic cross section. The fact that transverse momenta can go up and down in a single parton chain implies that such a chain can correspond to more than one hard parton-parton sub-collision. Thus one type of correlations between the sub-collisions is automatically included in the LDC formalism. However, even so the *per chain* cross section exceeds the total non-diffractive cross section. Therefore there will in general be several dipole chains stretched between two colliding hadrons, and it is also in this approach necessary to make assumptions about the impact parameter dependence, now for the distribution in the number of chains in one event.

In this paper we will investigate the effects of such multiple chains in more detail, using the LDC event generator LDCMC [20], modified to generate hadronic collisions. The investigation will still be on a somewhat qualitative level since effects of colour connection between the chains, and of hadronization are not included. Therefore we will here compare our results with the PYTHIA generator on parton level rather than with experimental data.

A very essential result from these MC studies is the fact that the number of chains per event is stable against variations of the $p_\perp$ cutoff in the perturbative parton evolution. When fitting experimental data on F_2, the input soft gluon distribution is adjusted, and corresponds to a scale given by the cutoff. The soft input gluons can also form direct chains between the colliding hadrons, and these chains are also allowed to emit final state bremsstrahlung below the cutoff. If the soft cutoff is increased there will be fewer hard chains, which is compensated by a more singular input gluon distribution. As we will show below, when the cutoff is increased, the decrease in the number of hard chains is compensated by a larger number of soft chains (which are now also allowed to radiate more). Thus the total number of chains in pp collisions can be fully determined by data on F_2, without any additional adjustable free parameter.

The outline of this paper is as follows. In section 4.2 we give some further comments on parton evolution in DIS, including a brief introduction to the LDC model. In section 4.3 we discuss the application of the LDC model for hadronic collisions. Then in section 4.4 we discuss some general aspects of multiple scatterings, in particular how they are included in the PYTHIA generator and how we treat them in the present analysis. The technical details of the Monte-Carlo implementation are discussed in section 4.5. In section 4.6 we present some preliminary results, followed by conclusions in section 4.7.

4.2 Small-x physics in DIS

Effects of BFKL evolution have been studied extensively at HERA, where BFKL predicted a strong power-like increase of F_2 for small x. It turns out, however, that BFKL suffers from huge next-to-leading order corrections [21] and it has been very difficult to obtain reliable predictions, especially when it comes to non-inclusive observables involving final-state hadrons. More reliable predictions for final-state observables can be obtained using CCFM evolution [22, 23], which agrees with BFKL in the asymptotic limit, but also approximates DGLAP for large x. The central feature of the CCFM model is the angular ordering of the parton chains contributing to the proton structure function, which is a consequence of colour coherence or soft gluon interaction. The parton chains are ordered in energy (or positive light-cone momentum q_+) and in angle (or rapidity $y = \frac{1}{2}\ln(q_+/q_-)$). (We use q_i and k_i to denote the real emitted partons and the virtual links respectively, as indicated in figure 4.1.) Other kinematically allowed emissions (symbolized by the dashed lines in figure 4.1) are treated as final-state emissions.

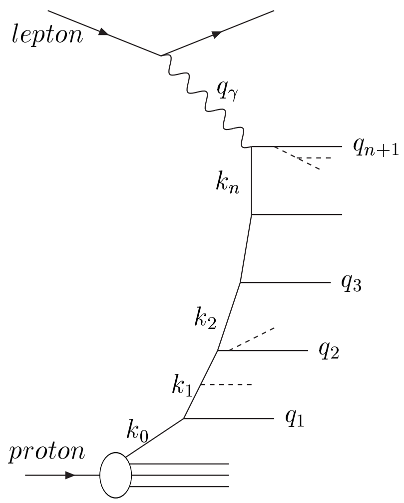

Figure 4.1: A fan diagram for a DIS event. The quasi-real partons from the initial-state radiation are denoted q_i, and the virtual propagators k_i. The dashed lines denote final-state radiation.

4.2.1 CCFM Evolution

Like BFKL evolution, the CCFM model is based on the $k_\perp$-factorization formalism, and the unintegrated distribution function is given by

$$\begin{aligned}\mathcal{G}(x,k_\perp^2,\overline{q}) \quad \sim \quad & \sum_n \int \prod^n \bar{\alpha} dz_i \frac{d^2 q_{\perp i}}{\pi q_{\perp i}^2} \left(\frac{1}{z_i} \Delta_{ne}(z_i, k_{\perp i}^2, \overline{q}_i) + \frac{1}{1-z_i} \right) \Delta_S \times \\ & \delta(x - \Pi z_i)\theta(\overline{q}_i - \overline{q}_{i-1} z_{i-1})\delta(k_\perp^2 - k_{\perp n}^2)\theta(\overline{q} - \overline{q}_n z_n) \end{aligned} \quad (4.1)$$

where the non-eikonal and the Sudakov form factors are given by

$$\Delta_{ne} = \exp\left(-\bar{\alpha} \ln \frac{1}{z} \ln \frac{k_\perp^2}{z\bar{q}^2}\right); \quad \Delta_S = \exp\left(-\bar{\alpha} \int \frac{dq_{\perp i}^2}{q_{\perp i}^2} \frac{dz}{1-z} \Theta_{order}\right) \quad (4.2)$$

Here $\bar{\alpha} \equiv 3\alpha_s/\pi$, the splitting parameter z is defined as $z_i = k_{+,i}/k_{+,i-1}$, and the kinematic range allowed by the ordering constraints is specified by Θ_{order}. The quantity $\overline{q}_i$ is defined by $\overline{q}_i \equiv q_{\perp i}/(1-z_i)$, which implies that the angular ordering condition is satisfied by the constraint $\overline{q}_i > \overline{q}_{i-1} z_{i-1}$, accounted for by a θ-function in eq. (4.1). The CCFM model has been developed assuming purely gluonic chains, and only the singular terms in the splitting functions, proportional to $1/z$ and $1/(1-z)$, are included in a fully consistent way. The $1/z$ pole is most important in the BFKL region for small x, while the $1/(1-z)$ pole and the Sudakov form factor are essential for larger x and large $k_\perp$. We also note that the distribution function, $\mathcal{G}$, depends on two separate scales. Besides the transverse momentum, $k_\perp$, of the interacting gluon, it also depends on $\overline{q}$, which determines an angle beyond which there is no (quasi-) real parton in the chain.

A Monte Carlo implementation of CCFM, CASCADE [24], reproduces a wide range of final-state observables at HERA, although there are still some unsolved questions. Since CCFM does not include the non-singular terms in the gluon splitting function, DGLAP is not fully reproduced in the relevant limit, and including non-singular terms degrades the reproduction of HERA data, especially for observables which are supposed to be sensitive to BFKL effects, such as forward jet cross sections [25].

4.2.2 The Linked Dipole Chain Model

The Linked Dipole Chain (LDC) model [18, 19] is a reformulation and generalization of CCFM. It is based on the observation that the dominant features of the parton evolution is determined by a subset of emitted gluons, which are ordered in both positive and negative light-cone components, and also satisfies the relation

$$q_{\perp i} > \min(k_{\perp i}, k_{\perp, i-1}). \quad (4.3)$$

In LDC this subset of "*primary*" gluons forms a chain of initial state bremsstrahlung (ISB), and all other emissions are treated as final state bremsstrahlung (FSB).

This redefinition of the ISB–FSB separation implies that one single chain in the LDC model corresponds to a set of CCFM chains. As was shown in ref. [18], when one considers the contributions from all chains in this set, with their corresponding non-eikonal form factors, they just add up to one. Thus, the non-eikonal form factors do not appear explicitly in LDC, and the gluon distribution function is given by

$$\begin{aligned} \mathcal{G}(x, k_\perp^2) \quad \sim \quad & \sum_n \int \prod^n \bar{\alpha} dz_i \frac{d^2 q_{\perp i}}{\pi q_{\perp i}^2} P(z_i) \Delta_S \times \\ & \theta(q_{+,i-1} - q_{+i}) \theta(q_{-i} - q_{-,i-1}) \delta(x - \Pi z_i) \delta(\ln k_\perp^2 - \ln k_{\perp n}^2). \end{aligned} \tag{4.4}$$

Here $P(z)$ is the full gluonic splitting function, and Δ_S the associated Sudakov form factor, defined by

$$\Delta_S = \exp\left(-\bar{\alpha} \int \frac{dq_{\perp i}^2}{q_{\perp i}^2} z dz P(z) \Theta_{order}\right) \tag{4.5}$$

where again Θ_{order} specifies the region of phase space allowed by the ordering constraints. The result of this reformulation is a simpler form for the unintegrated distribution functions, which essentially depends only on a single scale, $k_\perp^2$. As many of the gluons which make up the initial-radiation chain in the CCFM model are treated as final state radiation in the LDC formalism, most of the problem of angular ordering is postponed to the treatment of the final state radiation. The ordering of the LDC evolution in both q_+ and q_-, and the fact that the $1/z$ pole in the splitting function is here not associated with an non-eikonal form factor, imply that this contribution is completely forward–backward symmetric. Therefore the chain in figure 4.1 can be thought of either as an evolution from the proton towards the photon or, equivalently, from the photon towards the proton end. The $1/(1-z)$ pole in $P(z)$ and the Sudakov form factor are most essential in the DGLAP region, where chains with ordered $q_\perp$ values dominate and large z-values are important. In the LDC model the expression in eq. (4.4) is symmetrized so that steps downwards in transverse momentum with large values of the backwards splitting parameter $z_{-i} = k_{-i}/k_{-,i+1}$ are weighted by the splitting function $P(z_{-i})$ and a correspondingly defined Sudakov form factor. The absence of the non-eikonal form factor also implies that quark links and non-singular terms in the splitting function can be included in a natural and straightforward way.

The set of "*primary*" gluons in eq.(4.4) make up a chain of linked colour dipoles, and the sum over all such possible chains, convoluted with non-perturbative input parton densities, will give the proton structure function. Besides this inclusive description of the events, the result in eq. (4.4) can also be interpreted as the production probability for an exclusive final state. We note, however, that due to the different separation between ISB and FSB in LDC and CCFM or other approaches, it is important to include final state emissions before comparing results for exclusive final states with results from other formalisms or with experimental data.

The LDC model is also implemented in a MC event generator, LDCMC. When the soft input parton densities are adjusted to fit data on F_2, the model is able to reproduce a wide range of HERA data [20]. The resulting integrated gluon distribution also agrees well with global fits by the CTEQ [26] and MRST [27] collaborations [28]. However, as for the CCFM Monte Carlos, the data for forward jets can only be described if non-singular terms are omitted from the gluon splitting function.

The fact that the LDC formalism is manifestly forward-backward symmetric implies that it automatically takes into account contributions from "resolved virtual photons", where the chain describes evolution from the proton and photon ends towards a central hard parton sub-collision. This property is a consequence of the specific choice of separation between initial and final state emissions adopted in the LDC model, and it means that the formalism is also very well suited to describe hard interaction in hadron-hadron collisions, as will be discussed in more detail in the following section.

4.3 The Linked Dipole Chain Model for Hadronic Collisions

As mentioned in section 4.2, to get the gluon distribution function in a proton, the perturbative chains in eq. (4.4) have to be convoluted with non-perturbative input parton densities, $g_0(x_0, k_{\perp 0}^2)$, for $k_\perp^2 = k_{\perp 0}^2$:

$$g(x, k_\perp^2) = \int dx_0 dx' \mathcal{G}(x', k_\perp^2; k_{\perp 0}^2) g_0(x_0, k_{\perp 0}^2) \delta(x_0 x' - x) \tag{4.6}$$

As we are assuming a running coupling, which diverges for small $q_\perp$, it is necessary to introduce a cutoff, $k_{\perp 0}$, for the $q_{\perp i}$ distributions in eq. (4.4) (see e.g. [19]). In eq. (4.6) this is explicitely indicated as an argument in $\mathcal{G}$. Thus $g_0(x_0, k_{\perp 0}^2)$ is assumed to describe all chains with transverse momenta below the cutoff $k_{\perp 0}$.

4.3.1 Hard Chains

The fact that $\mathcal{G}$ is completely forward-backward symmetric, as discussed in section 4.2, now implies that the cross section, σ_c, for formation of a chain

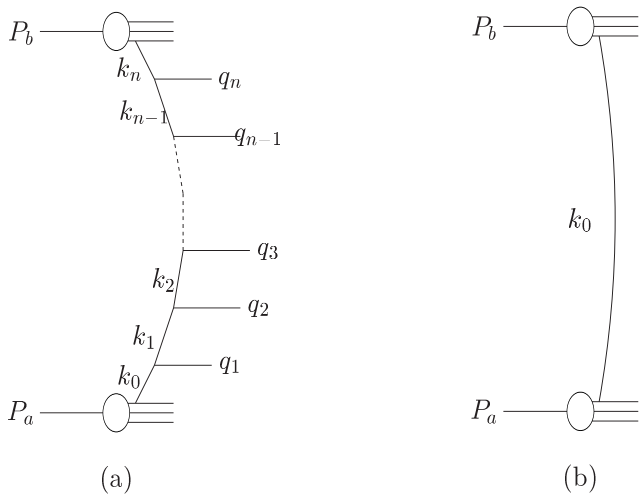

Figure 4.2: (a) A chain of n initial state emissions in a hadronic collision. (b) An exchange of a single soft gluon without initial state emissions.

between two colliding protons is directly obtained if the distribution in eq. (4.6) is convoluted with a parton distribution from the upper proton in figure 4.2. Thus we find:

$$\begin{aligned}\sigma_c &= \frac{\pi^3}{2k_{\perp 0}^2}\int dx_{0+}dx\, dx_{0-}g_0(x_{0+},k_{\perp 0}^2)\mathcal{G}(x,k_{\perp 0}^2;k_{\perp 0}^2)g_0(x_{0-},k_{\perp 0}^2)\times \\ &\quad \delta(x_{0+}x\, x_{0-}-k_{\perp 0}^2/s), \end{aligned} \tag{4.7}$$

with $x_{0+} = k_{0+}/P_{a+}$ and $x_{0-} = k_{n-}/P_{b-}$. The normalization factor $\pi^3/2$ originates from the fact that a hard scattering in the middle of the chain, with $q_{\perp i}^2 \approx k_{\perp i}^2 \approx q_{\perp,i+1}^2$, is in eq. (4.4) given a weight

$$\frac{\bar{\alpha}^2}{q_{\perp i}^2 q_{\perp,i+1}^2} \approx \frac{\bar{\alpha}^2}{\hat{t}^2} \tag{4.8}$$

where $\hat{t} \approx -k_{\perp i}^2$. This should be compared with the well-known cross section for gluon-gluon scattering, which for $\hat{s} >> |\hat{t}|$ is given by

$$\frac{9}{2\pi}\frac{\alpha_s^2}{\hat{t}^2} = \frac{\pi^3}{2}\frac{\bar{\alpha}^2}{\hat{t}^2} \tag{4.9}$$

The factor $1/k_{\perp 0}^2$ follows because $\mathcal{G}$ is defined as a density in $\ln k_{\perp}^2$, rather than in $k_{\perp}^2$.

4.3.2 Soft Chains

It should be noted that $\sigma_{\rm c}$ gives the cross section for a chain with at least one link with virtuality larger than $k_{\perp 0}^2$. There will also be chains with no perturbative emissions above this cut. (Emissions below the cut have to be added later as final state radiation.) The cross section for these soft chains, i.e. the cross section for exchanging a single (non-perturbative) gluon with virtuality $k_{\perp 0}^2$ (see figure 4.2b), is obtained by simply convoluting the two input gluon densities:

$$\sigma_{\rm c0}(k_{\perp 0}^2) = \frac{\pi^3}{2k_{\perp 0}^2} \int dx_{0+} dx_{0-} g(x_{0+}, k_{\perp 0}^2) g(x_{0-}, k_{\perp 0}^2) \delta(x_{0+}x_{0-} - k_{\perp 0}^2/s). \tag{4.10}$$

As we will see in section 4.6, if the cutoff is increased, the cross section for the perturbative chains will decrease, but the cross section for the non-perturbative chains will increase since the fitted input gluon density is then more divergent for small x. This implies that the total number of chains in pp collisions is insensitive to the cutoff $k_{\perp 0}$, and therefore can be fully determined by data on F_2, without any additional adjustable free parameter.

The results in eqs. (4.7) and (4.10) give together with the total non-diffractive cross section the average number of chains in one event. This average number is, however, not enough to determine the properties of exclusive final states. The sub-collisions may be correlated so that central collisions have a larger, and peripheral a smaller, number of chains. These correlations will be studied in more detail in section 4.4.

4.3.3 Final State Bremsstrahlung

In the LDC model, final state radiation is emitted from the dipoles in the chain in the same way as in the Dipole Cascade Model (DCM) [29, 30] for time-like parton cascades, which is implemented in the ARIADNE program [31]. In these time-like cascades the emissions are, however, limited by the $k_{\perp}$ of the propagators in the initial chain. In figure 4.3, this corresponds to the area below the line connecting the q_i points.

The parameters in the DCM have been fitted, together with the parameters in the string fragmentation [32] in PYTHIA, to reproduce a wide range of final-state observables at LEP to an extraordinary precision. The main parameters in ARIADNE are $\Lambda_{\rm QCD}$ and the cutoff in transverse momentum, $p_{\perp\rm cut}$, which have been fitted by the DELPHI collaboration to 0.22 GeV and 0.6 GeV respectively [33]. The fact that $p_{\perp\rm cut}$ typically is smaller than the cutoff for the ISB, $k_{\perp 0}$,

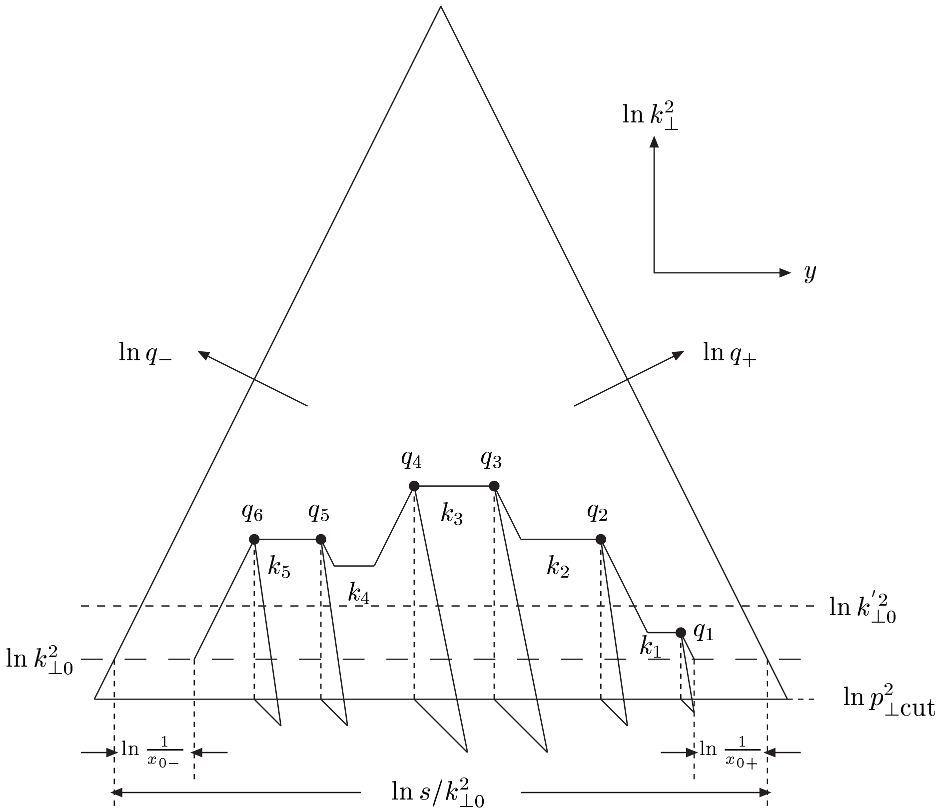

Figure 4.3: An example of a dipole chain in hadronic collisions. The initial-state emissions q_i are marked with points in the $(y, \kappa = ln(q_\perp^2))$-plane. The connecting lines correspond to the propagators k_i.

obtained by fitting LDC to F_2 data, means that FSB will be allowed also below $k_{\perp 0}$ down to the hadronization cutoff, $p_{\perp\mathrm{cut}}$. This means that if $k_{\perp 0}$ is increased to $k'_{\perp 0}$, some gluon emissions in the initial state, such as q_1 in figure 4.3, will no longer be allowed, but will then instead be allowed as FSB. In this way the distribution of the final state partons should be quite insensitive to the precise value of $k_{\perp 0}$.

Special care must be taken when radiating from the dipoles connecting the first ISB gluons with the hadron remnants. This problem is especially important for the soft chains, where FSB will also be allowed below $k_{\perp 0}$ from a dipole between the remnants. This will be discussed further in section 4.5.

4.4 Multiple scatterings in hadronic collisions

At high energies the inclusive cross section for parton-parton sub-collisions becomes larger than the total non-diffractive cross section, which means that there are on average more than one hard collision per event. Indications for multiple hard collisions are observed both in hadronic collisions [10] and in photoproduction [34]. The properties of exclusive final states then depend sensitively on the distribution in the number of sub-collisions in a single event. At high energies two colliding hadrons are Lorentz contracted to two flat pancakes. When they pass through each other the different regions are causally disconnected, and it is then natural to assume that the sub-collisions are independent for a fixed value of the impact parameter, b. This implies an eikonalized description, where the probability to have n sub-collisions is given by a Poissonian distribution with an average, $\bar{n}(b)$, which depends on b, or alternatively by such a distribution with the value $n = 0$ excluded. Models of this type include PYTHIA, HERWIG [1], and the Dual Parton Model.

4.4.1 Impact-Parameter Dependence

We note that the result depends not only upon the average number of hard sub-collisions for fixed impact parameter, $\tilde{n}(b)$, but also on the probability for an interaction, $P_{int}(b)$, for this value of b. These quantities are defined so that the inclusive sub-collision cross section is given by $\sigma_{hard} = \int d^2b\, \tilde{n}(b)$ and the total non-diffractive cross section by the relation $\sigma_{tot} = \int d^2b\, P_{int}(b)$. Expressed in these quantities we have

$$\bar{n}(b) = \tilde{n}(b)/P_{int}(b) \tag{4.11}$$

In ref. [10] it is found that e.g. the "pedestal effect", i.e. the fact that the background is larger around a high $E_\perp$ jet than in a minimum bias event, and the distribution in the number of jets in a single event can be well reproduced if the b-dependence is described by a double Gaussian distribution, corresponding to the presence of a kind of "hard core", while a single Gaussian would severely underestimate the fluctuations. (By a Gaussian distribution we understand here a distribution which is Gaussian in the variable b, and consequently exponential in the density b^2.)

In this paper we will not present a full investigation of such correlations between sub-collisions, but only study some qualitative features. The fact that there often are more than two jets in one single chain in our approach, will imply a positive correlation between the sub-collisions in addition to the one originating from the impact parameter dependence. Therefore the fluctuations in the number of chains due to the impact parameter dependence should be weaker than the fluctuations in the number of sub-collisions in the models

[1] Using the add-on JIMMY program [34]

mentioned above. To illustrate the effect of these two contributions to the correlations, we will study two different cases:

- Completely independent chains, where the number of chains is determined by a Poissonian distribution

$$P_n = e^{-\bar{n}}\frac{\bar{n}^n}{n!} \tag{4.12}$$

  where $\bar{n}$ is the b-independent average number of chains in an event.

- An impact parameter dependence which results in an exponential distribution in $\bar{n}(b)$ when weighted by the probability $P_{int}(b)$. The probability $P(n')$ for a collision with a centrality corresponding to $\bar{n}(b) = n'$ is thus assumed to satisfy

$$P(n') = \frac{1}{\sigma_{tot}}\int d^2bP_{int}(b)\delta(\bar{n}(b) - n') = \bar{n}e^{-n'/\bar{n}} \tag{4.13}$$

  Here $\bar{n}$ is the average n'-value. Assuming a Poissonian distribution in n for fixed value of b, i.e. for fixed value of n', we then find a geometric distribution with the same average, $\bar{n}$, for the number of chains, n, in a random event. For the distribution in the number of chains we then find the geometric distribution in n, with the same average, $\bar{n}$:

$$P_n = \int dn'P(n')\cdot e^{-n'}\frac{n'^n}{n!} = \frac{1}{1+\bar{n}}(\frac{\bar{n}}{1+\bar{n}})^n \tag{4.14}$$

In figure 4.4 we compare the simple geometrical distribution with the distribution in number of scatterings in PYTHIA with a double Gaussian b-distribution, and we find that the geometrical distribution actually is extremely similar. Also shown is PYTHIA with independent scatterings and a Poissonian distribution for comparison.

A reason to concentrate on these two alternatives in this preliminary study, is that the Poissonian distribution will act as a reference for the effect of further correlations, while the geometric distribution can mimic the fluctuations in the favoured PYTHIA version. We also note that both these distributions are chosen so that they depend only on a single parameter, the average number of chains, $\bar{n}$.

4.5 Monte Carlo implementation

The LDC event generator LDCMC, is written to model deeply inelastic lepton–hadron scattering or, more specifically, γ^*-h scattering. To use it for generating

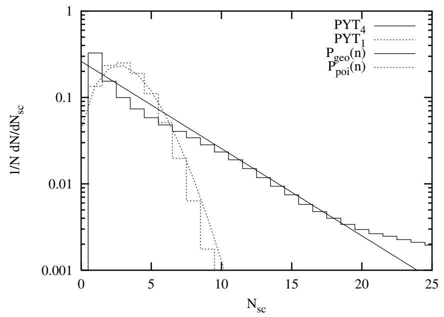

Figure 4.4: The distribution in number of scatterings for non-diffractive events in PYTHIA. The full histogram is $\mathbf{PYT_4}$ and the dotted histogram is $\mathbf{PYT_1}$ (see subsection 4.6.1 for notation). The full and dotted curves are geometrical and Poissonian distributions respectively with the same average as the corresponding histograms.

single dipole chains in hadronic collisions we lower the virtuality of the γ^* to below $k_{\perp 0}$ and use a reweighting procedure to obtain the correct input parton densities for the hadron and to account for the fact that the photon only couples to quarks, while the hadron also has a gluon density.

Since we expect that there will be several chains in each hadronic collision, we need to discuss two problems concerning how to combine the generated chains: we need to consider the colour connections between the chains and the hadron remnants, and we need to ensure energy–momentum conservation, so that the chains do not take more than the available energy in the colliding hadrons.

4.5.1 Colour Connections

We do not expect all individual chains to be connected to the hadron remnant – this would give a large set of overlapping strings producing too many hadrons in the full rapidity region. Instead we expect that ISB partons in the ends of each chain may be connected to corresponding partons in other chains. One could also imagine situations where two chains are different branches on the same cascading tree. This possibility will, however, be neglected in the present analysis. To be less sensitive to the colour connections we will here only consider the properties of the *partonic* final state. However, although less sensitive, also the final state radiation will be affected to some extent, since the emitting dipoles depend on these connections.

Clearly, the question of colour connections is a very complicated one, and we will defer a detailed investigation to a later publication. Here we will simply assume that the FSB can be added to each chain independently, also allowing the dipoles between the ISB partons in the ends of the chain and the hadron remnants to radiate. This will certainly somewhat overestimate the amount of soft partons in the events and the results presented below must therefore be considered somewhat preliminary.

The FSB emissions from the remnant dipoles also pose another problem. The emission probability from a dipole is basically flat in $\ln p_\perp^2$ and rapidity. This means that the emitted gluon can easily take a large fraction of the remnant momentum. The standard way of dealing with this in ARIADNE is the Soft Radiation Model [35], but here we will use a different method, to be as insensitive as possible to the cutoff, $k_{\perp 0}$. Looking at the initial-state emission of the gluon q_1 in figure 4.3, it will also have a basically flat rapidity distribution, except there will be a $(1 - x_{0+})^4$ suppression from the input gluon density (see eq. (4.17) and table 4.1 in section 4.6.1). If we now increase the cutoff to $k'_{\perp 0}$, q_1 should instead be allowed as a final state emission with approximately the same distribution. We have therefore chosen a procedure where for each gluon emission generated according to the Dipole Cascade Model in a remnant dipole, a corresponding new x'_{0+} is calculated from the energy loss of the remnant, and the emission is only accepted with a probability

$$\left(\frac{1 - x'_{0+}}{1 - x_{0+}}\right)^4. \tag{4.15}$$

The correct procedure would, of course, be to use the actual ratio of the relevant input parton densities. We have, however, checked that the results are insensitive to the details of the suppression (e.g. changing the exponent from 4 to 3) and will therefore in this paper be satisfied with this simplified treatment.

4.5.2 Energy–Momentum Conservation

The treatment of emissions from the remnant dipole is also related to the question of energy–momentum conservation when combining several chains. If each chain takes a large fraction of the energy of the incoming hadron, there will not be enough energy to have many chains. To ensure energy–momentum conservation we have adopted the following procedure when combining chains into single events.

1. First we choose n, the number of chains to be included in the event, from either the Poissonian distribution in eq. (4.12) or the geometrical one in eq. (4.14).

2. Then we choose n chains, either hard chains with both ISB and FSB partons or soft ones with only FSB, according to the values of σ_c and σ_{c0}.

3. The selected chains are then ordered in the transverse momentum of the hardest parton. This procedure is analogous to the treatment in the PYTHIA model. It implies that the hardest chain is always accepted in the following veto procedure, which is necessary to ensure that the spectrum of high $E_\perp$ jets is correctly described.

4. Each chain is now tested in order of decreasing hardness. The sum of the positive and negative light-cone momentum already used up by the previously accepted chains is calculated and from that, new effective values of $x'_{0\pm}$ of the current chain are obtained. Chains which would take more than the available energy are vetoed. Kinematically allowed chains are accepted with a probability
$$\left(\frac{1-x'_{0+}}{1-x_{0+}}\times\frac{1-x'_{0-}}{1-x_{0-}}\right)^4, \tag{4.16}$$
to approximate the change in the input parton densities after some partons have already been extracted. As for the treatment of remnant dipoles in eq. (4.15) it may be more correct to here use the ratio of the actual input densities used. (Again we have checked that our results are not very sensitive if the exponent is changed from 4 to 3.)

5. We are now left with $n_{\rm acc} \leq n$ accepted chains which are combined into a partonic event.

The procedure presented here is at present rather cumbersome and slow and some results presented here have rather large statistical fluctuations. The absence of hadronization also makes the current version of the program unsuited for direct comparison with experiment. A new publicly available version of LDCMC capable of generating hadronic collision events will therefore be postponed until the issues of colour connections have been addressed in more detail.

4.6 Results

In this section we will study features of jet and minijet production, which are sensitive to the properties of multiple interactions. We will look at inclusive jet production, minijet distributions, and the pedestal effect and other properties of underlying events.

As example we have chosen *pp* collisions at the Tevatron energy, 1.8 TeV in the cms. To be specific we define jets with a simple cone-algorithm[2] using an idealized calorimeter with cells distributed uniformly in pseudo-rapidity and azimuth angle with the size $\delta\eta \times \delta\phi \approx 0.2 \times 0.2$. The transverse energy of all generated partons are collected in the corresponding cells, and any cell with a

[2] PYCELL in PYTHIA

fit	A_g	a_g	b_g	a_d	b_d	a_u	b_u	a_s	b_s	$k_{\perp 0}$	χ^2/d.o.f.
fit-0	2.24	0.09	**4**	1.77	**3**	0.58	**3**	**0**	**4**	**0.88**	795/625
fit-1	1.86	0.00	**4**	1.78	**3**	0.57	**3**	**0**	**4**	0.99	694/625
fit-2	1.42	-0.09	**4**	1.94	**3**	0.56	**3**	**0**	**4**	**1.14**	710/625
fit-3	1.17	-0.14	**4**	2.10	**3**	0.55	**3**	**0**	**4**	**1.3**	751/625

Table 4.1: The result of the fit of the parameters for the input parton densities to data from H1 [36], ZEUS [37], NMC [38] and E665 [39] in the region $x < 0.3$, $Q^2 > 1.5$ GeV^2. The last columns gives the χ^2 over the number of fitted data points, respectively. Parameters in bold face have not been fitted.

summed $E_\perp$ above 1 GeV is tried as a jet-initiator. If the summed $E_\perp$ within a radius of 0.7 in the η-ϕ plane around such an initiator is above 3 GeV, this $E_\perp$ is assigned to a jet in the $E_\perp$ weighted direction of the cells included. Only jets with $|\eta| < 2.5$ are included in the following.

As discussed above we will in this preliminary study not include hadronization effects, which are sensitive to how the chains are colour connected. We will therefore only compare with parton distributions generated by the PYTHIA generator, and make no direct comparisons with experimental data.

4.6.1 Fitting procedure

The parameters used in the MC simulations are fitted to DIS data. To get quantitative results from LDC we must convolute the dipole chains with input parton densities in the proton. These densities are not à priori known, but must be parameterized in some way and fitted to data. The form of these densities are taken to be

$$xf_i(x, k_{\perp 0}^2) = A_i x^{a_i}(1-x)^{b_i}, \tag{4.17}$$

where $i = d_v, u_v, g$ and s for the d-valence, u-valence, gluon and sea-quark densities respectively (where the sea flavour densities are assumed to be $f_{\bar{d}} = f_{\bar{u}} = 2f_{\bar{s}}$). The parameters A_i, a_i, b_i and the perturbative cutoff, $k_{\perp 0}$, are then fitted to reproduce the measured data on F_2. There are some relations between the parameters which are fixed by sum rules. Thus A_{d_v} and A_{u_v} are determined by flavour conservation and A_s is fixed by momentum conservation. The fits to F_2 do not constrain the remaining parameters very strongly, so we have fixed the b parameters to 3 in the valence densities and to 4 in the sea and gluon densities. The best fit is the one called *standard* in reference [28] and fit-1 in table 4.1. The fitted value of $k_{\perp 0}$ is 0.99 GeV, but since we would like to check the dependence on the cutoff, we also present additional fits in table 4.1 where $k_{\perp 0}$ has been fixed to higher and lower values.

In the following we will look at a couple of options for LDC and compare with different cases in PYTHIA. (For the alternatives with a single chain (**LDC$_0$**

and $\mathbf{LDC'_0}$) or a single sub-collision ($\mathbf{PYT_0}$) we can only study inclusive cross sections, and the reduction from energy conservation due to overlayed chains or collisions is not included.)

$\mathbf{LDC_0}$: Single LDC chains with the default (fit-1) tuning.

$\mathbf{LDC_{\mathit{P}}}$: Uncorrelated multiple LDC chains (fit-1) according to the Poissonian distribution.

$\mathbf{LDC_{\mathit{G}}}$: Multiple LDC chains (fit-1) according to the geometrical distribution.

$\mathbf{LDC'_0}$: As $\mathbf{LDC_0}$ but with the $k_{\perp 0} = 1.3$ GeV tuning (fit-3) (similarly for $\mathbf{LDC'_{\mathit{G}}}$).

$\mathbf{PYT_0}$: PYTHIA without multiple scatterings selecting low-$p_\perp$ events without hadronization. Everything else default.

$\mathbf{PYT_1}$: As $\mathbf{PYT_0}$ but with uncorrelated multiple scatterings (with default values[3]).

$\mathbf{PYT_4}$: As $\mathbf{PYT_0}$ but with multiple scatterings according to a double Gaussian distribution (with default values).

$\mathbf{PYT'_4}$: As $\mathbf{PYT_4}$ but with a higher soft regularization parameter (2.5 GeV instead of 2.1 GeV).

Since $\mathbf{PYT_4}$ is known to give a fair description of experimental data, we will in the following use it as a reasonable approximation to nature. We should keep in mind, however, that the results presented here are on parton level only, and that many of the observables studied have not been measured experimentally, so deviations from $\mathbf{PYT_4}$ do not imply that our model is wrong. We will also mostly compare $\mathbf{LDC_{\mathit{P}}}$ with $\mathbf{PYT_1}$, which both are based on the assumption of uncorrelated scatterings; and $\mathbf{LDC_{\mathit{G}}}$ with $\mathbf{PYT_4}$, since we have shown in figure 4.4 that $\mathbf{PYT_4}$ is well approximated by a geometrical distribution. Note, however, that the procedure for energy conservation in LDC severely limits the possibility to have many chains, and $\mathbf{LDC_{\mathit{G}}}$ deviates substantially from a geometrical distribution, as can be seen in figure 4.5. The effects of energy conservation in PYTHIA is much smaller since the ISB is modeled with a DGLAP parton shower with strongly ordered virtualities which means that only very rarely are partons emitted close to the hadron remnants.

4.6.2 Chain multiplicity

First we want to study the cross section for the formation of a chain in a hadronic collision, which is given by eqs. (4.7) and (4.10). For fit-1 at a c.m. energy of 1.8 TeV, we obtain for perturbative chains a cross section of $\sigma_{\mathrm{c}} =$

[3]The indices for the PYTHIA options refer to the setting of the switch, `MSTP(82)`, selecting the multiple interaction model.

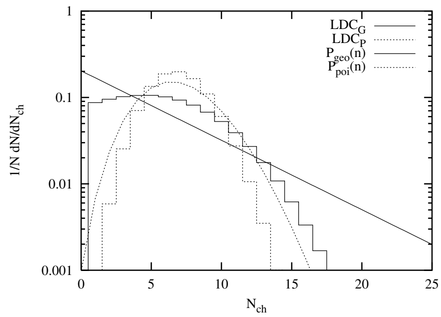

Figure 4.5: The distribution in number of chains per event in LDC. The full histogram is $\mathbf{LDC}_{\boldsymbol{G}}$ and the dotted histogram is $\mathbf{LDC}_{\boldsymbol{P}}$. The full and dotted curves are geometrical and Poissonian distributions respectively with the same average as the corresponding histograms.

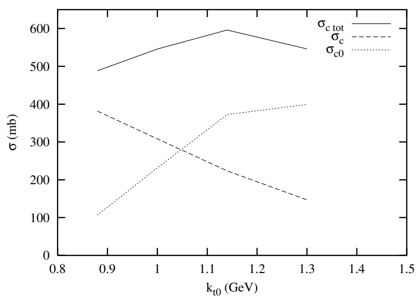

Figure 4.6: The cross section per chain in the LDC model as a function of the cutoff, $k_{\perp 0}^2$. The dashed line is the cross section for chains with at least on emission above the cutoff, the dotted line is for soft chains without emissions above the cutoff, and the full line is the sum of the two. Note that the input parton densities have been re-fitted for each value of $k_{\perp 0}$.

315 mb, which is much larger than the non-diffractive cross section at the Tevatron[4], $\sigma_{\rm nd} \approx 39$ mb. In figure 4.6 we see how this cross section per chain varies with the soft cutoff used in the fit to DIS F_2 data. The result is an almost linear dependence on the cutoff $k_{\perp 0}$. (Note that the input parton densities have been re-fitted for each value of $k_{\perp 0}$.) In figure 4.6 we also show the cross section for formation of soft chains, represented by the exchange of a single

[4] We take the value as estimated by a simple parameterization in PYTHIA based on ref. [40].

(non-perturbative) gluon with virtuality $k_{\perp 0}^2$ (cf. eq. (4.10)). We see that if the cutoff is increased, the cross section for the perturbative chains will decrease, but the cross section for the non-perturbative chains will increase since the fitted input gluon density is then more divergent for small x. From figure 4.6 we see that the sum of the two cross sections is almost independent of the cutoff $k_{\perp 0}$. Thus we conclude that the total number of chains in pp collisions can be fully determined by data on F_2, without any additional adjustable free parameter.

Taking the sum of σ_c and σ_{c0} (547 mb for $k_{\perp 0} = 0.99$ GeV) we would then expect on the average around 14 chains per collision. However, after the veto procedure to conserve energy and momentum we are left with an average of 7 and 6 chains per event for $\mathbf{LDC}_{\boldsymbol{P}}$ and $\mathbf{LDC}_{\boldsymbol{G}}$ respectively.

4.6.3 Inclusive jet production

In figure 4.7a we look at the inclusive differential cross section for the highest $E_\perp$ jet in a single LDC chain and compare it to the corresponding cross section in PYTHIA without multiple interactions ($\mathbf{PYT_0}$). We find that the LDCMC result is close to PYTHIA. Comparing $\mathbf{LDC_0}$ and $\mathbf{LDC'_0}$ we find a weak dependence on the cutoff. The reason for this may be that the input densities in LDC has been fitted to F_2 data which are only indirectly sensitive to the gluon contribution. Indeed, in $\mathbf{LDC'_0}$ the gluons carry a smaller fraction of the proton momentum which could account for the differences in figure 4.7a. In the future, when LDCMC can be compared directly with high-$E_\perp$ jet production, it should be possible to make a more global fit of the input parton densities, which would better constrain the gluon distribution. Another reason for the dependence could be the differences in FSB caused by our simplified treatment of the colour connections of the chains.

In figure 4.7b we show the differential $E_{\perp\max}$ cross with multiple interactions added with Poissonian ($\mathbf{LDC}_{\boldsymbol{P}}$) and geometrical ($\mathbf{LDC}_{\boldsymbol{G}}$) distributions for the number of chains in one event. For comparison we also show $\mathbf{PYT_1}$ and $\mathbf{PYT_4}$. We find that the LDC curves more or less lie in between the PYTHIA ones, which indicates that the procedure chosen to combine chains is a reasonable one. We note, however, a difference for small $E_{\perp\max}$ values where $\mathbf{LDC}_{\boldsymbol{G}}$ lies significantly above $\mathbf{PYT_4}$.

4.6.4 Minijet distributions

As another check that our procedure is reasonable, we look at the rapidity distribution of minijets. In figure 4.8a we show the results for $\mathbf{LDC_0}$, $\mathbf{LDC'_0}$ and $\mathbf{PYT_0}$. We find that the curves agree well, and the cutoff dependence in LDC is negligible. The slight asymmetry in the LDC distributions is due to the fact that the recoil strategy for the final state emissions from the parton

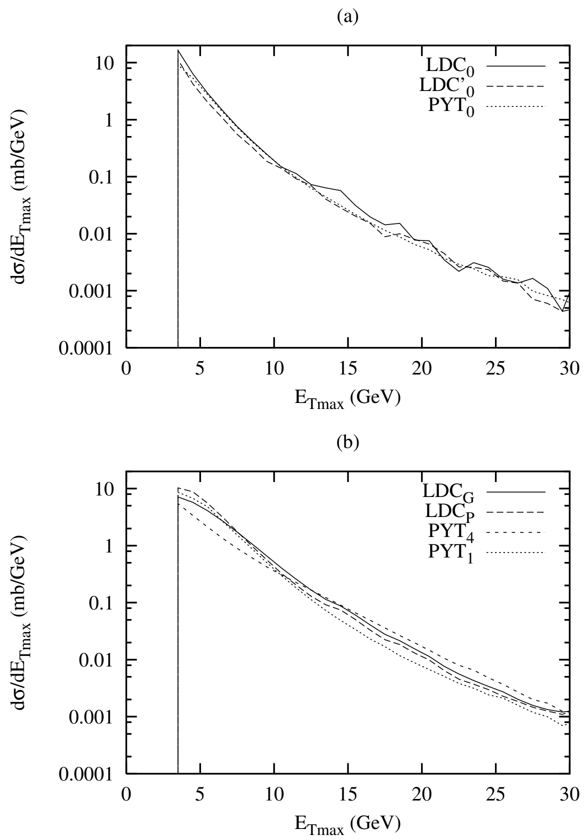

Figure 4.7: The differential $E_{\perp\max}$ cross section. In (a) $E_{\perp\max}$ is the largest $E_\perp$ jet in a chain or hard scattering. Full line is $\mathbf{LDC_0}$, dashed is $\mathbf{LDC_0'}$ and the dotted line is $\mathbf{PYT_0}$. In (b) $E_{\perp\max}$ is the largest $E_\perp$ in an event. Full line is $\mathbf{LDC}_{\boldsymbol{G}}$, long-dashed is $\mathbf{LDC}_{\boldsymbol{P}}$, short-dashed is $\mathbf{PYT_4}$ and the dotted line is $\mathbf{PYT_1}$.

closest to the photon in the LDCMC for DIS is not fully consistently modified in this preliminary application to hadronic collisions.

In figure 4.8b we show the results for the multiple interaction models. Here the LDC curves are above the corresponding PYTHIA ones. Although there are no obvious reasons for the curves to agree, we note that the soft FSB in LDC may be somewhat overestimated, especially for the soft chains. We also note that the statistics for the LDC curves is poor due to the present inefficient

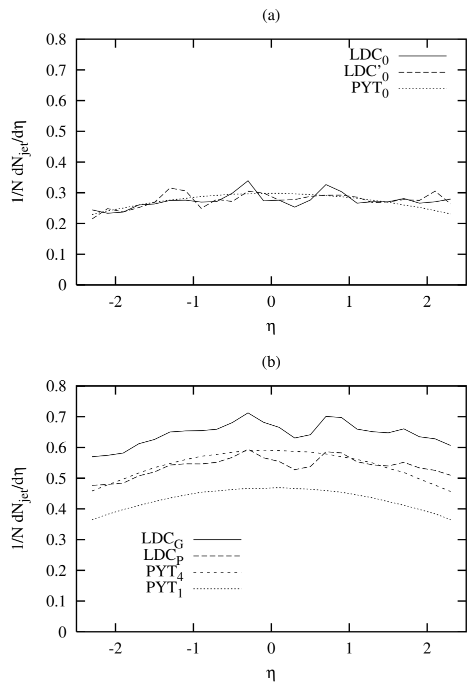

Figure 4.8: The rapidity distribution of minijets (per event with at least one minijet) In (a) the full line is $\mathbf{LDC_0}$, dashed is $\mathbf{LDC'_0}$ and the dotted line is $\mathbf{PYT_0}$. In (b) the full line is $\mathbf{LDC}_{\boldsymbol{G}}$, long-dashed is $\mathbf{LDC}_{\boldsymbol{P}}$, short-dashed is $\mathbf{PYT_4}$, dash-dotted is $\mathbf{PYT_3}$ and the dotted line is $\mathbf{PYT_4}$. (The different LDC curves have been obtained using the same sample of chains which is why the statistical fluctuations are correlated.)

simulation procedure. In addition, the statistical fluctuations in $\mathbf{LDC}_{\boldsymbol{P}}$ and $\mathbf{LDC}_{\boldsymbol{G}}$ are correlated since the two curves are obtained using the same set of generated single LDC chains.

To investigate the fluctuations we show in figure 4.9a the distribution in number of jets in the central 5 units of rapidity for the different multiple interaction models. It is clear that $\mathbf{LDC}_{\boldsymbol{G}}$ has much larger fluctuations than has $\mathbf{LDC}_{\boldsymbol{P}}$, as was expected. $\mathbf{LDC}_{\boldsymbol{P}}$ has also larger fluctuations than $\mathbf{PYT_1}$ although both are based on uncorrelated scatterings. This is because in LDC there is, as mentioned above, a possibility to have several hard scatterings in each chain, which increases the correlations. $\mathbf{LDC}_{\boldsymbol{G}}$ does not have as large fluctuations as $\mathbf{PYT_4}$, which also was expected since, as shown in figure 4.5, the

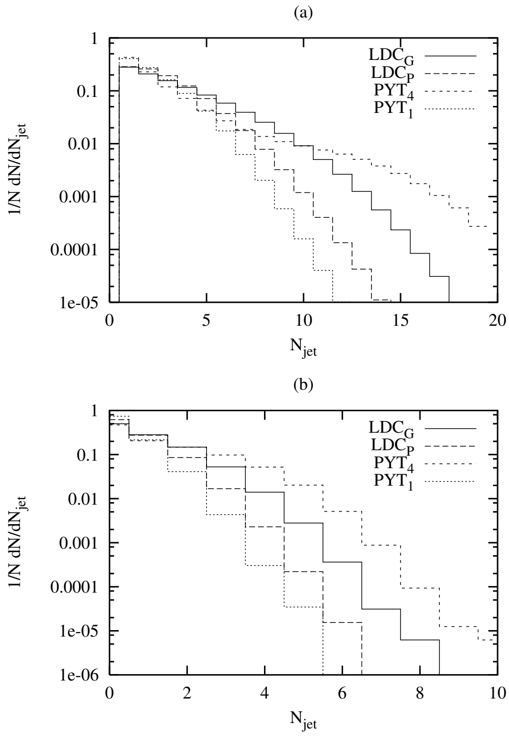

Figure 4.9: The distribution in number of minijets in the range $|\eta| < 2.5$ (per event with at least one minijet). (a) shows all minijets, while (b) is all minijets in the minimum azimuth region (as defined in the text) in each event with $E_{\perp\max} > 10$ GeV. In both cases the full line is $\mathbf{LDC_{\boldsymbol{G}}}$, long-dashed is $\mathbf{LDC_{\boldsymbol{P}}}$, short-dashed is $\mathbf{PYT_4}$, and the dotted line is $\mathbf{PYT_1}$.

distribution in number of chains in $\mathbf{LDC_{\boldsymbol{G}}}$ is much narrower than a geometrical distribution, due to energy conservation.

4.6.5 The Pedestal Effect and Underlying events

The contribution from hard sub-collisions is in many analyses added on top of an independent "underlying event". In reference [41] a number of observables were presented which were shown to be especially sensitive to this background activity. The regions of azimuth which are transverse to the highest $E_\perp$ jet in an event given by $60° < \phi < 120°$, should be less affected by the primary *trigger* scatterings, which mainly populate the collinear and opposite azimuth region from the highest $E_\perp$ jet with hadrons. There are, however, also effects from bremsstrahlung from the primary interaction in the transverse regions, but the authors argue that these typically only affect one of these two regions. Thus, by looking at the activity in the transverse region which has the smallest activity, one is especially sensitive to effects of the "underlying event" and secondary scatterings. We will call this region the *minimum azimuth region*, and in 4.9b we show the distribution in number of jets in this region in events with a trigger jet of $E_{\perp\max} > 10$ GeV. Clearly, the general trend found for the overall distribution in number of jets is present also here.

One of the most important features of the underlying event is the so-called jet pedestal effect, i.e. the fact that the underlying event activity is not independent of a large $E_\perp$ jet. In figure 4.10 we show the average number of minijets as a function of the $E_\perp$ of the hardest jet, both for the overall minijet activity and for the minimum azimuth region. As expected all models show an increasing average number with increasing $E_{\perp\max}$ since, even in the case of uncorrelated scatterings, there is a higher probability to find a large $E_\perp$ jet in an event with many scatterings than in an event with few. Also, the models with most fluctuations gives the strongest rise, while models with fewer fluctuations saturate earlier. We note, however, that for this variable there is a particularly large difference between the $\mathbf{LDC_{\boldsymbol{G}}}$ and $\mathbf{PYT_4}$ models.

4.6.6 Cutoff Dependence

Finally we would like to check the cutoff dependence also for our multiple scattering model. In figure 4.11 we show the distribution in number of jets and the average number of jets as a function of $E_{\perp\max}$ for $\mathbf{LDC_{\boldsymbol{G}}}$ and $\mathbf{LDC'_{\boldsymbol{G}}}$ and we find that the differences indeed are very small. As comparison we also show the results for $\mathbf{PYT_4}$ and $\mathbf{PYT'_4}$. For the double-Gaussian model in PYTHIA, there is no direct cutoff, but rather a soft regularization parameter, $p_{\perp 0}$, which forces the partonic cross sections and the running of α_{s} to be finite at small scales by modifying them according to

$$\frac{d\sigma_{\mathrm{part}}(p_\perp^2)}{dp_\perp^2} \to \frac{d\sigma_{\mathrm{part}}(p_\perp^2)}{dp_\perp^2} \times \left(\frac{p_\perp^2}{p_\perp^2 + p_{\perp 0}^2}\right)^2, \quad \alpha_{\mathrm{s}}(p_\perp^2) \to \alpha_{\mathrm{s}}(p_\perp^2 + p_{\perp 0}^2) \quad (4.18)$$

We see in figure 4.11 that the result is very sensitive to the value of $p_{\perp 0}$, which has to be adjusted to fit experimental data. We also note that in PYTHIA the value of $p_{\perp 0}$ is expected to increase with energy in a way which is not determined by the model, which means that it is difficult to make reliable predictions for future experiments at higher energies. Naturally we should not compare the variation in cutoff for LDC (0.99 $\to$ 1.3 GeV) with the variation in the regularization parameter in PYTHIA (2.1 $\to$ 2.5 GeV). From figure 4.11 we can, however, see that the dependence in LDC is very weak, which means that in this model the result can be directly estimated from data from DIS.

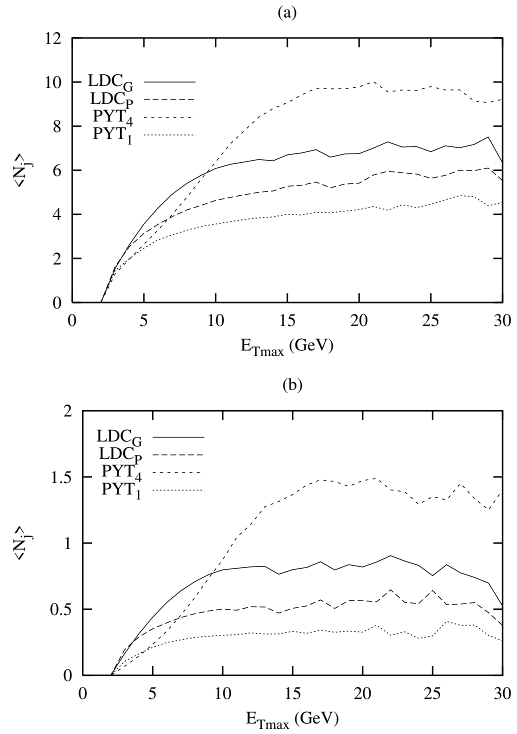

Figure 4.10: (a) The average number of minijets per event as a function of the $E_\perp$ of the largest jet in the event. The full line is $\mathbf{LDC}_{\boldsymbol{G}}$, long-dashed is $\mathbf{LDC}_{\boldsymbol{P}}$, short-dashed is $\mathbf{PYT_4}$ and the dotted line is $\mathbf{PYT_1}$. (b) Is the same but looking only at minijets in the minimum azimuth region.

4.7 Conclusions

In this article we present a new approach to describe high energy hadronic collisions, which is based on the Linked Dipole Chain model for DIS. The main advantage over earlier treatments is a much reduced sensitivity to an infrared cutoff, which in models based on collinear factorization has to be fitted to experimental data. In our model the parton-parton sub-collision cross section can be fully determined by data from DIS, which implies a more intimate relation between hadron-hadron collisions and DIS. We hope that this relation also implies increased possibilities to use data on hh collisions to constrain fits to parton distribution functions. Thus e.g. the connections between different parton chains in hh collisions may be related to gluon saturation effects in

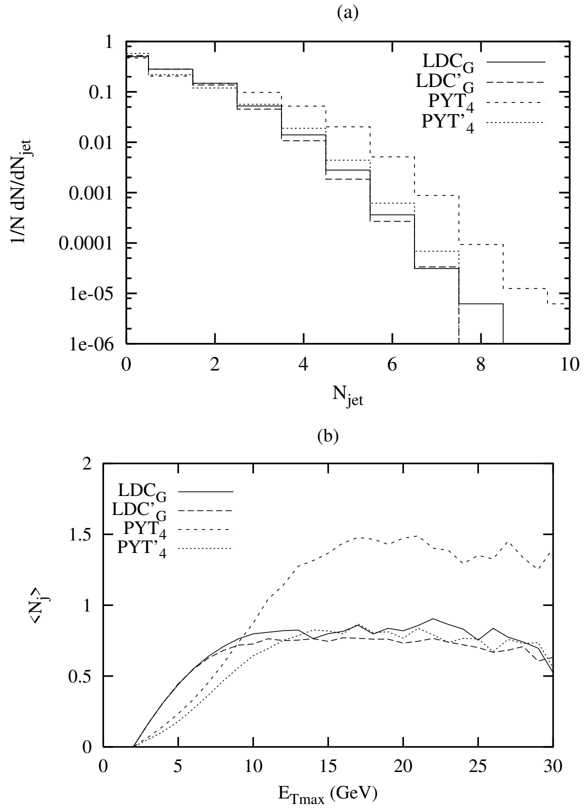

Figure 4.11: (a) The distribution in number of minijets in the minimum azimuth region in events with $E_{\perp\max} > 10$ GeV. (b) The average number of minijets per event in the minimum azimuth region as a function of the $E_{\perp\max}$. In both plots the full line is $\mathbf{LDC}_{\boldsymbol{G}}$, long-dashed is $\mathbf{LDC}'_{\boldsymbol{G}}$, short-dashed is $\mathbf{PYT}_{\mathbf{4}}$ and the dotted line is $\mathbf{PYT}'_{\mathbf{4}}$.

DIS. The insensitivity to a soft cutoff also makes it easier to make reliable extrapolations to higher energies.

At high energies the properties of hadron-hadron collisions appear to be dominated by hard and semi-hard parton collisions. Although the parton-parton collisions are of perturbative nature, various non-perturbative effects make a description of hadronic collisions much more complicated than e.g. DIS:

(i) In a traditional collinear factorization scheme the inclusive sub-collision cross section is divergent for small $p_\perp$, which has to be treated by a soft cutoff $p_{\perp 0}$.

(ii) The inclusive sub-collision cross section is larger than the total non-diffractive cross section, which means that there may be many hard sub-collisions in a single event. This implies that the correlations between the sub-collisions are important.

(iii) The scattered partons can be colour connected with each other and with the proton remnants in different ways by strings or cluster chains.

In models based on collinear factorization the soft cutoff, $p_{\perp 0}$, has to be fitted to experimental data. The correlation between partonic sub-collisions is, in e.g. the DPM model, PYTHIA, and HERWIG, described in an eikonalized form by an impact parameter dependence. For a single hard sub-collision the colour structure can be read off from the perturbative matrix elements [42, 43], but for events with many sub-collisions the result necessarily depends on non-perturbative effects.

The LDC model for DIS is a reformulation and generalization of the CCFM model. It is based on $k_\perp$-factorization and the inclusion of non-$k_\perp$-ordered parton chains, which are expected to be important for limited $p_\perp$ and high energies. The formulation is fully symmetric with respect to the photon and the proton ends of the parton chain, which makes the model also suitable for a description of hadronic collisions. The input soft gluon distribution, $g_0(x, Q_0^2)$, is fitted to data from DIS, and when we then calculate the number of parton chains in pp collisions, we find that the result is actually fixed by the fit to F_2. If the soft cutoff used in the fit is increased the number of hard chains is reduced, but this is fully compensated by an increase of soft chains described by the input distribution function, g_0. (These soft chains are now also allowed to emit final state radiation up to the increased value for the $k_\perp$-cutoff.)

Concerning point (ii) in the list above, we note that some correlations between hard sub-collisions are included automatically, as a single non-$k_\perp$-ordered parton chain can contain two or more local maxima which all correspond to separate hard sub-collisions. Besides this correlation due to sub-collisions in a single chain, we expect that the number of chains is larger in central and smaller in peripheral collisions. As in the models mentioned above, we want to describe this by an impact parameter dependence, and in this paper we have studied two different distributions, one purely stochastic and one similar to the double Gaussian distribution used in the PYTHIA model.

The third problem, concerning colour connections, is very important for the final distribution of hadrons, but less important for a determination of the partonic state before its hadronization. In this preliminary study of the model we focus on features of jet and minijet production, such as the inclusive jet production, minijet distributions and the jet pedestal effect, which are less sensitive to hadronization effects. We will postpone a more detailed analysis of the colour connection structures to future work. In this study we therefore do not include any hadronization effects, and as a consequence we are not comparing our results with experimental data, but are satisfied by a comparison with parton level results from the PYTHIA generator.

For the numerical estimates we are using a modified version of the LDCMC event generator program, and as an example we study pp collisions at $\sqrt{s} = 1.8$ TeV. From the numerical results we realize that it is very essential to consider the effects of energy-momentum conservation. This reduces the possibility to have many chains in a single event, and it also constrains the final state radiation in the regions close to the proton remnants.

On a qualitative level the results from our two versions agree well with the ones obtained from PYTHIA. We find that our version with uncorrelated chains gives larger fluctuations than the corresponding model with uncorrelated scatterings in PYTHIA, which is expected since the dipole chains already include some correlations between multiple scatterings in the same chain. Including the correlations from our geometrical chain distribution increases the fluctuations, but not fully to the level of the model based on a double Gaussian impact parameter dependence in PYTHIA. This is because the suppression of large chain-multiplicities due to the energy conservation procedure, is larger than the corresponding suppression in PYTHIA.

As discussed above, there are still unsolved problems in the LDC model for hadronic collisions. This concerns in particular the modeling of colour connections between the chains and the hadron remnants in a single event, which needs to be analysed in much more detail. In turn, this will affect the way final state bremsstrahlung and hadronization are handled, and also the impact of energy conservation. In particular, the simplified model presented here probably overestimates the soft final state emissions, since the final state radiation is allowed from each chain independently. With proper treatment of colour connections we expect a reduction of such soft emissions.

Furthermore, the implementation of the model in the LDCMC event generator needs to be improved substantially, as the current procedure, where γ^*-p collision events need to be reweighted and combined by hand into p-p events, is clearly too cumbersome.

Despite the shortcomings of the simplified model presented here, we are confident that the problems can be solved and that the final model will be able to describe essential features of high energy hadronic collisions, including underlying events and jet-pedestal effects in high $E_\perp$ events.

Acknowledgments

We would like to thank Torbjörn Sjöstrand for valuable discussions.

References

[1] P. Huovinen, P. V. Ruuskanen, and J. Sollfrank *Nucl. Phys.* **A650** (1999) 227–244, `nucl-th/9807076`.

[2] B. Andersson, G. Gustafson, and B. Nilsson-Almqvist *Nucl. Phys.* **B281** (1987) 289.

[3] B. Andersson, G. Gustafson, and H. Pi *Z. Phys.* **C57** (1993) 485–494.

[4] A. Capella and J. Tran Thanh Van *Z. Phys.* **C10** (1981) 249–262.

[5] A. Capella, U. Sukhatme, C.-I. Tan, and J. Tran Thanh Van *Phys. Rept.* **236** (1994) 225–329.

[6] P. Aurenche *et al. Phys. Rev.* **D45** (1992) 92–105.

[7] F. E. Paige, S. D. Protopopescu, H. Baer, and X. Tata `hep-ph/9804321`.

[8] G. Corcella *et al. JHEP* **01** (2001) 010, `hep-ph/0011363`.

[9] T. Sjöstrand, et al. *Comput. Phys. Commun.* **135** (2001) 238–259, `arXiv:hep-ph/0010017`.

[10] T. Sjöstrand and M. van Zijl *Phys. Rev.* **D36** (1987) 2019.

[11] V. N. Gribov and L. N. Lipatov *Yad. Fiz.* **15** (1972) 781–807.

[12] L. N. Lipatov *Sov. J. Nucl. Phys.* **20** (1975) 94–102.

[13] G. Altarelli and G. Parisi *Nucl. Phys.* **B126** (1977) 298.

[14] Y. L. Dokshitzer *Sov. Phys. JETP* **46** (1977) 641–653.

[15] E. A. Kuraev, L. N. Lipatov, and V. S. Fadin *Sov. Phys. JETP* **45** (1977) 199–204.

[16] I. I. Balitsky and L. N. Lipatov *Sov. J. Nucl. Phys.* **28** (1978) 822–829.

[17] G. Gustafson and G. Miu *Phys. Rev.* **D63** (2001) 034004, `hep-ph/0002278`.

[18] B. Andersson, G. Gustafson, and J. Samuelsson *Nucl. Phys.* **B467** (1996) 443–478.

[19] B. Andersson, G. Gustafson, and H. Kharraziha *Phys. Rev.* **D57** (1998) 5543–5554, `hep-ph/9711403`.

[20] H. Kharraziha and L. Lönnblad *JHEP* **03** (1998) 006, `hep-ph/9709424`.

[21] V. S. Fadin and L. N. Lipatov *Phys. Lett.* **B429** (1998) 127–134, `hep-ph/9802290`.

[22] M. Ciafaloni *Nucl. Phys.* **B296** (1988) 49.

[23] S. Catani, F. Fiorani, and G. Marchesini *Phys. Lett.* **B234** (1990) 339.

[24] H. Jung *Comput. Phys. Commun.* **143** (2002) 100–111, `hep-ph/0109102`.

[25] **Small x** Collaboration, B. Andersson *et al.* `hep-ph/0204115`.

[26] **CTEQ** Collaboration, H. L. Lai *et al.* *Eur. Phys. J.* **C12** (2000) 375–392, `hep-ph/9903282`.

[27] A. D. Martin, R. G. Roberts, W. J. Stirling, and R. S. Thorne *Eur. Phys. J.* **C23** (2002) 73–87, `hep-ph/0110215`.

[28] G. Gustafson, L. Lönnblad, and G. Miu *JHEP* **09** (2002) 005, `hep-ph/0206195`.

[29] G. Gustafson *Phys. Lett.* **B175** (1986) 453.

[30] G. Gustafson and U. Pettersson *Nucl. Phys.* **B306** (1988) 746.

[31] L. Lönnblad *Comput. Phys. Commun.* **71** (1992) 15–31.

[32] B. Andersson, G. Gustafson, G. Ingelman, and T. Sjöstrand *Phys. Rept.* **97** (1983) 31.

[33] K. Hamacher and M. Weierstall, "The Next Round of Hadronic Generator Tuning Heavily Based on Identified Particle Data," `hep-ex/9511011`.

[34] J. M. Butterworth, J. R. Forshaw, and M. H. Seymour *Z. Phys.* **C72** (1996) 637–646, `hep-ph/9601371`.

[35] B. Andersson and G. Gustafson and L. Lönnblad and U. Pettersson *Z. Phys.* **C43** (1989) 625.

[36] **H1** Collaboration, S. Aid *et al.* *Nucl. Phys.* **B470** (1996) 3–40, `hep-ex/9603004`.

[37] **ZEUS** Collaboration, M. Derrick *et al.* *Z. Phys.* **C72** (1996) 399–424, `hep-ex/9607002`.

[38] **New Muon** Collaboration, M. Arneodo *et al.* *Phys. Lett.* **B364** (1995) 107–115, `hep-ph/9509406`.

[39] **E665** Collaboration, M. R. Adams *et al.* *Phys. Rev.* **D54** (1996) 3006–3056.

[40] A. Donnachie and P. V. Landshoff *Phys. Lett.* **B296** (1992) 227–232, `hep-ph/9209205`.

[41] **CDF** Collaboration, T. Affolder *et al.* *Phys. Rev.* **D65** (2002) 092002.

[42] G. Gustafson *Z. Phys.* **C15** (1982) 155–160.

[43] H. U. Bengtsson *Comput. Phys. Commun.* **31** (1984) 323.